

**COVERAGE CONTROL:
FROM HETEROGENEOUS ROBOT TEAMS TO EXPRESSIVE SWARMS**

A Dissertation
Presented to
The Academic Faculty

By

María T. Santos Fernández

In Partial Fulfillment
of the Requirements for the Degree
Doctor of Philosophy in the
School of Electrical and Computer Engineering

Georgia Institute of Technology

August 2020

Copyright © María T. Santos Fernández 2020

**COVERAGE CONTROL:
FROM HETEROGENEOUS ROBOT TEAMS TO EXPRESSIVE SWARMS**

Approved by:

Dr. Magnus Egerstedt, Advisor
School of Electrical and Computer
Engineering
Georgia Institute of Technology

Dr. Seth Hutchinson
School of Interactive Computing
Georgia Institute of Technology

Dr. Ayanna Howard
School of Electrical and Computer
Engineering
Georgia Institute of Technology

Dr. Samuel Coogan
School of Electrical and Computer
Engineering
Georgia Institute of Technology

Dr. Vijay Kumar
Department of Mechanical Engineering
and Applied Mechanics
University of Pennsylvania

Date Approved: July 21, 2020

Only through motion can the soul be seen

Anne Carson

A meu pai e miña nai

ACKNOWLEDGEMENTS

It is a truth universally acknowledged, that a grad student in pursuit of a Ph.D., must be in want of a vital transformation. My journey at Georgia Tech has been the most challenging, enriching, and fulfilling experience of my life. But, above all, it has been a lot of fun. I am forever grateful to everyone that has helped me along the way and I will try my best to make them justice here.

With all certainty, there is not a person that has positively influenced more my adult self than my doctoral advisor, Professor Magnus Egerstedt. To this day, I still reflect upon the serendipity that brought me to his class on my very first day at Georgia Tech and the somewhat naiveté that helped me ask about joining his lab. There are no words to express my gratitude to Magnus for his continued mentorship on my research, teaching, and general life choices; but mostly for his encouragement to pursue my slightly less-than-conventional interests during my Ph.D. and for helping me design an effective but singular research agenda including them. With his help, I have become quite confident at asking the big research *whys*: why do we do something, but also why we do it a certain way. There is something about Magnus, however, that I have yet to master, and that is his ability to always elevate people's morale and motivation. He has this kind of superpower that makes you feel so much better about your research—and life, really—every time you have a meeting with him, and I strive to someday transmit that kind of positive energy to my mentees. I will miss our weekly conversations dearly.

I oftentimes find myself explaining to people why grad school is so amazing and justifying my lack of desire to graduate for so long. I have learned now that this can be hard to grasp when you have not been surrounded by the extraordinary bunch that comprises the GRITS Lab. I feel extremely privileged to have been surrounded by the most creative, enthusiastic, and supportive people, who have spoiled me with rewarding, interesting, and fun conversations on a daily basis. Hands down, the biggest shout-out goes to my partners in

crime, Siddharth Mayya and Gennaro Notomista—I am forever indebted for the happiness you brought into my life every day during the last four years. I could not have wished for better teammates, research critics, and conference explorers, but, most of all, friends; and I hope our paths will cross periodically in the future (even if it takes some extra control effort on our part). I would also like to express my deepest appreciation to my labmates Yousef Emam, Anqi Li, Chris Banks, Ian Buckley, Mark Mote, and Pietro Pierpaoli; to the former GRITSers Matt Hale, Daniel Pickem, Tina Setter, Yancy Diaz-Mercado, Sebastian Ruf, Li Wang, Paul Glotfelter, Karthik Rao, Jeremy Cai and, Sean Wilson; and visitors Riku Funada and Alessia Benevento, for their continuous streamline of useful feedback and smart advice, but mostly for making TSRB such a welcoming space and always keeping their smiling faces even through the loudness of my conversations. You guys are champs, I am spoiled for life.

Throughout my doctoral journey I have attended some outstanding conferences where I have been very lucky to meet my favorite fellow roboticists. Thanks to them, I have learnt that (i) there is life beyond swarms—albeit maybe not as fascinating—and (ii) conferences are definitely not only about talks, but friends. Special thanks to Mario Selvaggio, David Saldaña, Kalesha Bullard, Dario Bellicoso, and Lorenzo Sabattini for not only making conferences a blast but also for helping extensively these last two years with my research projects, career decisions and overall mental health. I will try to meet all possible conference deadlines from now on, I promise.

The city of Atlanta will forever be a fundamental part of my identity, and I owe that to all the wonderful people that have contributed to my personal story during my stay here. As a European used to being able to reach everywhere by foot, I would have been convinced Atlanta was a hostile city for much longer if it was not for Ikay, who, thanks to his fourth year Ph.D. wisdom, rightfully persuaded me to socialize in my first semester and onwards. I am also very grateful to Nick, with whom I have shared amazing times in Atlanta’s coolest neighborhoods and throughout the US. To my latino gang, I have never

had as much fun in my life as at our parties, thank you for accepting me as one of your own. Among my Colombian sweethearts, I need to single out Andrés, who took me under his wing and made me discover my two favorite social roles—i.e. hostess and DJ; and Daniela, for our philosophical conversations about life utility functions that would go until the crack of dawn. The Atlantic Ocean has certainly kept me from visiting my family as much as I would like, but I must say that my roommates never left me feeling alone here. I am grateful to Eryn for her congregation skills around Friends, to Nathan for always being down to discuss the randomest topics in our after-dinner tea time, and to Chris and Lesia for supporting all my stress during this final sprint. Very special thanks to my personal inspiration and role model, Michele, who has always cared for me like a sister. I am looking forward to our new adventures together.

Finally, I could not be here if it was not for the continuous support on the many people I love in Spain. First, I cannot begin to express my gratitude to the members of the Hazte Industrial. Adriana, David, Noemí, Eli, and Paola, your constant support and humour have brightened every single day since I came to the US and I am positive that I would have gone insane if not for you. I also feel very grateful that playing the violin has led me to the most special human I know; my most complementary person and the one that understands me the most: Andrea. I am honored to have shared this friendship with her all these years and that she is still willing to keep walking my way with me, even if I keep deferring going back to Europe. Finally, to my parents, Francisco and Loli, I owe everything. I am extremely grateful to them for giving me an exceptional education and for instilling in me the principles of perseverance and hard work. I would also want to thank my brothers, Pablo and Fran, for not letting me overthink everything and for having a safety net for me to fall back on when I was the most vulnerable. To the rest of my family, I love you.

Not in my wildest dreams did I think grad school would go so well. As I prepare to move forward towards the next chapter, I already feel nostalgic of Georgia Tech and all its wonderful people. Thank you for everything. Farewell, Atlanta.

TABLE OF CONTENTS

List of Tables	xii
List of Figures	xiii
Summary	xx
Chapter 1: Introduction	1
Chapter 2: Background	4
2.1 Coverage Control	4
2.1.1 Coverage Control With Heterogeneous Robot Teams	9
2.1.2 Coverage of Time-Varying Density Functions	10
2.2 Robots and Arts	13
2.2.1 Artistic Robotic Painting	14
2.2.2 Emotionally Expressive Robotics	15
2.3 Conclusions	19
Chapter 3: Coverage Control With Heterogeneous Sensing Capabilities	20
3.1 Problem Statement	21
3.2 Heterogeneous Coverage	22
3.2.1 Gradient Descent	24

3.3	Communication Aware Heterogeneous Coverage	29
3.3.1	Gradient Descent	32
3.4	Experimental Results	35
3.4.1	Heterogeneous Coverage	36
3.4.2	Communication Aware Heterogeneous Coverage	41
3.5	Conclusions	47
Chapter 4: Coverage Control With Time-Varying Density Functions		50
4.1	Time-Varying Density Functions	51
4.1.1	Homogeneous Coverage of Static Density Functions	51
4.1.2	Time-Varying Densities	53
4.2	Constraint-Based Task Execution	54
4.2.1	Control Barrier Functions	55
4.2.2	Minimum-Energy Gradient Descent	56
4.2.3	Decentralized Constraint-Based Control of Multi-Robot Systems . .	57
4.3	An Exact and Decentralized Approach to Time-Varying Coverage	59
4.4	Simulations and Experimental Results	61
4.5	Time-Varying Coverage With Heterogeneous Sensing Capabilities	65
4.5.1	Time-Varying Heterogeneous Coverage	66
4.5.2	Time-Varying Communication-Aware Heterogeneous Coverage . .	72
4.6	Conclusions	75
Chapter 5: Multi-Robot Painting Through Colored Motion Trails		76
5.1	Density-Based Multi-Robot Control	78

5.1.1	Coverage Control	78
5.1.2	Coverage With Heterogeneous Painting Capabilities	79
5.2	From Coverage Control to Painting	82
5.3	Experimental Results With Projected Trails	84
5.4	Discussion	90
5.4.1	Color Distance	93
5.4.2	Chromospectroscopy	96
5.4.3	Statistical Results	99
5.5	Conclusions	101
Chapter 6: Emotionally Expressive Robotic Swarms		103
6.1	Emotionally Expressive Movement	104
6.2	Swarm Behavior Design	109
6.2.1	Collective Behavior	109
6.2.2	Individual Robot Control	112
6.3	User Study	115
6.3.1	Procedure	115
6.3.2	Results and Discussion	116
6.4	Robotic Implementation	121
6.5	Conclusions	124
6.A	Collective Swarm Behavior	125
6.A.1	Happiness	125
6.A.2	Surprise	127

6.A.3	Sadness	127
6.A.4	Anger, Fear and Disgust	128
6.B	Individual Robot Control	129
Chapter 7: Conclusions and Future Directions		131
References		154

LIST OF TABLES

3.1	Sensor modalities for the experiments comparing gradient descent on \mathcal{H}_{het} with a heterogeneous version of Lloyd’s algorithm.	37
3.2	Density parameters for the experiments comparing gradient descent on \mathcal{H}_{het} with a heterogeneous version of Lloyd’s algorithm.	38
3.3	Comparison of the observed total cost comparing gradient descent on \mathcal{H}_{het} with a heterogeneous version of Lloyd’s algorithm.	39
3.4	Sensor configuration and density parameters for the experiments comparing \mathcal{H}_{het} and \mathcal{H}_{com}	44
5.1	Experimental parameters associated with the user-specified color density functions.	86
5.2	Paint equipment for the different experimental setups.	88
5.3	Color sectors throughout the painting used for the chromospectroscopy analysis, according to the density parameters specified in Table 5.1.	97
6.1	Movement and shape attributes associated with different emotions and emotion valences.	107
6.2	Motion and shape attributes selected for the behaviors associated with the fundamental emotions.	115
6.3	Confusion matrix calculated with the survey responses.	117

LIST OF FIGURES

2.1	Centroidal Voronoi tessellations achieved in simulation by a team of 25 differential-drive mobile robots covering a rectangular domain according to the control law in (2.5). In (a), the multi-robot team is tasked with covering the domain according to a uniform density function, i.e. all the points in the domain have equal importance. A bivariate Gaussian density function is used in (b) to represent a situation where the center of the domain is more important than the areas near the borders, where higher values of density are depicted through a darker shade of blue. In both situations, the Voronoi cells are depicted through black lines.	8
3.1	Regions of dominance for four neighboring robots with respect to Sensor 1, (a), and Sensor 2, (b). In this example, the sensing performance in a point $q \in \mathcal{D}$ degrades with the square of the distance to the robot: $f_j(d_j(p_i, q)) = \ p_i - q\ ^2$, $i \in \{1, \dots, 4\}$, $j \in \{1, 2\}$. For each Sensor j , the resulting regions of dominance, V_i^j , are Voronoi cells generated by those robots equipped with the sensor.	30
3.2	Evolution of the cost $\mathcal{H}_{het}(p(t))$ with respect to time in Experiment 4. The difference between the cost for heterogeneous Lloyd's and the proposed gradient descent in Theorem 3.2 arises from ignoring the boundary terms in (3.11) necessary to minimize the heterogeneous cost. Note that the increase in cost around $t = 40$ is due to the fact that the algorithm assumes single integrator dynamics while the actual robots are subject to nonholonomic constraints.	39
3.3	Effect of the regularizer term, σ , on the final configuration of the robot team for the sensor configuration of Experiment 4. As specified in Table 3.2, Robots 1 and 2 share the same density function, as do Robots 5 and 6. We can observe how, as the value of the regularizer decreases, the coordination between agents vanishes, making the robots that share the same objectives crowd together.	40

- 3.4 A group of ten GRITSBots executing the control law in Theorem 3.2—gradient descent on \mathcal{H}_{het} —with $\sigma = 0.975$, (a), versus a pure coordination algorithm, with $\sigma = 1$, (b). An overhead projector is used to visualize relevant information in the robot arena. For Robot i , the filled circle represents the center of mass of its Voronoi cell, c_i , while the centers of mass on the boundary, ρ_{ij} , $j \in \mathcal{N}_i$, are depicted using crosses at the boundaries of the cells. For this experiment, each robot has a unique sensor configuration with only one sensor. The location of the mean of the associated density function, $\phi_{s(i)} = \phi_i$, corresponds to the empty circle labeled with the robot’s numerical identifier. Making $\sigma = 1$ implies the sole consideration of the coordination term in the control law, which may result in some robots staying in areas with low information density, as in (b). This situation is alleviated by making $\sigma < 1$ in the control law and therefore involving the term \mathcal{H}_O , which allows the robot team to attain a better spatial configuration in the domain, (a). 42
- 3.5 Evolution of the global performance cost, \mathcal{H}_G , for the proposed gradient descent algorithm in Theorem 3.2 and the controller without communications in Theorem 3.3. We can see how, throughout the six experiments, the cost attained by the proposed controller is consistently equal or smaller than the one attained by the other controller. The performance difference is particularly acute in the case of Experiment 5, where the controller that does not consider communications converges to a critical point of its cost that does not correspond to a good overall coverage of the domain. 46
- 3.6 Final configurations of the multi-agent team for Experiments 2, 4 and 6. Figures (a), (c) and (e) correspond to the coverage control algorithm in Theorem 3.2, while Figs. (b), (d) and (e) illustrate the final spatial allocation of the team when running the algorithm in Theorem 3.3, which includes communications, for the same sensor configurations and initial conditions. The parts of the domain shaded with the different colors represent the areas of highest density, with each color identifying a different sensing modality. Each robot has a collection of symbols located to its right, which represents its sensor equipment and is color coded according to the associated density functions. With respect to the specifications in Table 3.4, the colors—blue, red, green, orange, and purple—correspond to the numerical identifiers 1 to 5 in the sensor equipments. 49

4.1	Evolution of the integral of the cost, $J(p, t)$, over time for the proposed constraint-based approach, Lloyd's algorithm [43] as well as the centralized and decentralized controllers in Lee <i>et al.</i> [83]. The final value of the cumulative cost for the proposed algorithm is very similar (although slightly lower) to the controllers that consider the effects of the time-varying densities by Lee <i>et al.</i> Ignoring the effects of a time-varying density function causes an appreciable difference in the case of Lloyd's algorithm. Inset highlights differences in costs towards the end of the experiment.	63
4.2	Comparison of the cumulative control effort for the proposed constraint-based approach, Lloyd's algorithm [43] as well as the centralized and decentralized controllers in [83]. While the performance of the algorithms in Lee <i>et al.</i> are similar to the proposed approach in terms of the final cost (see Fig. 4.1), the control effort required for the team to track the density functions is higher.	63
4.3	Snapshots from the time-varying coverage control experiment deployed on a multi-robot team operating on the Robotarium [191]. The time-varying density function is depicted by projecting its contour plot onto the testbed. As seen, using the constraint-based coverage algorithm, the robots track the centroids of their Voronoi cells, depicted as gray circles.	64
4.4	Evolution of the cost $J(p, t)$ for the proposed minimum energy coverage algorithm. The constraint-based approach drives the robots in a direction which reduces the overall coverage cost considered in (4.5) to zero. The temporary increases in the cost can be attributed to the fact that the robots have actuator constraints and thus cannot track arbitrarily high velocities generated by the optimization program. As the robots reduce the distance from the moving centroids of their Voronoi cells, the cost goes back towards zero.	65
5.1	A group of 12 robots generating a painting based on the densities specified by a human user for 5 different color tones: cyan, blue, pink, orange and yellow. The robots lay colored trails as they move throughout the canvas, distributing themselves according to their individual painting capabilities. The painting arises as a result of the motion trails integrating over time. . .	77

5.2	Painting mechanism based on heterogeneous coverage control. Each sub-figure shows the color trails laid by the robots (left) as they move to optimally cover a user-specified color density function (right) by executing the controller in (5.5). The symbols located to the right of the robot indicate its painting capabilities. Figures (a), (c) and (e) show the operation of the painting mechanism in Section 5.2 for a single robot equipped with all three colors, i.e. cyan (C), magenta (M) and yellow (Y), thus capable of producing all color combinations in the CMY basis. In (a), the robot lays a cyan trail according to the density color specification β_1 . The robot equally mixes magenta and yellow in (c) according to the color mixing strategy in (5.7), producing a color in between the two density color specifications, β_2 and β_3 . Finally, in (e), the robot exactly replicates the color specified by β_4 . On the other hand, Figures (b), (d) and (f) depict the operation of the painting mechanism with a team of 3 robots, where the Voronoi cells (color coded according to the CMY basis) are shown on the density subfigures.	85
5.3	Evolution of the painting according to the density parameters in Table 5.1, for the Setup 3 given as in Table 5.2. The robots distribute themselves over the domain in order to track the density functions as they evolve through the canvas. The color distribution of the color trails reflects the colors specified for the density functions within the painting capabilities of the robots. Even though none of the robots is equipped with the complete CMY equipment and, thus, cannot reproduce exactly the colors specified by the user, the integration of the colors over time produce a result that is close to the user's density specification.	87
5.4	Paintings generated for the densities in (5.8), with the team of 12 robots in their final positions. Figure 5.4a corresponds to a simulated painting and it is used for benchmarking. According to the painting equipment setups in Table 5.2 we can see how, as the robots in the team are equipped with more painting capabilities, the color gradients become smoother and more similar to the ideal outcome.	89
5.5	For each input color (given in Table 5.1): mean of the input density function (circle), and center of mass of the resulting color according to (5.12). The dotted lines depict the covariance ellipse according to (5.13). As seen the heterogeneity of the multi-robot team (as defined in (5.9)) impacts how far the colors are painted from the location of the input, as given by the user.	95
5.6	Average distance from mean density input to the resulting center of mass over the input colors of the painting as a function of the heterogeneity among the robots (as defined in (5.9)). As seen, with increasing sparsity of painting equipment on the robots (signified by increasing heterogeneity), the mean distance increases, indicating that colors get manifested farther away from where the user specifies them.	96

5.7	Chromospectroscopy by sectors on the canvas (as indicated in Table 5.3) for each equipment configuration (as specified in Table 5.2). With increasing heterogeneity, and consequently, sparser painting capabilities of the robots, colors distinctly different from the target colors begin to appear in each sector. For teams with lower heterogeneity (Setups 1-3), anomalous colors in the chromospectroscopy typically appear from neighboring sectors only.	98
5.8	Averaged paintings over 10 trials. Mean of the input densities (circle), center of mass of the resulting colors according to φ from (5.12) (square), and covariance ellipse (dotted lines). The heterogeneity in the painting equipment of the robots has a significant impact on the nature of the paintings.	100
5.9	Box plots of the average distance between mean density input to resulting center of mass as computed in (5.14) for the 9 different equipment configurations. The results are presented for 10 different experiments conducted for each equipment. As seen, the average distance increases with increasing heterogeneity among the robots' painting equipment.	101
6.1	The GRITSBot, a 3cmx3cm miniature mobile differential drive robot. The robotic swarm considered in this study is composed of 15 GRITSBots. The top view of these robots is used in the simulations shown to the study participants when evaluating the different swarm behaviors.	105
6.2	The behavior of a robotic swarm depends on which interactions are considered between the robots, which information is exchanged through those interactions, and how each robot acts on such information. Different interaction schemes and control laws produce distinct swarm behaviors.	108
6.3	Sequence of snapshots of the <i>happiness</i> behavior. Each robot follows a point that travels along a circular sinusoid, visually producing a circular shape with small ripples. The trajectories of five robots have been plotted using solid lines. See the full video at https://youtu.be/q_FenI1DdRY	110
6.4	Sequence of snapshots of the <i>surprise</i> behavior. The robots move along a circle of expanding radius, thus creating a spiral effect. The trajectories of five robots have been plotted using solid lines. See the full video at https://youtu.be/VYIJ5hBeOIU	110
6.5	Sequence of snapshots of the <i>sadness</i> behavior. The robots move along a small circle at a low speed. The trajectories of five robots have been plotted using solid lines. After 8 seconds, each robot has only displaced approximately an eighth of the circumference. See the full video at https://youtu.be/rfHZcFnRFg8	110

6.6	Sequence of snapshots of the <i>fear</i> behavior. The robots spread out uniformly over the domain. As it can be observed from the trajectories, they displace slowly with a non-smooth, angular movement trace. See the full video at https://youtu.be/jz-5INUd8wc	111
6.7	Sequence of snapshots of the <i>disgust</i> behavior. The robots spread out slowly towards the boundaries of the domain, with a trajectory with a non-smooth, angular trace. See the full video at https://youtu.be/EprfuCsuuRM	111
6.8	Sequence of snapshots of the <i>anger</i> behavior. The density function is defined as a Gaussian at the center of the domain, causing the robots to concentrate around this area. However, the fact that the robots move with high speed causes overshoots in their positions, thus producing a significantly angular movement trace. See the full video at https://youtu.be/kAGBrMkOtyY	111
6.9	Effect of the diffeomorphism parameter, l , on the movement trace of an individual robot. In all cases, the controller is following a particle that moves along the black dashed line—the desired trajectory. The top figure illustrates how an agent capable of executing the single integrator dynamics in 6.1 follows closely the desired trajectory. The other two trajectories, in blue, illustrate two different diffeomorphisms performed over the control action of the single integrator. In the middle, a small value of l results in an angular movement trace that follows quite closely the desired trajectory. In contrast, at the bottom, a large value of l results on a very smooth movement trace, at the expense of following more loosely the desired trajectory. . . .	114
6.10	Representation of the survey responses in the valence-arousal plane. The location of each emotion is represented with a color-coded cross according to the circumplex model of affect [167, 222]. Next to each emotion, a sequence of color-coded circles represent how the human subjects identify each behavior, with the diameter of each circle being proportional to the amount of responses given to the corresponding emotion. We can observe how, in general, the majority of users labels the behavior according to the signaled emotion, with most variations occurring generally with those emotions closest in the plane. In the cases of fear and disgust, while the relative majority of subjects still labels their behaviors according to the hypothesis, we observe a significant amount of confusion among them, which may be due to the proximity of such emotions in terms of valence and arousal. . . .	118

6.11	Percentage of subjects that identified each emotion in the video according to the hypothesis, classified according the robotics background of the subjects. There is no substantial difference between the responses given by the subjects that had experience studying or researching in robotics and those who did not.	119
6.12	Percentage of subjects that successfully assigned the emotion to the corresponding video, according to the hypothesis, according to the gender of the participants. We can observe how the responses of the female subjects are consistently more aligned with the hypothesized behavior for each of the videos.	119
6.13	Snapshots of the swarm behaviors implemented on a team of 12 GRITSBot X, taken in the Robotarium with an overhead camera that provides an analogous perspective to the one used in the simulations (Figs. 6.3 to 6.8). The trajectories of four robots have been plotted using solid lines. A link to the full video of each behavior is provided below each snapshot.	122
6.14	Snapshots of the swarm behaviors implemented on a team of 12 GRITSBot X in the Robotarium, from a perspective point of view. The snapshots, taken with a camera located 1.70m over the Robotarium surface, provide a similar angle view to that of a human spectator. A link to the full video is provided for each behavior.	123
6.15	Shapes selected for the happiness, surprise and sadness swarm behaviors. Each agent—here depicted as a red circle—follows a point (black circle) that moves along the dashed trajectory. The go-to-go controller that makes each agent follow the corresponding point is illustrated with blue arrows for 3 of the agents.	126
6.16	Density functions associated to represent the emotions of anger (a), disgust (b) and fear (c). The higher the density (darker color), the higher the concentration of robots will be in that area. The red circles represent the position of the agents once the control law in (6.7) has converged.	128
6.17	Parameters involved in the near-identity diffeomorphism in (6.10), used to transform the single integrator dynamics in (6.8) into unicycle dynamics (6.9), executable by the GRITSBots. The pose of the robot is determined by its position, $p = (x, y)^T$, and its orientation, θ . The single integrator control, u , is applied to a point \tilde{p} located at a distance l in front of the robot. The linear and angular velocities, v and ω , that allow the robot to track \tilde{p} are obtained applying the near-identity diffeomorphism in (6.10).	130

SUMMARY

Coverage control constitutes a canonical multi-robot coordination strategy that allows a collection of robots to distribute themselves over a domain to optimally survey the relevant features of the environment. This thesis examines two different aspects of the coverage problem. On the one hand, we investigate how coverage should be performed by a multi-robot team with a heterogeneous sensor equipment in the presence of qualitatively different types of events or features in a domain, which may evolve over time. On the other hand, we explore the use of coverage control as an interaction modality between artists and multi-robot systems for robotic swarms to be used in different forms of artistic expression.

In complex environments, a multi-robot team may need to simultaneously monitor multiple types of events or features throughout the domain of interest, which requires a mixture of sensors too extensive to be mounted into every single robot. This thesis investigates how to incorporate qualitatively different sensing modalities into the coverage formulation and how different communication schemes among the robots affect the coverage performance in such a scenario. In addition, having characterized the optimal spatial configurations for the multi-robot team, this thesis presents a constraint-based approach that allows the multi-robot team to cover different types of features whose locations evolve over time.

In contrast, the intersection of robotics and arts, which has been actively explored by both robotics researchers and artists, motivates the work in the second part of this thesis. In the context of swarm robotics in the arts, we investigate how the coverage paradigm, which affords the control of the entire multi-robot team through the high-level specification of density functions, can serve as an interaction modality for artists to effectively utilize robotic swarms. In particular, we explore the use of coverage control to create emotionally expressive swarm behaviors for robot theatre applications. Furthermore, the heterogeneous coverage framework developed in this thesis is employed to interactively control desired concentrations of color throughout a canvas for the purpose of artistic multi-robot painting.

CHAPTER 1

INTRODUCTION

Swarm robotics deals with how to coordinate large teams of robots to produce collective behaviors that go beyond the capabilities of the robots as individuals [1]. The operation of such robotic systems relies on the individuals executing control rules based on information obtained through local interactions, which altogether lead to a desired swarm behavior. This affords multi-robot systems desirable features such as redundancy, increased spatial coverage, flexible reconfigurability, or fusion of distributed sensors and actuators [2]; making them particularly suitable for applications such as precision agriculture, search-and-rescue operations, or environmental monitoring, among others [3]. In addition to these more conventional applications, robotic swarms have been commercially deployed as robotic toys [4] or to support performances in the entertainment industry [5].

Among the many decentralized control algorithms for multi-robot systems studied in the literature (see [3] for a survey), coverage control constitutes an attractive coordination strategy for many of the aforementioned applications, since it allows a collection of mobile robots to spatially distribute themselves according to the relative importance of different areas within a domain, typically defined by spatial fields and referred to as *density functions* in the literature [6, 7]. In addition to affording an optimal spatial allocation of the multi-robot team over a domain, the coverage approach enables an effective human-swarm interaction modality where a human operator can control the behavior of the swarm as a whole by specifying which areas of the domain it should roughly concentrate [8].

In the context of the coverage problem, this thesis deals with how to introduce heterogeneity in the problem formulation to reflect the capabilities of different robots in a natural manner when their sensing modalities are qualitatively different. Heterogeneity in multi-agent teams and its impact on their collective performance has been studied by researchers

of many disciplines, from the biological sciences, where insect societies benefit from behavioral specialization [9, 10], to business and sports management [11, 12, 13, 14, 15], where education and talent diversity, along with different cultural perspectives and experiences, contribute to disseminate and share knowledge in the teams. In robotic swarms, heterogeneous teams formed by robots that possess only a subset of the capabilities necessary to accomplish the global task may enable tackling much more complex tasks with presumably simpler, cheaper robots—as opposed to engineering robots with all the capabilities bundled together [16, 17, 18]. As a result, heterogeneous approaches have been proposed for a variety of multi-robot tasks including foraging [19], coverage [20, 21], collision avoidance [22] and task allocation [23]. Inspired by the beneficial effects of heterogeneity on collective performance, Chapter 3 studies how to perform coverage when there exist different types of events or features in the domain and the robots in the team have only a subset of the necessary sensors to monitor them, a novel problem in the coverage control literature.

The attractiveness of the coverage formulation, however, not only resides on its ability to achieve optimal surveillance of a domain in a distributed manner, but also on its amenability to human-swarm interaction, i.e. the intervention of a human on the autonomous operation of a robotic swarm to provide information inaccessible to the robotic system or to convey changes pertaining mission objectives [24]. In the coverage problem, the collective behavior of the swarm can be controlled by only specifying the density functions to be covered throughout the domain, which constitutes an intuitive, high-level command to be produced by a human [8]. Changes in the goal specification of the coverage problem, however, imply using dynamic density functions to describe the importance of the points on the domain. In Chapter 4, we introduce a constraint-based approach to the coverage of time-varying density functions—for both the homogeneous and the heterogeneous cases—that can be executed in an exact, decentralized fashion without imposing any conditions on the rate of change of the density functions.

Precisely, the amenability of coverage control as a modality for human-swarm interaction somewhat motivated in part the second half of this thesis. The intersection of robotics and arts has gain a lot of traction, with robots being consistently intertwined with multiple forms of art [25, 26]. In particular, for the case of robotic swarms, their aforementioned inherent properties (i.e. inexpensive platforms, flexible reconfigurability and increased spatial coverage) have propelled their commercial deployment for theatrical effects in performances [5, 27, 28]. This thesis explores the use of robotic swarms in artistic applications, with coverage as the main interaction modality between the artist and the robotic system. Using the framework developed in Chapter 3, in Chapter 5 the swarm is controlled by color densities throughout a canvas to produce artistic paintings. This chapter, furthermore, dives into the implications of using different levels of heterogeneity in the painting equipments and their impact on the resulting paintings that the robot team creates. In contrast, coverage is used with other standard multi-robot control strategies in Chapter 6 to produce expressive behaviors for robotic swarms to convey emotion in artistic expositions. These chapters thus illustrate how coverage can effectively serve as an abstraction for artists to control the overall behavior of a robotic swarms for different artistic purposes, without concerning themselves with low-level aspects of their control.

This thesis is organized as follows. In Chapter 3, we introduce heterogeneity in the coverage problem formulation to reflect qualitatively different sensing capabilities among the robots. Subsequently, Chapter 4 presents a constraint-based strategy for time-varying density functions that affords optimal coverage in an exact and decentralized fashion. The second part of the thesis moves onto the topic of swarm robotics and art, with coverage as the overarching interaction modality between the human artist and the robotic swarm for the two applications considered in this work, namely density-control painting and emotionally expressive motion, in Chapters 5 and 6, respectively. Chapter 7 concludes this thesis by outlining the main contributions and future work.

CHAPTER 2

BACKGROUND

This thesis investigates how a multi-robot team can be controlled to monitor different types of events over a domain, as well as how coverage can serve as an interaction modality between artists and robotic swarms for different forms of art expression. The objective of this chapter is to outline some of the existing work related to coverage control, as well as some literature on the intersection of robotics and arts. While each chapter in this thesis is self-contained, the aim of this chapter is to detail the coverage framework used throughout the thesis, as well as contextualize its findings. First, the formulation of coverage control used throughout this thesis is introduced. Variants of the coverage problem regarding heterogeneous multi-robot teams as well as coverage with respect to time-varying scalar fields are also included in this first half of the chapter, as they directly relate to the work presented in Chapters 3 and 4, respectively. Then, we move on to a summary on some of the existing work on the intersection of robotics and arts, with a focus on the types of artistic expression explored in Chapters 5 and 6 of this thesis, namely artistic painting and expressive movement.

2.1 Coverage Control

Coverage control concerns itself with the problem of distributing a collection of mobile sensor nodes across a domain in such a way that relevant environmental features and events are detected by at least one sensor node (with sufficiently high probability), e.g., [6, 29]. Different ways of encoding this have been proposed, including the construction of networks with particularly effective topologies, e.g., triangulations [30, 31], deployment according to spatial point processes with desired probability characteristics [32], and the partition of the domain into useful regions of dominance, where each node is in charge of covering its

own region [7].

In this thesis, we use the notion of optimal coverage developed by Cortés [6], which adapts concepts from locational optimization used for facility placement and resource distribution in operations research [33, 34, 35, 36] and is also related to territorial behaviors in observed in ecology [37, 38, 39] and cellular biology [40, 41, 42]. In particular, we consider a scenario where a team of N planar robots with positions $p_i \in \mathcal{D} \subset \mathbb{R}^2$, $i = 1, \dots, N$, are to cover a convex domain \mathcal{D} . A common strategy [6, 43] is to assign to each of the agents the surveillance of the points in the domain that are closest to it. If we let the position of Robot i in the team be denoted by $p_i \in \mathcal{D}$, $i \in \{1, \dots, N\} =: \mathcal{N}$, then Robot i has the responsibility of covering the set

$$V_i(p) = \{q \in \mathcal{D} \mid \|q - p_i\| \leq \|q - p_j\|, j \in \mathcal{N}\}, \quad (2.1)$$

where p is the combined positions of all the robots $[p_1^T, \dots, p_N^T]^T$ and $\{V_1(p), \dots, V_N(p)\}$ constitutes a Voronoi partition of the domain \mathcal{D} under the Euclidean metric [36].

Given a Voronoi partition of the domain into regions of dominance, one can now ask how well the team is actually covering the area. This question is typically asked relative to an underlying density function $\phi : \mathcal{D} \mapsto [0, \infty)$, which captures the relative importance of points in the domain, with $\phi(q) > \phi(\hat{q})$ meaning that q is more important, has a higher probability of being a place where an event will occur, or contains more relevant features than point \hat{q} , as discussed in [7]. If we furthermore assume that the sensing quality of each robot is isotropic and degrades with distance, the quality the coverage obtained in region $V_i(p)$ can be encoded through the cost

$$h_i(p) = \int_{V_i(p)} \|q - p_i\|^2 \phi(q) dq,$$

with a better coverage corresponding to a lower cost. Summing over all agents thus yields

the so-called *locational cost*

$$\mathcal{H}(p) = \sum_{i \in \mathcal{N}} h_i(p) = \sum_{i \in \mathcal{N}} \int_{V_i(p)} \|q - p_i\|^2 \phi(q) dq, \quad (2.2)$$

as described in [6] as a way of capturing the coverage performance.

A standard approach to minimize (2.2) is to let the individual robots move in a direction of descent of the gradient in order to minimize it [6, 7, 44], that is,

$$\dot{p}_i = -\gamma_i(p) \frac{\partial \mathcal{H}(p)}{\partial p_i}^T, \quad i \in \mathcal{N},$$

for some positive, possibly state-dependent, gain $\gamma_i(p)$, with the result that

$$\frac{d\mathcal{H}(p)}{dt} = -\frac{\partial \mathcal{H}(p)}{\partial p} \Gamma(p) \frac{\partial \mathcal{H}(p)}{\partial p}^T = -\left\| \frac{\partial \mathcal{H}(p)}{\partial p} \right\|_{\Gamma(p)}^2,$$

where $\Gamma(p) = \text{diag}(\gamma_1(p), \dots, \gamma_N(p))$ is a positive definite diagonal matrix. This descent formulation has two highly desirable properties, as discussed in [6]. On the one hand, it directly turns \mathcal{H} into a Lyapunov function, amenable to the application of LaSalle's invariance principle as a way of showing convergence to a stationary point. On the other hand, the distributed nature of the team is encoded through a Delaunay adjacency relationship [36]—Robots i and j only have to exchange information if they share a boundary in the Voronoi tessellation (as long as $\Gamma(p)$ does not introduce additional dependencies).

The gradient to $\mathcal{H}(p)$ can be computed by applying Leibniz integral rule [45], which contains terms involving the derivative of the integrands as well as the domains over which the integrals are defined. However, even though a small change in p_i results in a corresponding change to the boundary of the Voronoi cell $V_i(p)$, the net contribution from this change to the locational cost is offset by the corresponding changes to the locational cost from the boundaries of the adjacent Voronoi cells, given that the density function, $\phi(q)$, is common to all the agents and the total mass is conserved across \mathcal{D} . As a result, the do-

main terms in Leibniz rule cancel among neighbors and only the integrand terms must be considered when computing the gradient [29, 45], given by

$$\frac{\partial \mathcal{H}(p)}{\partial p_i} = 2 \int_{V_i(p)} (p_i - q)^T \phi(q) dq.$$

It is possible to express this gradient in a more compact form by defining the *mass* and *center of mass* associated with Robot i 's Voronoi cell as

$$m_i(p) = \int_{V_i(p)} \phi(q) dq, \quad c_i(p) = \frac{\int_{V_i(p)} q \phi(q) dq}{m_i(p)}, \quad (2.3)$$

which yields the gradient

$$\frac{\partial \mathcal{H}(p)}{\partial p_i} = 2m_i(p) (p_i - c_i(p))^T. \quad (2.4)$$

Moreover, by letting the gain be

$$\gamma_i(p) = \frac{\kappa}{2m_i(p)},$$

the scaled descent algorithm becomes the well-known Lloyd's algorithm [43],

$$\dot{p}_i = -\kappa(p_i - c_i(p)), \quad (2.5)$$

where $\kappa > 0$ is a proportional control gain. In fact, using LaSalle's invariance principle, Lloyd's algorithm has been shown to asymptotically achieve a centroidal Voronoi tessellation (CVT), i.e., a configuration where, asymptotically, $p_i = c_i(p)$, which in turn is a necessary condition for optimal coverage, as shown in [29]. Figure 2.1 shows two different CVTs achieved by the same team of mobile robots in a domain according to two different density functions, $\phi(q)$.

Many aspects of the coverage problem have been considered in the literature. Regard-

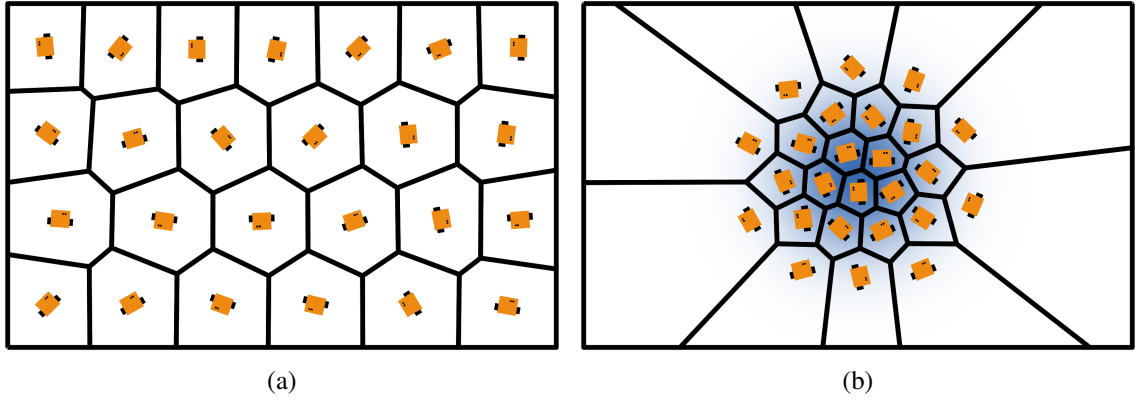


Figure 2.1: Centroidal Voronoi tessellations achieved in simulation by a team of 25 differential-drive mobile robots covering a rectangular domain according to the control law in (2.5). In (a), the multi-robot team is tasked with covering the domain according to a uniform density function, i.e. all the points in the domain have equal importance. A bivariate Gaussian density function is used in (b) to represent a situation where the center of the domain is more important than the areas near the borders, where higher values of density are depicted through a darker shade of blue. In both situations, the Voronoi cells are depicted through black lines.

ing the domain to be surveyed, authors have studied the coverage of non-convex [46], non-Euclidean [47], time-varying [48, 49], cluttered [50, 51], and structured environments [52, 53]. The density to be monitored by the team within the domain has also been an object of study, with a prominent focus on dealing with initially unknown density distributions, a problem often tackled through a simultaneous estimation and coverage through a series of control theory strategies [54] as well as statistical inference or learning [55, 56, 57, 58, 59, 60, 61]. With respect to the capabilities of the robots, authors have studied how to perform coverage when the team presents different kinematic configurations [62], mixed ground-aerial platforms [63], power constraints [21, 64] or sensor limitations [65, 66, 67, 68]. The adaptability of the sensors' performance to the environment has also been considered [69], as well as the application of the coverage framework to purely visual strategies, where specific camera performance measures have to be incorporated to reflect the particular aspects of position-fixed but reconfigurable orientations and focal parameters [69, 70], as well as visual sensors mounted on mobile robots [71, 72, 73].

Given that one of the pillars of this thesis is to investigate how coverage should be performed by teams where the individual robots are equipped with qualitatively different sensors—which constitutes the topic of Chapter 3—Section 2.1.1 presents a summary of how different types of heterogeneity in multi-robot teams have been previously considered in the formulation of the coverage problem. Furthermore, in relation to the framework introduced in Chapter 4, Section 2.1.2 presents an overview of existing solutions for the coverage of time-varying density functions.

2.1.1 Coverage Control With Heterogeneous Robot Teams

In many applications, individuals in a multi-robot team are rarely identical [74], as they may be equipped with different sensor suites, have varying levels of available energy, or the extent of wear and tear on the hardware may affect their performance. In the context of the coverage problem, a number of approaches considering heterogeneous teams have been proposed, focusing on sensor ranges or anisotropy [20, 75, 76], visibility limitations [46, 77], robot footprints [78, 79], and motion or sensor performance [21, 64, 79, 80] as the differentiating features among the robots. The heterogeneity among agents is usually encoded through a set of weights $w = \{w_1, \dots, w_N\}$ that result in a weighted Voronoi partition, the so-called *power diagram* [81],

$$P_i(p, w) = \{q \in \mathcal{D} \mid \|q - p_i\|^2 - w_i^2 \leq \|q - p_j\|^2 - w_j^2, \forall j \in \mathcal{N}\}.$$

Furthermore, the set of weights, w , are incorporated into the locational cost through the function that measures the distance between each robot and the points within its region of dominance,

$$\mathcal{H}_{power}(p, w) = \sum_{i \in \mathcal{N}} \int_{P_i(p, w)} (\|q - p_i\|^2 - w_i^2) \phi(q) dq. \quad (2.6)$$

This approach allows encoding many types of heterogeneity within the multi-robot team. However, the locational cost in (2.6) is restricted to scenarios where the density

function $\phi(q)$ is common to all the agents, that is, all the sensors measure the same types of features. One of the questions pursued in this research is how to introduce heterogeneity into this formulation in a way that reflects the capabilities of the different robots in a natural manner when the sensing modalities are qualitatively different, i.e., when there is no longer a single density function $\phi(q)$ that represents the importance of the points in the domain for all the robots in the team. In Chapter 3, we explicitly try to maintain some of the structural advantages afforded by the formulation of the coverage problem through a locational cost similar to the costs in (2.2) and (2.6), while capturing qualitatively different sensing capabilities distributed across the robots.

2.1.2 Coverage of Time-Varying Density Functions

In some coverage applications, the importance of the points in the domain may evolve over time due to, for example, the tracking of moving targets [29, 82] or new area objectives specified by a human operator [8, 83]. In these cases, it may be advantageous to preserve most of the structure of the coverage problem introduced in Section 2.1 and reflect the dynamic nature of these goals by considering the density function to be time-varying, $\phi : (q, t) \in \mathcal{D} \times \mathbb{R}_+ \mapsto \phi(q, t) \in \mathbb{R}_+$, which results in the following locational cost,

$$\mathcal{H}_{tv}(p, t) = \sum_{i=1}^N \int_{V_i(p)} \|q - p_i\|^2 \phi(q, t) dq, \quad (2.7)$$

where the subscript tv denotes the fact that the density function, ϕ , is *time-varying*.

Past approaches to the time-varying coverage problem rely on limitations on the rate of change of the density functions [29, 84, 85]. In particular, assuming the variation on the density is quasi-static [29], the multi-robot team can minimize (2.7) by letting each robot execute

$$u_i = \dot{c}_i(p, t) - \left(\kappa + \frac{\dot{m}_i(p, t)}{m_i(p, t)} \right) (p_i - c_i(p, t)), \quad \kappa > 0. \quad (2.8)$$

Analogously to the static case in (2.3), m_i and c_i represent the *mass* and *center of mass*,

defined here with respect to the time-varying density, $\phi(q, t)$,

$$m_i(p, t) = \int_{V_i(p)} \phi(q, t) dq, \quad c_i(p, t) = \frac{\int_{V_i(p)} q \phi(q, t) dq}{m_i(p, t)}. \quad (2.9)$$

The time derivatives in (2.8) are computed as follows,

$$\dot{m}_i = \int_{V_i} \dot{\phi}(q, t) dq, \quad \dot{c}_i = \frac{1}{m_i} \left(\int_{V_i} q \dot{\phi}(q, t) dq - m_i c_i \right),$$

where we have suppressed the dependencies m_i , c_i and their time derivatives on (p, t) and the dependency of V_i on p for notational convenience.

Motivated by the assumptions needed for (2.8) to render a stable controller in the presence of rapidly changing density functions, the restrictions on the rate of change of the density function $\phi(p, q)$ are lifted in [82], where the following control law is proposed to minimize the time-varying locational cost in (2.7),

$$u_i = \frac{m_i c_i + R_i - m_i p_i}{2 \|m_i c_i + R_i - m_i p_i\|^2} \left(\kappa m_i \|c_i - p_i\|^2 + F_i \right), \quad \kappa > 0, \quad (2.10)$$

with m_i and c_i defined as in (2.9). The term F_i results from the fact that the density function, $\phi(q, t)$, is time-varying and

$$F_i = (c_i - p_i)^T \int_{V_i} (2q - c_i - p_i) \dot{\phi}(q, t) dq,$$

while R_i accounts to variations caused by the displacement of the boundaries between Robot i and its neighbors,

$$R_i = \sum_{j \in \mathcal{N}_i} \left[\frac{1}{2} \int_{\partial V_{ij}} \phi(q) \frac{\partial q}{\partial p_i} n_q dq (c_i^T c_i - c_j^T c_j) - \int_{\partial V_{ij}} q \phi(q) \left(\frac{\partial q}{\partial p_i} n_q \right)^T dq (c_i - c_j) \right],$$

with ∂V_{ij} denoting the Voronoi boundary between Robots i and j and n_q , the outward facing normal vector to such boundary at point q . The efficacy of the control law in (2.10)

is demonstrated in simulation and experiments in [82]. However, no analytical guarantees are shown in [82] to guarantee that the controller u_i does not blow up as the robots approach a CVT.

The restrictiveness of the quasi-static approach in [29] and the lack of theoretical guarantees in [82] motivated a different approach in [83]. As illustrated in [83], considering the time-varying version of the cost in (2.7), one can achieve a CVT, without imposing conditions on the variation of $\phi(q, t)$, by setting

$$u = \left(I - \frac{\partial c}{\partial x} \right)^{-1} \left(\kappa(c(p, t) - x) + \frac{\partial c}{\partial t} \right), \quad (2.11)$$

where $u = [u_1^T, \dots, u_N^T]^T$ and $c = [c_1^T, \dots, c_N^T]^T$.

However, inverting the matrix $I - \frac{\partial c}{\partial x}$ in (2.11) cannot be done in a decentralized fashion. For this reason, in [83], the inverse is approximated by a truncated Neumann series as

$$\left(I - \frac{\partial c}{\partial x} \right)^{-1} \approx I + \frac{\partial c}{\partial x}$$

which allows each robot to evaluate its corresponding term based solely on information about its Delaunay neighbors.

In Chapter 4, we propose a constraint-based approach to the time-varying coverage problem that can be executed in an exact, decentralized fashion without imposing any conditions on the rate of change of the density functions. In addition, the proposed constraint-based strategy naturally lends itself composable with additional behaviors that could be concurrently executed by the multi-robot team, e.g. energy saving, collision avoidance [86].

2.2 Robots and Arts

The intersection of robots and arts has become an active object of study as both researchers and artists push the boundaries of the traditional conceptions of different forms of art [25, 26]. Robots have entered the realm of music, imitating human playing on preprogrammed musical pieces [87, 88, 89], enhancing the playing abilities of human musicians [90] or interactively playing or improvising alongside people [91, 92]. Dance has also been explored in the robotic context, with authors making robotic agents imitate structured human dances [93, 94], exploring the stylistic generation of dance patterns [95] and moving in real time according to music [96, 97]. Movement and engaging interactions between humans and robots has not been limited to dance, being also the object of study in the context of robot theater [98, 99, 100, 101] and stage support for visual performances [5, 102]. Robots are also capable of creating physical pieces of arts through artistic painting [103, 104] or by becoming art exhibits by themselves [105, 106, 107, 108, 109, 110].

On a smaller scale, the artistic possibilities of robotic swarms have also been explored in the context of choreographed or generated movements to music [5, 27, 111, 112], emotionally expressive motions [113, 114, 115, 116], interactive music generation based on the interactions between agents [117], or artistic paintings [118, 119, 120], among others. In this thesis, we explore coverage as an interaction modality between human artists and robotic swarms for two different artistic applications, namely interactive artistic painting, developed in Chapter 5, and emotionally expressive movement for performance support and robot theater, in Chapter 6. To this end, the remainder of this chapter provides a literature review on the topic of artistic robotic painting, as well as an overview on the expression of emotion and affect in robotic systems.

2.2.1 Artistic Robotic Painting

Advances in image processing and robotic control have opened up fascinating possibilities for researchers and artists, paving the way for new forms of artistic painting. Furthermore, in contrast to some other expressions of robotic art, robotic painting creates tangible pieces of art (paintings) which can be compared to other robot-created paintings—or even to paintings created by human artists.

In the context of robotic painting, the focus has been primarily on robotic arms capable of rendering input images provided to the robot setup. Monochromatic portraits, created as pen-an-ink drawings have drawn a significant amount of attention [121, 122], with some setups including additional control challenges such as drawing over arbitrary surfaces [123]. Some portrait setups, such as Paul the robot [104], reproduce face drawings of people based on observation, thus enhancing the human experience by providing the possibility of posing for a portrait. Along the lines of single-stroke painting, robotic painting has also been explored for the reproduction of handwritten characters [124, 125].

Realistic painting constitutes the preferred style in robotic painting literature, possibly due to the direct benchmarking that it affords. Robot Artist [126] has been used for the colorful reproduction of images, while ARTCYBE [127] has tackled realistic black and white paintings, diving into specific difficult techniques such as faithful tone rendition [128]. Other robotic applications on realistic painting have focused on the reproduction of the entire human painting process [129], exploring diverse grasps of different brushes. Realism has also favored exploring the use of Cartesian robots [130], in opposition to the extended use of robotic arms.

Alternative aesthetic and painting styles have also been approached in non-photorealistic robotic painting. The eDavid robot project [103] focused on simulating the entire human painting process, affording the use of multiple types of brushes or pencils, as well as physical colors ranging from ink to oil paint. Busker Robot, on the other hand, focused on the creation of watercolor painting, with changes in brush type, color dilution, etc. Later instal-

lations of both robots focused on different non-photorealistic techniques based on different types of strokes [131] and rendering techniques [132, 133]. The production of abstract paintings with similar robotic arm setups remains mostly unexplored, with some exceptions such as JacksonBot, a robot where the motion of the human hand has been analyzed to produce paintings in the style of Jason Pollock's [134].

Finally, robotic painting has not being exclusively related to the use of physical paint in the literature, with some authors exploring the use of quadrotors for single-stroke light painting in the space [135].

Robotic Swarm Painting

The idea of swarm painting has been substantially investigated in the context of computer generated paintings, where virtual painting agents move inspired by ant behaviors [136, 137, 138]. The creation of paintings with embodied robotic swarms, however, is lacking. Furthermore, in the existing instances of robotic swarm painting, the generation paradigm is analogous to those employed in simulation: the painting emerges as a result of the agents movement according to some behavioral, preprogrammed controllers [118, 119]. The robotic swarm thus acts in a completely autonomous fashion once deployed, which prevents any interactive influence of the human artist once the creation process has begun. Even in such cases where the human artist participates in the creation of the painting along with the multi-robot system [120], the role of the human artist has been limited to that of a co-creator of the work of art, since they can add strokes to the painting but their actions do not influence the operation of the multi-robot team.

2.2.2 Emotionally Expressive Robotics

As the integration of robots into domestic and public environments becomes a reality, there arises a need for robots to communicate in a familiar, socially intelligent manner, rendering their behavior recognizable to humans [139]. In order to effectively interact with a human, a

robot must convey emotion [140] and intentionality [141], i.e. the human must believe that the robot has beliefs, desires, and intentions [141]. In artistic applications, this requirement becomes essential: robots must be able to convey artistic expression an emotion to the audience, analogously to their human counterparts [142, 143].

Emotionally expressive interactions have been considered in the context of anthropomorphic robots [144], especially humanoids [99, 145, 146], and non-anthropomorphic robots [27, 147, 148], with different strategies being considered for the conveyance of emotional information. Laban Movement Analysis [149] has been adopted predominantly in robotic systems to express emotion through acceleration patterns [150, 151, 152, 153, 154, 155]. Additional movement features such as speed, smoothness or distance to obstacles have also been explored as ways to convey emotion [156]. Motor actions can also be used in conjunction with verbal cues [156], facial expressions [141] or touch [139, 157] to enhance the interaction between robots and humans. Lastly, the expressivity of the robotic system may not only be a result of the individual actions of the robot and the human, but also be influenced by the environment context [158].

Regarding robotic swarms, while its choreographed use to enhance stage performances has become quite popular in the last years [5, 27, 111, 102], the study of expressive interactions for this type of robotic systems remains sparse [114, 115, 116]. For these robotic platforms, however, authors have not only been constrained to movement descriptors common to individual robots (e.g. speed or smoothness), but have exploited the unique capabilities of robotic swarms in terms of synchronization [114] or standard collective algorithms [115, 116].

Emotion Models

For expressive robotic platforms, an intrinsically related question to that of *how to convey emotions* is that of *which emotions should be conveyed*. The question of which emotions are intrinsic to the human species and, thus, represent the basis for all the other emotions to

stem—possibly as a consequence of the cultural influence we experience in our respective societies—is certainly not restricted to these robotic applications, but rather constitutes an open question in the field of social psychology. As a consequence, authors have considered different emotion models when studying emotionally expressive robotic systems.

A prevalent model in the emotionally expressive robotics literature, both for anthropomorphic (e.g. [159]) as well as for non-anthropomorphic robots (e.g. [147]) is based on the so-called *fundamental* or *basic emotions*. Proposed by psychologists Ekman [160] and Izard [161], among others, this model contemplates six fundamental emotions—happiness, sadness, anger, fear, surprise and disgust, which are considered to be inherent to human mentality and adaptive behavior, and to remain recognizable across cultures [160, 161, 162].

Mehrabian’s emotional model [163, 164] has also been used in the robotics literature to provide a basis for which emotion basis to consider, both with physical [156] as well as for virtual agents [165]. The model, referred to as PAD emotional state model, classifies emotions as a function of three numerical dimensions: pleasure, arousal and dominance. The *pleasure/displeasure scale*—sometimes referred also as the *valence* of an emotion—designates the intrinsic attractiveness or aversiveness of an event, object or situation [166], and therefore characterizes its positive or negative connotation. The term *arousal scale* refers the activation or deactivation associated with an emotion and the *dominance-submissiveness* scale represents the prevalence of some emotions over others.

Finally, the P (pleasure/displeasure) and A (arousal/relaxation) scales of Mehrabian’s PAD model constitute the base for the circumplex model of affect proposed by Russell [167], which considers these dimensions orthogonal. Russell’s model has also been considered in the robotics literature, together with Ekman’s and Mehrabian’s emotion classifications, or by itself, e.g. [153].

Abstract Emotional Descriptors

A robotic swarm is comprised of a high number of relatively simple robots capable of reconfiguring themselves in a surface (planar robots) or in a volume (aerial robots) according to application objectives. However, the individual robots in a swarm typically have non-anthropomorphic, non-reconfigurable bodies, which can pose limitations in their expressivity when trying to apply strategies developed for robots with anthropomorphic traits such as faces, torsos or limbs. Given these limitations, this section outlines abstract shape and motion descriptors associated with different emotions in the social psychology literature [168].

Emotions can be attributed to kinematic features of abstract objects such as speed, acceleration or smoothness of the motion. Indeed, average speed and movement time are considered strong features in affect attribution [169, 170, 171, 172], especially with respect to its arousal [170]: increased speed is associated with emotion with high arousal (e.g. anger, happiness) [170] and smaller, slower movements are connected to low arousal (e.g. fear or sadness) [170, 172, 173, 174]. Movement acceleration also affects the emotion sensing, with acceleration being proportional to the perceived emotion arousal [171]. On the other hand, the smoothness or angularity of the movement trace of an object is often related to emotion valence, with smoother movements evoking pleasant emotions [169, 171, 175, 176].

In addition, static features of an abstract object may also influence emotion attribution. Similarly to the movement trace, the shape contour of an object also affects its emotive perception [175, 177, 178]. Generally, rounded shape contours are related to positive emotions and angular shapes, to negative ones—with the exception of sadness, a negative emotion that is associated with rounded shapes [179]. The size of an object also affects its emotive perception, with the surface area of a shape being directly entailing increased potency, i.e. higher arousal [175].

2.3 Conclusions

This chapter outlined the formulation of the coverage control problem used throughout this thesis, based on the works of Cortés [6]. This coverage formulation serves as the framework for the coverage of heterogeneous and density-functions, which constitute the object of interest of Chapters 3 and 4. In this context, this chapter has also provided a review of relevant work in the robotics literature related to different types of heterogeneity in the problem of coverage, as well as how dynamic density functions have been approached in the past.

The second part of this thesis deals with artistic robotic swarm applications based on coverage control as the interaction modality between the swarm and the human artist. This chapter outlined the body of work related to artistic robotic painting, including the sparse work on painting with robotic swarms. Regarding emotionally expressive robotic swarms, the chapter offered an overview of different strategies used to create emotionally expressive interactions between humans and robots, as well as a brief summary of different emotion models and emotion descriptors, both from the social psychology literature.

CHAPTER 3

COVERAGE CONTROL WITH HETEROGENEOUS SENSING CAPABILITIES

The problem of coverage for multi-robot teams deals with the positioning of a team of robots in a domain of interest such that the environmental features in the domain are monitored by at least one of the robots in the team [6, 7, 44, 20]. Many aspects of the coverage problem have been explored in the literature, including limitations on the robots' motion performance [21, 64], variations on the environmental features present in the domain [83], or geometric characteristics of the sensor footprint [65, 66], among others. However, the robots are often interchangeable in terms of the kind of features they monitor, i.e., all the robots in the team are equipped with the same sensing modalities, thus being able to detect the same events in the domain, even when differences arise between the robots in terms of performance [20, 78].

In complex environments, a multi-robot team may need to simultaneously monitor multiple types of features (e.g. radiation, humidity, temperature [180]), which require a mixture of sensing capabilities too extensive to be designed into a single robot [181]. As an alternative, each robot may be equipped with a subset of those sensors as long as, collectively, the team has all the sensor modalities needed to monitor the collection of features in the domain. However, in that case, the formulation of the coverage control algorithm needs to account for the sensing capabilities of each of the robots in the team.

This chapter studies how to introduce heterogeneity into the coverage formulation in a way that reflects the capabilities of the different robots in a natural manner when the sensing modalities are qualitatively different. The chapter is organized as follows: Section 3.1 presents the heterogeneous coverage problem formulation that considers robots equipped with qualitatively different sensors. Two different approaches to the heterogeneous coverage problem are included in this chapter: Section 3.2 presents an approach where each

robot calculates its individual density function by composing the functions associated with its sensors, while, in Section 3.3, different domain partitions are established according to the sensing modalities in the team. Both strategies are compared experimentally in Section 3.4. Section 3.5 concludes the chapter.

3.1 Problem Statement

The question of how well a team of N planar robots with positions $p_i \in \mathcal{D} \subset \mathbb{R}^2$, $i = 1, \dots, N$, is covering a convex domain \mathcal{D} is typically asked relative to an underlying density function $\phi : \mathcal{D} \mapsto [0, \infty)$, which captures the relative importance of points in the domain, with $\phi(q) > \phi(\hat{q})$ meaning that q is more important, has a higher probability of being a place where an event will occur, or contains more relevant features than point \hat{q} , as discussed in [7]. In the homogeneous coverage problem from [6] (see Section 2.1 for details), the quality of coverage is encoded through the locational cost,

$$\mathcal{H}_{hom}(p) = \sum_{i \in \mathcal{N}} \int_{V_i(p)} \|q - p_i\|^2 \phi(q) dq,$$

where $\{V_1(p), \dots, V_N(p)\}$ constitutes a Voronoi partition of the domain \mathcal{D} under the Euclidean metric as defined in (2.1). We use the subscript *hom* here to explicitly refer to the fact that all the robots have the same sensing capabilities, i.e., the team is homogeneous.

This chapter pursues the question of how to introduce heterogeneity into this formulation in a way that reflects the capabilities of the different robots in a natural manner when the sensing modalities are qualitatively different. To this end, let \mathcal{S} be a set of sensory modalities, with each robot being equipped with a subset of these sensors, denoted by $s(i) \subset \mathcal{S}$, $i \in \mathcal{N}$. Moreover, for each sensor $j \in \mathcal{S}$, there is a corresponding density of events or features in \mathcal{D} that this particular sensor can detect. For example, a camera can detect color variations associated with wilting crops on a farm field, while chemical gas sensor arrays can be used to measure soil conditions [182, 183]. As a result, we no longer

have a single density function, but rather a class of functions $\phi_j : \mathcal{D} \mapsto [0, \infty)$, $j \in \mathcal{S}$, with $\phi_j(q)$ representing the importance of a point $q \in \mathcal{D}$ according to sensor $j \in \mathcal{S}$ [184, 185].

3.2 Heterogeneous Coverage

Given the class of density functions $\phi_j : \mathcal{D} \rightarrow [0, \infty)$, $j \in \mathcal{S}$, one can encode the heterogeneity among the sensing modalities by defining the density associated with point q as it pertains to Robot i as a combination of the densities associated with its sensor suite [184],

$$\phi_{s(i)}(q) = \bigoplus_{j \in s(i)} \phi_j(q), \quad (3.1)$$

where \oplus is an appropriately chosen composition operator. The choice of composition operator reflects how the densities from the different sensors on the robot should be combined in order to compute the overall density function. For example, one simple way to combine the density functions is a direct summation,

$$\bigoplus_{j \in s(i)} \phi_j(q) = \sum_{j \in s(i)} \phi_j(q),$$

where the relative importance of a point is reflected by the sum of its importance among different sensors. Another possible composition is to pick the maximum density value among the sensors on Robot i ,

$$\bigoplus_{j \in s(i)} \phi_j(q) = \max_{j \in s(i)} \phi_j(q).$$

This choice would ensure that the density associated with a point corresponds to the highest relative importance measured by its sensors.

In order to maintain the structural advantages afforded by the homogeneous formulation in Section 3.1 (see Section 2.1 for more details), where each robot can measure the relative position of its neighbors and has information about the density distribution to be covered,

a direct usage of the locational cost with the agent-dependent density function in (3.1) becomes,

$$\mathcal{H}_c(p) = \sum_{i \in \mathcal{N}} \int_{V_i(p)} \|q - p_i\|^2 \phi_{s(i)}(q) dq. \quad (3.2)$$

Note that, under this formulation, the original Voronoi partition as in (2.1) is employed,

$$V_i(p) = \{q \in \mathcal{D} \mid \|q - p_i\| \leq \|q - p_j\|, j \in \mathcal{N}\},$$

giving each individual robot the sole responsibility for its region of dominance. The reason for this is twofold, namely (a) a desire to recover as much as possible from the homogeneous coverage control case in terms of the structure of the derivations, and (b) the fact that *coordination* emerges explicitly from the regions of dominance—hence the subscript \mathcal{C} .

However, in the heterogeneous case, it is no longer true that whichever area Robot i does not cover outside of $V_i(p)$ is automatically covered by the adjacent robots. Since the robots may be equipped with different sensor suites, it may be necessary to let coverage responsibilities encroach on other robots' cells, i.e., we no longer have a strict partition of the domain into regions of dominance. In the extreme case, if Robot i is the only robot equipped with a particular sensor, and that sensor is needed to cover the whole domain (as well as possible), it is necessary to define an additional cost over the whole domain. As such, in order to let the agents embrace their *domain objectives*, denoted by the subscript \mathcal{O} , a different locational cost is needed,

$$\mathcal{H}_O(p) = \sum_{i \in \mathcal{N}} \int_{\mathcal{D}} \|q - p_i\|^2 \phi_{s(i)}(q) dq, \quad (3.3)$$

where each integral measures how well Robot i is covering the entire domain \mathcal{D} with respect to its particular sensor configuration.

Armed with these two different locational costs, we let the *heterogeneous locational*

cost be given by a convex combination of the costs in (3.2) and (3.3),

$$\begin{aligned}
\mathcal{H}_{het}(p) &= \sigma \mathcal{H}_C(p) + (1 - \sigma) \mathcal{H}_O(p) \\
&= \sigma \sum_{i \in \mathcal{N}} \int_{V_i(p)} \|q - p_i\|^2 \phi_{s(i)}(q) dq \\
&\quad + (1 - \sigma) \sum_{i \in \mathcal{N}} \int_{\mathcal{D}} \|q - p_i\|^2 \phi_{s(i)}(q) dq,
\end{aligned} \tag{3.4}$$

where $\sigma \in (0, 1]$ acts as a regularizer between the two competing objectives. We do not let $\sigma = 0$ since, with this choice, no coordination among agents is present. The effect of selecting different values of σ is further discussed in subsequent sections.

These changes in the locational cost, as compared to the homogeneous case, have significant implications for how the gradient should be computed. In the following sections, we untangle these implications and present a controller that achieves convergence to the critical points of the heterogeneous locational cost in (3.4), which constitutes a necessary condition for optimal, heterogeneous coverage.

3.2.1 Gradient Descent

If we were to obtain the gradient to the heterogeneous locational cost in (3.4), a descent direction that achieves a local minimizer could be computed for the robots. To this end, we compute the gradient to \mathcal{H}_{het} by considering the two locational costs \mathcal{H}_C and \mathcal{H}_O separately, starting with the former of the two.

Let \mathcal{N}_i encode the Delaunay neighborhood of Robot i , i.e., the set of agents whose Voronoi cells share a face with agent i 's Voronoi cell, as was done in [83]. We can now break $\partial \mathcal{H}_C / \partial p_i$ down into three terms, namely Robot i 's contribution, the contributions

from robots in \mathcal{N}_i , and the contributions from the remaining robots,

$$\begin{aligned} \frac{\partial \mathcal{H}_c}{\partial p_i}(p) &= \frac{\partial}{\partial p_i} \left(\int_{V_i(p)} \|q - p_i\|^2 \phi_{s(i)}(q) dq \right) \\ &+ \frac{\partial}{\partial p_i} \left(\sum_{j \in \mathcal{N}_i} \int_{V_j(p)} \|q - p_j\|^2 \phi_{s(j)}(q) dq \right) \\ &+ \frac{\partial}{\partial p_i} \left(\sum_{j \notin \mathcal{N}_i \cup \{i\}} \int_{V_j(p)} \|q - p_j\|^2 \phi_{s(j)}(q) dq \right). \end{aligned} \quad (3.5)$$

We immediately note that the last term in the above expression does not depend on p_i , and as such, will be zero. For the remaining terms, we need to recall Leibniz integral rule:

Lemma 3.1 (Leibniz Integral Rule [45]). *Let $\Omega(p)$ be a region that depends smoothly on p such that the unit outward normal vector $n(p)$ is uniquely defined almost everywhere on the boundary $\partial\Omega(p)$. Let*

$$F = \int_{\Omega(p)} f(q) dq.$$

Then,

$$\frac{\partial F}{\partial p} = \int_{\partial\Omega(p)} f(q) n(q)^T \frac{\partial q}{\partial p} dq,$$

where $\int_{\partial\Omega(p)}$ denotes the line integral over the boundary of $\Omega(p)$.

This expression needs to be connected to the coordination locational cost in (3.2). Assuming that V_i and V_j share a boundary, this boundary will be orthogonal to the line connecting the Voronoi cell generators, as is observed in [186]. In other words, for any point q on this boundary,

$$\left(q - \frac{p_i + p_j}{2} \right)^T (p_i - p_j) = 0.$$

Differentiating this with respect to p_i yields

$$(p_j - p_i)^T \frac{\partial q}{\partial p_i} = (q - p_i)^T. \quad (3.6)$$

As $(p_j - p_i)/\|p_j - p_i\|$ is the unit outward normal from V_i on this shared boundary, by dividing (3.6) by $\|p_j - p_i\|$ the term $n(q)^T \frac{\partial q}{\partial p}$ in the integrand of Lemma 3.1 is obtained.

Considering coverage control when mass conservation no longer holds is not new. For example, [46] considers coverage control with visibility constraints and, analogously to what was done in [46], we can calculate the gradient to \mathcal{H}_C by applying the Leibniz integral rule to (3.5),

$$\begin{aligned} \frac{\partial \mathcal{H}_C}{\partial p_i} &= 2m_i (p_i - c_i)^T \\ &\quad + \sum_{j \in \mathcal{N}_i} \int_{\partial V_{ij}} \|q - p_i\|^2 \frac{(q - p_i)^T}{\|p_j - p_i\|} \phi_{s(i)}(q) dq \\ &\quad - \sum_{j \in \mathcal{N}_i} \int_{\partial V_{ij}} \|q - p_j\|^2 \frac{(q - p_i)^T}{\|p_j - p_i\|} \phi_{s(j)}(q) dq, \end{aligned} \quad (3.7)$$

where we, for notational convenience, have suppressed the explicit dependence of p on ∂V_{ij} —the boundary between Voronoi cells V_i and V_j —and where $\int_{\partial V_{ij}}$ refers to the line integral evaluated along this boundary. Moreover, m_i and c_i are the *heterogeneous mass* and *center of mass* in Robot i 's Voronoi cell, given by

$$m_i = \int_{V_i} \phi_{s(i)}(q) dq, \quad c_i = \frac{\int_{V_i} q \phi_{s(i)}(q) dq}{m_i}. \quad (3.8)$$

From the definition of the Voronoi tessellation, all points on a boundary between cells are equidistant from the seeds for those cells, i.e., for all $q \in \partial V_{ij}$ we have that $\|q - p_i\| =$

$\|q - p_j\|$. Substituting $\|q - p_j\|$ by $\|q - p_i\|$ in (3.7) yields

$$\begin{aligned} \frac{\partial \mathcal{H}_c}{\partial p_i} &= 2m_i (p_i - c_i)^\top \\ &+ \sum_{j \in \mathcal{N}_i} \left(\int_{\partial V_{ij}} (q - p_i)^\top \frac{\|q - p_i\|^2}{\|p_j - p_i\|} \phi_{s(i)}(q) dq \right. \\ &\quad \left. - \int_{\partial V_{ij}} (q - p_i)^\top \frac{\|q - p_i\|^2}{\|p_j - p_i\|} \phi_{s(j)}(q) dq \right), \end{aligned}$$

where the integral terms simplify to

$$\sum_{j \in \mathcal{N}_i} \int_{\partial V_{ij}} (q - p_i)^\top \frac{\|q - p_i\|^2}{\|p_j - p_i\|} (\phi_{s(i)}(q) - \phi_{s(j)}(q)) dq. \quad (3.9)$$

From this, we directly see that the gradient of the coordination term differs from the one obtained in the homogeneous case. Since the densities are no longer the same in adjacent cells, the net increase over $V_i(p)$ caused by a small movement in p_i is not offset by the changes in adjacent Voronoi cells. Note though that if the density functions are identical for all robots, $\phi_{s(i)} = \phi_{s(j)}$, $i, j \in \mathcal{N}$, then the additional term cancels out and the homogeneous gradient (2.4) from Section 2.1 is immediately recovered.

In order to get the gradient expression in a more compact form, we introduce the total *mass* and *center of mass* (both interpreted in terms of line integrals) *on the boundaries* between Voronoi cells using the following notation,

$$\mu_{ij} = \int_{\partial V_{ij}} \frac{\|q - p_i\|^2}{\|p_j - p_i\|} \phi_{s(i)}(q) dq, \quad \rho_{ij} = \frac{\int_{\partial V_{ij}} q \frac{\|q - p_i\|^2}{\|p_j - p_i\|} \phi_{s(i)}(q) dq}{\mu_{ij}}. \quad (3.10)$$

Plugging these into (3.9) yields the derivative of (3.2) with respect to Robot i 's position

$$\frac{\partial \mathcal{H}_c}{\partial p_i}^\top = 2m_i (p_i - c_i) + \sum_{j \in \mathcal{N}_i} \mu_{ij} (\rho_{ij} - p_i) - \mu_{ji} (\rho_{ji} - p_i). \quad (3.11)$$

The computation of $\partial\mathcal{H}_O/\partial p_i$ is less involved as the area of integration is the entire domain \mathcal{D} , which does not depend on the position of the agents,

$$\frac{\partial\mathcal{H}_O}{\partial p_i} = \frac{\partial}{\partial p_i} \left(\int_{\mathcal{D}} \|q - p_i\|^2 \phi_{s(i)}(q) dq \right) = 2M_i(p_i - C_i)^T.$$

Here M_i and C_i denote the *mass* and *center of mass of the domain* according to the density function of agent i , i.e.,

$$M_i = \int_{\mathcal{D}} \phi_{s(i)}(q) dq, \quad C_i = \frac{\int_{\mathcal{D}} q \phi_{s(i)}(q) dq}{M_i}. \quad (3.12)$$

The gradient of the heterogeneous locational cost thus becomes

$$\begin{aligned} \frac{\partial\mathcal{H}_{het}}{\partial p_i}^T &= \sigma \frac{\partial\mathcal{H}_c}{\partial p_i}^T + (1 - \sigma) \frac{\partial\mathcal{H}_O}{\partial p_i}^T \\ &= 2\sigma m_i(p_i - c_i) + \sigma \sum_{j \in \mathcal{N}_i} \mu_{ij}(\rho_{ij} - p_i) - \mu_{ji}(\rho_{ji} - p_i) \\ &\quad + 2(1 - \sigma)M_i(p_i - C_i). \end{aligned} \quad (3.13)$$

Letting Robot i follow a negative gradient flow establishes the following heterogeneous gradient descent theorem.

Theorem 3.2 (Heterogeneous Gradient Descent [184]). *Let Robot i , with planar position p_i , evolve according to the control law $\dot{p}_i = u_i$, where*

$$\begin{aligned} u_i &= -2\kappa \left(\sigma m_i(p_i - c_i) + (1 - \sigma)M_i(p_i - C_i) \right) \\ &\quad - \sigma \kappa \sum_{j \in \mathcal{N}_i} (\mu_{ij}(\rho_{ij} - p_i) - \mu_{ji}(\rho_{ji} - p_i)). \end{aligned} \quad (3.14)$$

Then, as $t \rightarrow \infty$, the robots will converge to a critical point of the heterogeneous location cost in (3.4) under positive gain $\kappa > 0$.

Proof. From (3.13), we already know the form for the gradient. What remains to be shown

is that convergence to a critical point is indeed achieved.

Consider the total derivative of the locational cost

$$\frac{d\mathcal{H}_{het}(p)}{dt} = \sum_{i \in \mathcal{N}} \frac{\partial \mathcal{H}_{het}}{\partial p_i} \dot{p}_i = -\kappa \left\| \frac{\partial \mathcal{H}_{het}}{\partial p} \right\|^2 \leq 0.$$

For (3.26) to be zero, we need $\partial \mathcal{H}_{het} / \partial p = 0$, in which case the control law becomes $\dot{p}_i = 0$. By LaSalle's invariance principle, the multi-robot system converges to the largest invariant set contained in the set of all points such that $d\mathcal{H}_{het}(p)/dt = 0$, which are the critical points to the heterogeneous locational cost in (3.4). \square

Note that, unlike the homogeneous case, Centroidal Voronoi Tessellations (CVTs) are no longer the only critical points to the locational cost. Indeed, as it will be observed in Section 3.4, in some situations, placing the agents in a CVT may yield higher costs than non-CVT configurations. Determining whether the achieved critical point is a local minimizer to the locational cost is difficult to establish—this remains an open issue even in the homogeneous case [45].

3.3 Communication Aware Heterogeneous Coverage

In this section, we investigate how the performance of the heterogeneous coverage algorithm can be improved by letting the robots communicate about their sensing modalities. By allowing Robot i to know which of its neighbors share some of its sensing modalities, it can determine which robots it should share responsibility with when covering each of the associated density functions, $\phi_j, j \in s(i)$, thus ensuring that no robot is tasked with covering a region without the required sensing modalities.

Analogously to other multi-robot coverage problems [6, 20, 44, 83], we are on the quest of defining a locational cost, $\mathcal{H}_{com}(p)$, that quantifies the quality of the coverage as a function of the positions of the robots in the team. For a sensing modality, $j \in \mathcal{S}$, and corresponding density, ϕ_j , the quality of coverage performed by Robot $i, j \in s(i)$, can be

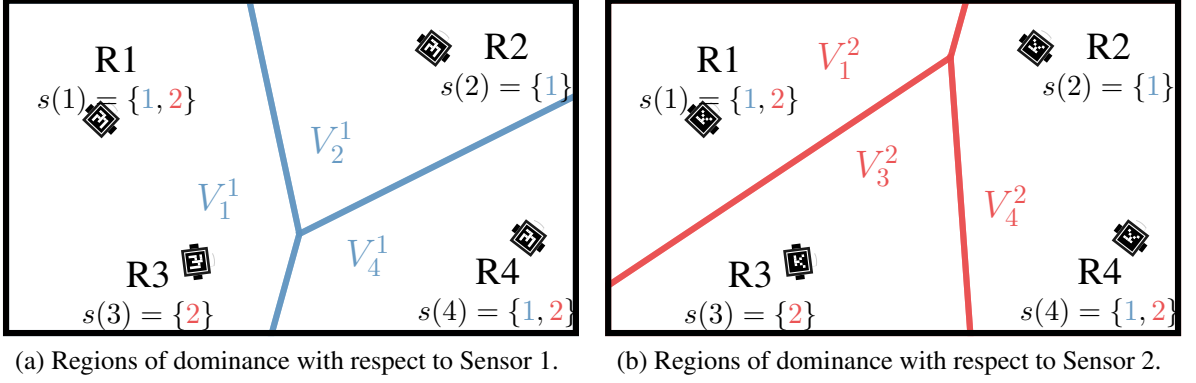


Figure 3.1: Regions of dominance for four neighboring robots with respect to Sensor 1, (a), and Sensor 2, (b). In this example, the sensing performance in a point $q \in \mathcal{D}$ degrades with the square of the distance to the robot: $f_j(d_j(p_i, q)) = \|p_i - q\|^2$, $i \in \{1, \dots, 4\}$, $j \in \{1, 2\}$. For each Sensor j , the resulting regions of dominance, V_i^j , are Voronoi cells generated by those robots equipped with the sensor.

encoded through the cost

$$h_i^j(p_i, V_i^j) = \int_{V_i^j} f_j(d_j(p_i, q)) \phi_j(q) dq, \quad (3.15)$$

where V_i^j is the region of dominance of Robot i with respect to Sensor j , $d_j : \mathcal{D} \times \mathcal{D} \mapsto \mathbb{R}$ measures the distance between robots and points in the domain, and $f_j : \mathbb{R} \mapsto \mathbb{R}$ is a smooth strictly increasing function that quantifies the degradation of the sensing performance with distance [20, 36]. The subscript j in d_j and f_j indicates they may be sensor dependent. Note that, for a system where the robots are equipped with different sensors, the region that Robot i is responsible for with respect to sensor j , V_i^j , can differ from the region to be monitored with respect to sensor k , V_i^k , $j, k \in s(i)$, depending on the sensor equipments of Robot i 's neighbors. An example of this for a four-robot, two-sensor scenario is shown in Fig. 3.1, where we can observe that the regions of dominance for Sensor 1, V_i^1 , differ from those of Sensor 2, V_i^2 , given that some robots are not equipped with those sensors and, thus, ignored when computing the corresponding regions of dominance.

In order to calculate the cost in (3.15), we need to determine what are the regions of dominance, V_i^j . By letting the robots communicate about their sensor suites, Robot i can

consider only the closest robots equipped with Sensor j (in terms of the distance function d_j) in order to calculate the boundaries of V_i^j . If we denote as \mathcal{N}^j the set of robots equipped with sensor j ,

$$\mathcal{N}^j = \{i \in \mathcal{N} \mid j \in s(i)\}, \quad \mathcal{N} = \{1, \dots, N\},$$

then the region of dominance of Robot i with respect to Sensor $j \in s(i)$ can be defined as a function of the positions of the robots according to the so-called *nearest-neighbor rule* [187],

$$V_i^j(p) = \{q \in \mathcal{D} \mid d_j(p_i, q) \leq d_j(p_k, q), \forall k \in \mathcal{N}^j\}.$$

The regions of dominance for Sensor j therefore correspond to the Voronoi partition generated by the robots in \mathcal{N}^j . Note that, if i is the only robot equipped with Sensor j , then the robot is in charge of covering the whole domain: $V_i^j = \mathcal{D}$.

With the regions of dominance defined, we can calculate the cost given by (3.15) for all the robots and all their sensors. With this information, the performance of the multi-robot team can be encoded through the *heterogeneous locational cost*,

$$\mathcal{H}_{com}(p) = \sum_{j \in \mathcal{S}} \sum_{i \in \mathcal{N}^j} \int_{V_i^j(p)} f_j(d_j(p_i, q)) \phi_j(q) dq, \quad (3.16)$$

with a lower value of the cost corresponding to a better coverage of the domain.

The proposed heterogeneous locational cost has two significant advantages when compared to the cost in [184]: On the one hand, the boundaries between the regions of dominance, $\partial V_i^j, i \in \mathcal{N}$, are defined with respect to the same density function, $\phi_j, j \in \mathcal{S}$, so that the cancellations that occur when applying Leibniz rule in the homogeneous case [6] will also take place when calculating the gradient of (3.16). On the other hand, when covering the density ϕ_j , a robot equipped with Sensor j will only relinquish the responsibility of an

area in the domain to a neighboring robot if the latter is also equipped with Sensor j and can perform a better coverage of such area (according to the functions d_j and f_j). This strategy thus ensures that no robot is ever in charge of covering a density over an area without the corresponding sensors and, as a result, there is no need to evaluate the performance of a robot over the whole domain, as was done in Section 3.2.

3.3.1 Gradient Descent

Having defined a locational cost that evaluates the quality of the coverage performed by the multi-robot team, we need to establish how the robots should move in the domain in order to minimize it. A standard approach to minimize the cost is to let each robot move in a direction of descent of the gradient, that is,

$$\dot{p}_i = -\gamma_i(p) \frac{\partial \mathcal{H}_{com}(p)^T}{\partial p_i}, \quad i \in \mathcal{N},$$

with $\gamma_i(p) > 0$ a gain for Robot i , which can depend on the position of the robots.

In order to calculate the derivative of the cost with respect to the position of Robot i , we need only to consider the terms associated with the sensor equipment of Robot i , $s(i)$,

$$\frac{\partial \mathcal{H}_{com}}{\partial p_i} = \frac{\partial}{\partial p_i} \left(\sum_{j \in s(i)} \sum_{k \in \mathcal{N}^j} \int_{V_k^j(p)} f_j(d_j(p_k, q)) \phi_j(q) dq \right), \quad (3.17)$$

given that the remainder terms in the first summation in (3.16) do not depend on p_i . Subsequently, for each sensor $j \in s(i)$, we can break down the expression in (3.17) in terms of the contribution of Robot i , its Delaunay neighbors with respect to such sensor, \mathcal{N}_i^j , and

the rest of the robots in \mathcal{N}^j ,

$$\frac{\partial \mathcal{H}_{com}}{\partial p_i} = \frac{\partial}{\partial p_i} \left(\sum_{j \in s(i)} \int_{V_i^j(p)} f_j(d_j(p_i, q)) \phi_j(q) dq \right) \quad (3.18)$$

$$+ \frac{\partial}{\partial p_i} \left(\sum_{j \in s(i)} \sum_{k \in \mathcal{N}_i^j} \int_{V_k^j(p)} f_j(d_j(p_k, q)) \phi_j(q) dq \right) \quad (3.19)$$

$$+ \frac{\partial}{\partial p_i} \left(\sum_{j \in s(i)} \sum_{\substack{k \in \mathcal{N}_i^j \\ k \notin \mathcal{N}_i^j \cup \{i\}}} \int_{V_k^j(p)} f_j(d_j(p_k, q)) \phi_j(q) dq \right), \quad (3.20)$$

where the term (3.20) is zero since it does not depend on p_i . Analogously to what was done in Section 3.2.1, we need to apply Leibniz integral rule (Lemma 3.1) to calculate the derivative of the first two terms.

The boundary of the region of dominance of Robot i with respect to sensor j , $\partial V_i^j(p)$, depends on p_i when a neighboring Robot k is also equipped with Sensor j , $k \in \mathcal{N}_i^j$. In this case we can denote as $\partial V_{ik}^j(p)$ the boundary between Robots i and k , with the points on that boundary satisfying the equality condition in the nearest-neighbor rule,

$$\partial V_{ik}^j(p) = \{q \in \mathcal{D} \mid d_j(p_i, q) = d_j(p_k, q), k \in \mathcal{N}_i^j\}. \quad (3.21)$$

Using this notation, we can write the derivative of (3.18) as

$$\sum_{j \in s(i)} \int_{V_i^j(p)} \frac{\partial f_j(d_j(p_i, q))}{\partial p_i} \phi_j(q) dq + \sum_{j \in s(i)} \sum_{k \in \mathcal{N}_i^j} \int_{\partial V_{ik}^j(p)} f_j(d_j(p_i, q)) \phi_j(q) n_{ik}^j(q)^T \frac{\partial q}{\partial p_i} dq, \quad (3.22)$$

where $n_{ik}^j(q)$, $q \in \partial V_{ik}^j(p)$, denotes the unit outward normal vector on the boundary between Robots i and k . Similarly, the derivative in (3.19) becomes,

$$- \sum_{j \in s(i)} \sum_{k \in \mathcal{N}_i^j} \int_{\partial V_{ik}^j(p)} f_j(d_j(p_k, q)) \phi_j(q) n_{ik}^j(q)^T \frac{\partial q}{\partial p_i} dq, \quad (3.23)$$

since the integrand of (3.19) does not depend on p_i and $n_{ik}(q) = -n_{ki}(q), \forall q \in \partial V_{ik}^j(p)$.

The integral terms over the boundaries in (3.22) and (3.23) cancel because the points on the boundary, $q \in \partial V_{ik}^j(p)$, satisfy the condition in (3.21) and therefore $f_j(d_j(p_i, q)) = f_j(d_j(p_k, q))$. Thus, the gradient of $\mathcal{H}_{com}(p)$ becomes,

$$\frac{\partial \mathcal{H}_{com}}{\partial p_i} = \sum_{j \in s(i)} \int_{V_i^j(p)} \frac{\partial f_j(d_j(p_i, q))}{\partial p_i} \phi_j(q) dq. \quad (3.24)$$

Letting Robot i follow a negative gradient descent establishes the following control law.

Theorem 3.3 (Communication Aware Heterogeneous Gradient Descent [185]). *Let Robot i , with planar position p_i , evolve according to the control law $\dot{p}_i = u_i$, where*

$$u_i = -\kappa \sum_{j \in s(i)} \int_{V_i^j(p)} \frac{\partial f_j(d_j(p_i, q))}{\partial p_i} \phi_j(q) dq \quad (3.25)$$

Then, as $t \rightarrow \infty$, the robots will converge to a critical point of the heterogeneous location cost in (3.16) under a positive gain $\kappa > 0$.

Proof. The form of the gradient is given in (3.24). Consider the locational cost $\mathcal{H}_{com}(p) > 0$ as a candidate function to prove convergence to a critical point. The total derivative of the locational cost is,

$$\frac{d\mathcal{H}_{com}(p)}{dt} = \sum_{i \in \mathcal{N}} \frac{\partial \mathcal{H}_{com}(p)}{\partial p_i} \dot{p}_i = -\kappa \left\| \frac{\partial \mathcal{H}_{com}(p)}{\partial p} \right\|^2 \leq 0. \quad (3.26)$$

The total derivative in (3.26) is zero if $\partial \mathcal{H}_{com}(p) / \partial p = 0$, in which case the control law becomes $\dot{p}_i = 0$. By LaSalle's invariance principle, the positions of the multi-robot system, p , will converge to the largest invariant set contained in the set of all points such that $d\mathcal{H}_{com}/dt = 0$, that is, the critical points to the heterogeneous locational cost in (3.16). \square

Note that, when the function d_j is defined as the Euclidean distance and the degradation

function, f_j , takes the square of that distance as in [6, 184], that is,

$$f_j(d_j(p_i, q)) = \|p_i - q\|^2, \forall i \in \mathcal{N}, j \in \mathcal{S},$$

then the control law in Theorem 3.3 becomes,

$$\dot{p}_i = 2 \sum_{j \in s(i)} m_i^j (c_i^j - p_i),$$

where m_i^j and c_i^j are defined as the *heterogeneous mass* and *center of mass* of Robot i with respect to sensor j ,

$$m_i^j = \int_{V_i^j(p)} \phi_j(q) dq, \quad c_i^j = \frac{\int_{V_i^j(p)} q \phi_j(q) dq}{m_i^j}. \quad (3.27)$$

Therefore, using the square of the Euclidean distance as the performance measure results in a controller that makes each robot move according to a weighted sum where each summation term corresponds to performing a continuous-time Lloyd descent as in [6] over the region of dominance corresponding to each of the sensors of the robot.

3.4 Experimental Results

The coverage control strategies for teams with heterogeneous sensing capabilities developed in this chapter were evaluated through a series of experiments. The performance of the heterogeneous coverage framework introduced in Section 3.2, where each robot calculates its individual density function, is evaluated against a heterogeneous version of Lloyd's algorithm in Section 3.4.1. Furthermore, the influence of the regularizer between the two competing objectives in \mathcal{H}_{het} in (3.4) as well as the effectiveness of the domain objectives cost are showcased in this section. The performance of the control laws in Theorems 3.2 and 3.3—corresponding to descent laws on \mathcal{H}_{het} and \mathcal{H}_{com} , respectively—are compared in Section 3.4.2 to show the effect of considering sensor-dependent partitions of the domain

afforded by the communications about the sensor suites among the robots.

3.4.1 Heterogeneous Coverage

The heterogeneous coverage algorithm proposed in Section 3.2 was implemented on the first version of the Robotarium [188], a remotely accessible swarm robotics testbed at the Georgia Institute of Technology, whose arena serves as the region to be covered by the robot team. The team was composed of six GRITSBots [189], which are miniature, differential-drive robots. A webcam-based tracking system provides information about the position and orientation of the different robots in the team. This information is fed to the control algorithm, which produces velocity commands for the robots.

As the descent algorithm ultimately produces desired velocities \dot{p}_i , $i \in \mathcal{N}$, an implicit assumption behind this construction is that the robot dynamics can be expressed as (or at least can execute) single integrator dynamics. But the differential-drive configuration does not directly support single integrator dynamics and, as such, the control commands resulting from Theorem 3.2 must be converted into suitable, low level inputs for the GRITSBots. To this end, let $p_i = (x_i, y_i)^T$ be the position of Robot i , and θ_i its orientation. Then, the differential-drive configuration can be modeled using unicycle dynamics,

$$\dot{x}_i = v_i \cos \theta_i, \quad \dot{y}_i = v_i \sin \theta_i, \quad \dot{\theta}_i = \omega_i,$$

where v_i and ω_i are the translational and rotational velocities to be commanded to the robot, respectively. Using a model similar to the one in [6], we can approximately convert the single integrator dynamics into unicycle dynamics as follows,

$$v_i = k_v [\cos \theta_i \quad \sin \theta_i] \dot{p}_i, \quad \omega_i = k_\omega \arctan \left(\frac{[-\sin(\theta_i) \quad \cos(\theta_i)] \dot{p}_i}{[\cos(\theta_i) \quad \sin(\theta_i)] \dot{p}_i} \right), \quad (3.28)$$

with k_v and k_ω positive gains.

To evaluate the control law in Theorem 3.2, its performance is compared to a baseline

Table 3.1: Sensor modalities for the experiments comparing gradient descent on \mathcal{H}_{het} with a heterogeneous version of Lloyd’s algorithm.

	Sensor modalities: \mathcal{S}	Robot sensors
Exp. 1	$\{1\}$	$s(i) = 1 \quad \forall i \in \mathcal{N}$
Exp. 2	$\{1, \dots, 6\}$	$s(i) = i \quad \forall i \in \mathcal{N}$
Exp. 3	$\{1, \dots, 6\}$	$s(i) = i \quad \forall i \in \mathcal{N}$
Exp. 4	$\{1, \dots, 4\}$	$s(1) = s(2) = 1$
		$s(3) = 2, s(4) = 3$
		$s(5) = s(6) = 4$

controller. To this end, we compare it to a heterogeneous version of Lloyd’s algorithm, whereby $\dot{p}_i = -\kappa(p_i - c_i(p))$, where c_i is evaluated using the heterogeneous densities as in (3.8). Given that the locational cost is an instantaneous measure, we moreover add a temporal component by evaluating the total cost of the controllers

$$\int_0^{t_f} \mathcal{H}_{het}(p(t)) dt$$

under identical initial conditions.

The experiment consists of four different configurations both in terms of the sensor suites assigned to the robots, $s(i)$, $i \in \mathcal{N}$, and the density functions associated with each sensor type, ϕ_j , $j \in \mathcal{S}$. The sensory capabilities of each robot are simulated using the overhead camera, which provides each robot with the information that its sensors would measure according to the corresponding density functions. Table 3.1 shows the sensor modalities for each experiment. In the first experiment, all the robots have the same sensor, therefore being in an equivalent configuration to the homogeneous case. Experiments 2 and 3 reflect situations where each robot has a unique sensor configuration, while in Experiment 4 some robots share sensor configurations.

Gaussian radial basis functions have been used in robotic networks to model sensors whose noisy signals represent physical quantities, such as magnetic forces, heat, radio

Table 3.2: Density parameters for the experiments comparing gradient descent on \mathcal{H}_{het} with a heterogeneous version of Lloyd’s algorithm.

		α_i		ν_i (cm)			
Agent	i	1	2	3	4	5	6
Exp. 1	$\beta_i = 1$			0			
				0			
Exp. 2	$\beta_i = i$			0			
				0			
Exp. 3	$\beta_i = 1$	−40	−20	0	0	20	40
		0	0	20	−20	0	0
Exp. 4	$\beta_i = 1$	−30	−30	0	0	30	30
		0	0	20	−20	0	0

signal, or chemical concentrations [190]. Following along these lines, for each sensor $j \in \mathcal{S}$, the corresponding density function is modeled as a bivariate normal distribution,

$$\phi_j(q) = \frac{\beta_j}{2\pi\sqrt{|\Sigma|}} \exp\left(-\frac{1}{2}(q - \nu_j)^T \Sigma^{-1}(q - \nu_j)\right),$$

where ν_j is the mean of the density and Σ is the covariance matrix, which is kept constant for all the sensors. β_j serves as a scale factor that models the strength of the density function. Table 3.2 indicates the density parameters used for each of the experiments, corresponding to the sensor modalities in Table 3.1. Note that the values for ν_j are measured with respect to the center of the Robotarium arena used in these experiments, a 120×70 cm rectangle.

Table 3.3 presents a comparison of the total cost observed for the four sensor configurations, where both the heterogeneous version of Lloyd’s algorithm and the descent law in Theorem 3.2 are executed for a total time of 2 minutes. Except for the first experiment, which corresponds to the homogeneous case, the total cost for the proposed algorithm is consistently smaller than the total cost attained by the heterogeneous Lloyd’s algorithm,

Table 3.3: Comparison of the observed total cost comparing gradient descent on \mathcal{H}_{het} with a heterogeneous version of Lloyd’s algorithm.

	Heterogeneous Lloyd’s	Gradient Descent
Exp. 1	0.14	0.14
Exp. 2	1.68	1.08
Exp. 3	0.70	0.61
Exp. 4	0.67	0.53

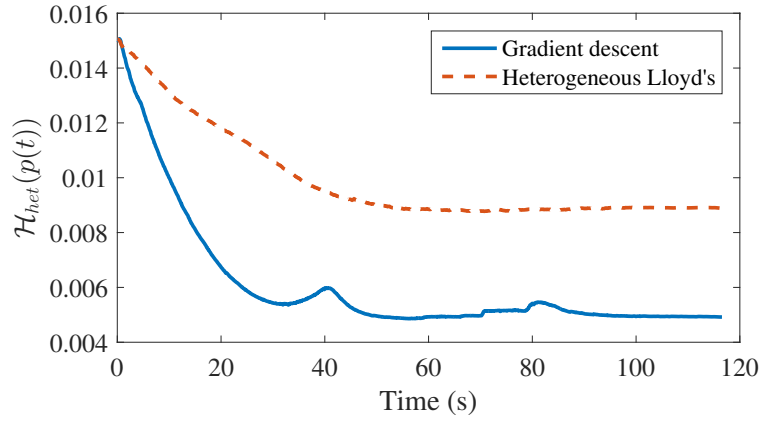


Figure 3.2: Evolution of the cost $\mathcal{H}_{het}(p(t))$ with respect to time in Experiment 4. The difference between the cost for heterogeneous Lloyd’s and the proposed gradient descent in Theorem 3.2 arises from ignoring the boundary terms in (3.11) necessary to minimize the heterogeneous cost. Note that the increase in cost around $t = 40$ is due to the fact that the algorithm assumes single integrator dynamics while the actual robots are subject to nonholonomic constraints.

which confirms that the control law in Theorem 3.2 is better suited for teams with heterogeneous sensing capabilities. The differences in performance between the two algorithms are also depicted in Fig. 3.2, where the absence of the boundary terms makes the heterogeneous version of Lloyd’s algorithm converge to a configuration with a higher final cost, showing that, for a heterogeneous cost, a CVT is not necessarily on its own a minimizer for the cost function.

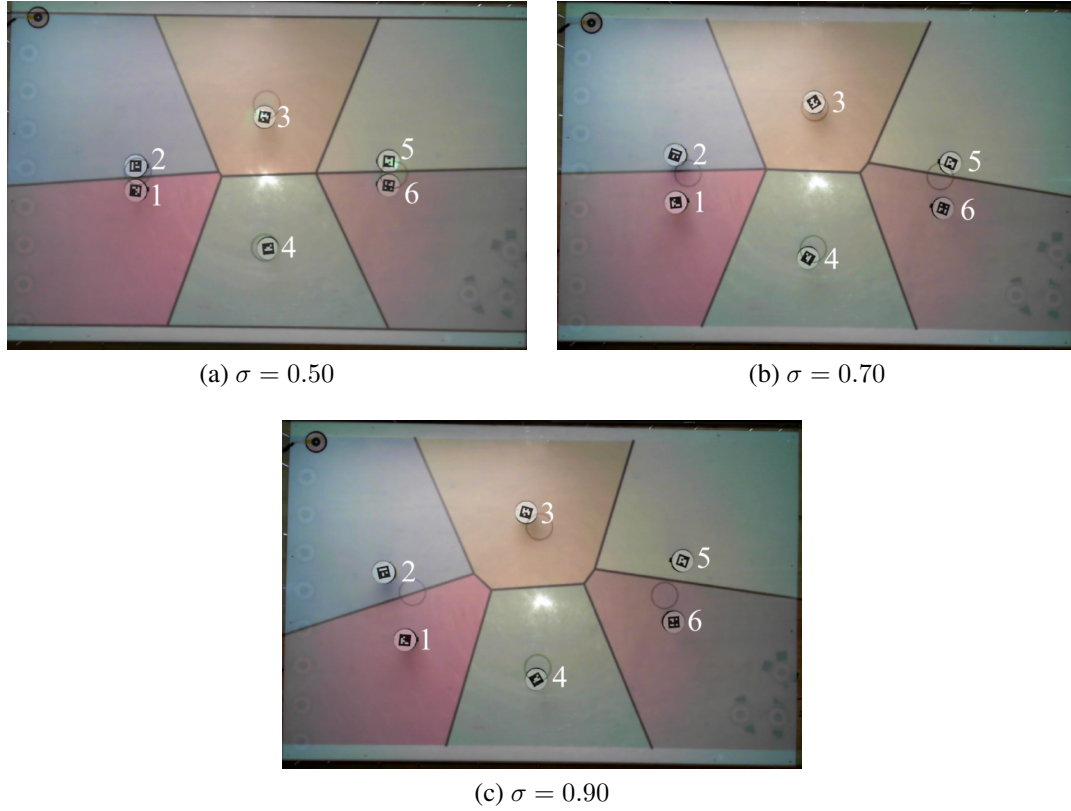


Figure 3.3: Effect of the regularizer term, σ , on the final configuration of the robot team for the sensor configuration of Experiment 4. As specified in Table 3.2, Robots 1 and 2 share the same density function, as do Robots 5 and 6. We can observe how, as the value of the regularizer decreases, the coordination between agents vanishes, making the robots that share the same objectives crowd together.

Effect of the Regularizer, σ

A value of $\sigma = 0.9$ is used in all four experiments. The value given to the regularizer σ is selected to favor the coordination component, \mathcal{H}_C , over the domain objectives. A comparison of the effect of different regularizer values on the behavior of the robot team for the sensor configuration of Experiment 4 is presented in Fig. 3.3, where we can observe that lower values of σ tend to excessively favor the domain objectives term, \mathcal{H}_O , concentrating the robots around their individual density functions and therefore reducing the coordinated nature of the coverage algorithm.

Effect of the Domain Objectives Cost, \mathcal{H}_O

A group of ten robots is used to illustrate the team behavior when $\sigma = 1$ in (3.14), that is, when the control law is solely determined by the gradient of the coordination cost, \mathcal{H}_C . In this case, the movement of a robot only depends on the values of its density function within its Voronoi cell and boundaries. Consequently, the team may be deterred from adequately covering an area associated with a particular density function, ϕ_j , if the robots equipped with the associated sensor, j , are located in areas with low values of the density ϕ_j , and are unable to move to higher density areas due to the position of their Delaunay neighbors, as shown in Fig. 3.4b.

In Section 3.2, \mathcal{H}_O was introduced as an additional locational cost to palliate the lack of coverage of areas outside each robot's region of dominance when the team is equipped with disjointed sets of sensors. The results from the convex combination of both locational costs, \mathcal{H}_O and \mathcal{H}_C , are shown in Fig. 3.4a. This situation illustrates how the proposed controller, thanks to the introduction of the domain objectives term, achieves a better spatial configuration of the agents in the domain while each robot still coordinates with the other members of the team.

3.4.2 Communication Aware Heterogeneous Coverage

The coverage performance of the two control laws for teams with heterogeneous sensing capabilities presented in this chapter are compared in this section. Both controllers were implemented on a team of ten GRITSBots [189] running in the Robotarium [191], where the code is uploaded via web interface and the experimental data can be retrieved after the experiment is finalized. On each iteration, the Robotarium interface provides information about the position and orientation of the robots in the team and allows to specify the linear and angular velocities to be executed by the robots.

An implicit assumption behind the controllers in both Theorems 3.2 and 3.3 is that each robot can move according to single integrator dynamics, $\dot{p}_i = u_i, \forall i \in \mathcal{N}$. Similarly

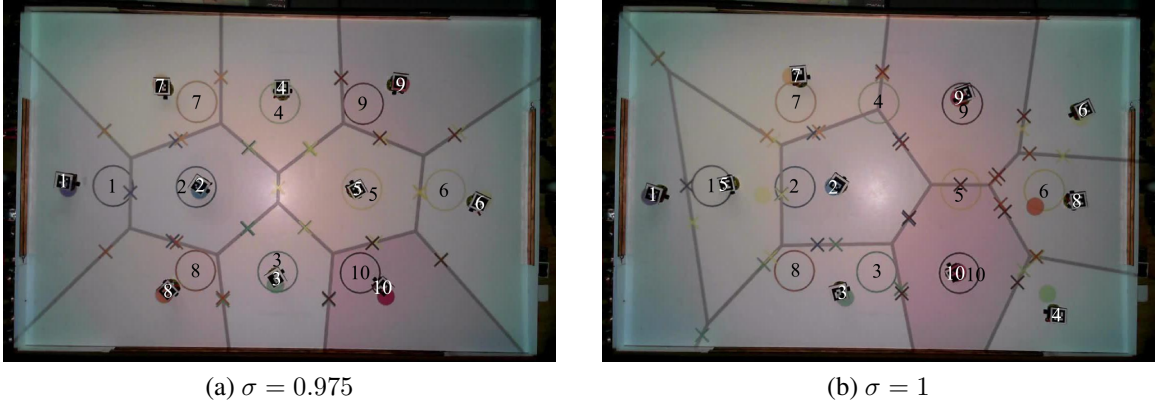


Figure 3.4: A group of ten GRITSBots executing the control law in Theorem 3.2—gradient descent on \mathcal{H}_{het} —with $\sigma = 0.975$, (a), versus a pure coordination algorithm, with $\sigma = 1$, (b). An overhead projector is used to visualize relevant information in the robot arena. For Robot i , the filled circle represents the center of mass of its Voronoi cell, c_i , while the centers of mass on the boundary, ρ_{ij} , $j \in \mathcal{N}_i$, are depicted using crosses at the boundaries of the cells. For this experiment, each robot has a unique sensor configuration with only one sensor. The location of the mean of the associated density function, $\phi_{s(i)} = \phi_i$, corresponds to the empty circle labeled with the robot’s numerical identifier. Making $\sigma = 1$ implies the sole consideration of the coordination term in the control law, which may result in some robots staying in areas with low information density, as in (b). This situation is alleviated by making $\sigma < 1$ in the control law and therefore involving the term \mathcal{H}_O , which allows the robot team to attain a better spatial configuration in the domain, (a).

to what was done in Section 3.4.1, the control commands produced by (3.25) must be converted into inputs executable by these differential drive robots, i.e., linear and angular velocity commands $(v_i, \omega_i), \forall i \in \mathcal{N}$. To that end, we here convert the single integrator dynamics produced by the two control laws into executable commands by the robots using the model in (3.28).

In order to evaluate the performance of both algorithms, and therefore the impact of introducing communications about sensor modalities, we define a baseline cost function which captures the team’s performance when global information is available, that is, the position and sensor equipment of all the robots. According to the nearest-neighbor rule [187], a point in the domain is best covered with respect to ϕ_j when its coverage is assigned to the closest robot equipped with sensor j , in which case the optimal coverage of the

density ϕ_j is given by,

$$\int_{\mathcal{D}} \min_{i \in \mathcal{S}^j} f_j(d_j(p_i, q)) \phi_j(q) dq,$$

with \mathcal{S}^j the set of all robots with sensor modality j ,

$$\mathcal{S}^j = \{i \in \mathcal{N} \mid j \in s(i)\}, j \in \mathcal{S}.$$

The performance of the team with respect to all the density functions, $\phi_j, j \in \mathcal{S}$, can be therefore obtained by adding the cost pertaining to each of the sensors, i.e.,

$$\mathcal{H}_G = \sum_{j \in \mathcal{S}} \int_{\mathcal{D}} \min_{i \in \mathcal{S}^j} f_j(d_j(p_i, q)) \phi_j(q) dq, \quad (3.29)$$

where G denotes the *global performance* of the team.

We use the cost in (3.29) as a baseline to compare the control laws Theorems 3.2 and 3.3, that is, the gradient descent flows that arise from considering the heterogeneous costs without and with communications among the robots about their sensor suites. In order to provide a fair assessment of their performance, the distance and degradation functions assigned to all the sensors in this section are defined as,

$$f_j(d_j(p_i, q)) = \|p_i - q\|^2, \forall j \in \mathcal{S}, i \in \mathcal{N},$$

given that the square of the Euclidean distance is the only sensing performance measured considered in Section 3.2.

The experiment consists on six different configurations of team sensors, \mathcal{S} ; robot sensors, $s(i), i \in \mathcal{N}$; and of the corresponding densities, $\phi_j, j \in \mathcal{S}$. The sensing capabilities of the robots are simulated based on the pose information provided by the tracking system, from which the corresponding sensing information is provided to each robot. The sensor

Table 3.4: Sensor configuration and density parameters for the experiments comparing \mathcal{H}_{het} and \mathcal{H}_{com} .

Experiment	Team Sensors	Robot Sensors	Density Functions (in cm)
1	$\mathcal{S} = \{1\}$	$s(i) = \{1\}, i \in \mathcal{N}$	$\phi_1(q) = \mathcal{G}(q, [0, 0]^T)$
2	$\mathcal{S} = \{1, 2\}$	$s(i) = \{1\}, i \in \{1, \dots, 5\}$ $s(i) = \{2\}, i \in \{6, \dots, 10\}$	$\phi_1(q) = \mathcal{G}(q, [-50, 0]^T)$ $\phi_2(q) = \mathcal{G}(q, [50, 0]^T)$
3	$\mathcal{S} = \{1, \dots, 10\}$	$s(i) = i, i \in \mathcal{N}$	$\phi_1(q) = \mathcal{G}([-55, 0]^T)$ $\phi_2(q) = \mathcal{G}(q, [55, 0]^T)$ $\phi_3(q) = \mathcal{G}(q, [-38, 38]^T)$ $\phi_4(q) = \mathcal{G}(q, [38, -38]^T)$ $\phi_5(q) = \mathcal{G}(q, [-38, -38]^T)$ $\phi_6(q) = \mathcal{G}(q, [38, 38]^T)$ $\phi_7(q) = \mathcal{G}(q, [-20, 0]^T)$ $\phi_8(q) = \mathcal{G}(q, [20, 0]^T)$ $\phi_9(q) = \mathcal{G}(q, [0, 40]^T)$ $\phi_{10}(q) = \mathcal{G}(q, [0, -40]^T)$
4	$\mathcal{S} = \{1, \dots, 5\}$	$s(1) = \{1\}$ $s(2) = \{2\}$ $s(3) = \{3\}$ $s(4) = \{4\}$ $s(5) = \{5\}$ $s(6) = \{1\}$ $s(7) = \{2\}$ $s(8) = \{3\}$ $s(9) = \{4\}$ $s(10) = \{5\}$	$\phi_1(q) = G(q, [-40, -40]^T)$ $\phi_2(q) = G(q, [-40, 40]^T)$ $\phi_3(q) = \mathcal{G}(q, [0, 0]^T)$ $\phi_4(q) = \mathcal{G}(q, [40, 40]^T)$ $\phi_5(q) = \mathcal{G}(q, [40, -40]^T)$
5	$\mathcal{S} = \{1, \dots, 4\}$	$s(1) = \{1, \dots, 4\}$ $s(2) = \{1\}$ $s(3) = \{1, 2\}$ $s(4) = \{1, 3\}$ $s(5) = \{1, 2, 4\}$ $s(6) = \{1\}$ $s(7) = \{1, 2, 3\}$ $s(8) = \{1\}$ $s(9) = \{1, 2, 4\}$ $s(10) = \{1, 3\}$	$\phi_1(q) = G(q, [0, 0]^T)$ $\phi_2(q) = \mathcal{U}(\mathcal{D})$ $\phi_3(q) = \mathcal{G}(q, [-60, 0]^T)$ $\phi_4(q) = \mathcal{G}(q, [-0, 40]^T)$ $\quad + \mathcal{G}(q, [0, -40]^T)$
6	$\mathcal{S} = \{1, \dots, 3\}$	$s(1) = \{1, 2, 3\}$ $s(2) = \{1, 2\}$ $s(3) = \{2, 3\}$ $s(4) = \{1, 3\}$ $s(5) = \{1\}$ $s(6) = \{1\}$ $s(7) = \{2\}$ $s(8) = \{2\}$ $s(9) = \{3\}$ $s(10) = \{3\}$	$\phi_1(q) = \mathcal{G}(q, [0, 40])$ $\phi_2(q) = \mathcal{G}(q, [-34, -20]^T)$ $\phi_3(q) = \mathcal{G}(q, [34, 20]^T)$

and density configurations used for each experiment are included in Table 3.4. Except for a uniform density, $\mathcal{U}(\mathcal{D})$, used in Exp. 5, all the density functions are bivariate normal distributions as used in [6, 44], where the covariance matrix, Σ , is kept constant for all the experiments. The notation used in Table 3.4 indicates the location of the mean,

$$\mathcal{G}(q, \mu) = \frac{1}{2\pi\sqrt{|\Sigma|}} \exp\left(-\frac{1}{2}(q - \mu)^T \Sigma^{-1}(q - \mu)\right).$$

The evolution of the global performance cost for the six experiments is shown in Fig. 3.5, where, for all the cases, the critical point attained by the proposed controller corresponds to a lower value of the performance measure in (3.29) with respect to the controller without communications.

The final spatial configurations attained by both algorithms correspond to critical points of their corresponding locational costs. Final allocations of the team for Experiments 2, 4 and 6, run under identical initial conditions, are compared in Fig. 3.6. In Experiment 2, the team is in charge of covering two density functions, with half of the robots assigned to each of them and no robot being in charge of both. Without communications (Fig. 3.6a), most of the robots are located close to their area of higher density, with the exception of a pair that establish a Voronoi boundary regardless of them not sharing any sensing capabilities. This situation is not observed running the proposed algorithm, Fig. 3.6b, given that boundaries are only established among robots equipped with the same sensors.

In Experiment 4, the team is divided in pairs to cover five different densities. As shown in Fig. 3.6c, having no communications about their sensing capabilities again results in two robots establishing a boundary with a neighbor without common sensors. Given that the gradient points each of these robots perpendicularly to their boundary, the team settles in this critical point. In contrast, the proposed algorithm (Fig. 3.6d), achieves a satisfactory spatial configuration where the robots are located in areas of high interest according to their sensors. In fact, the boundary of the regions of dominance for each pair crosses the

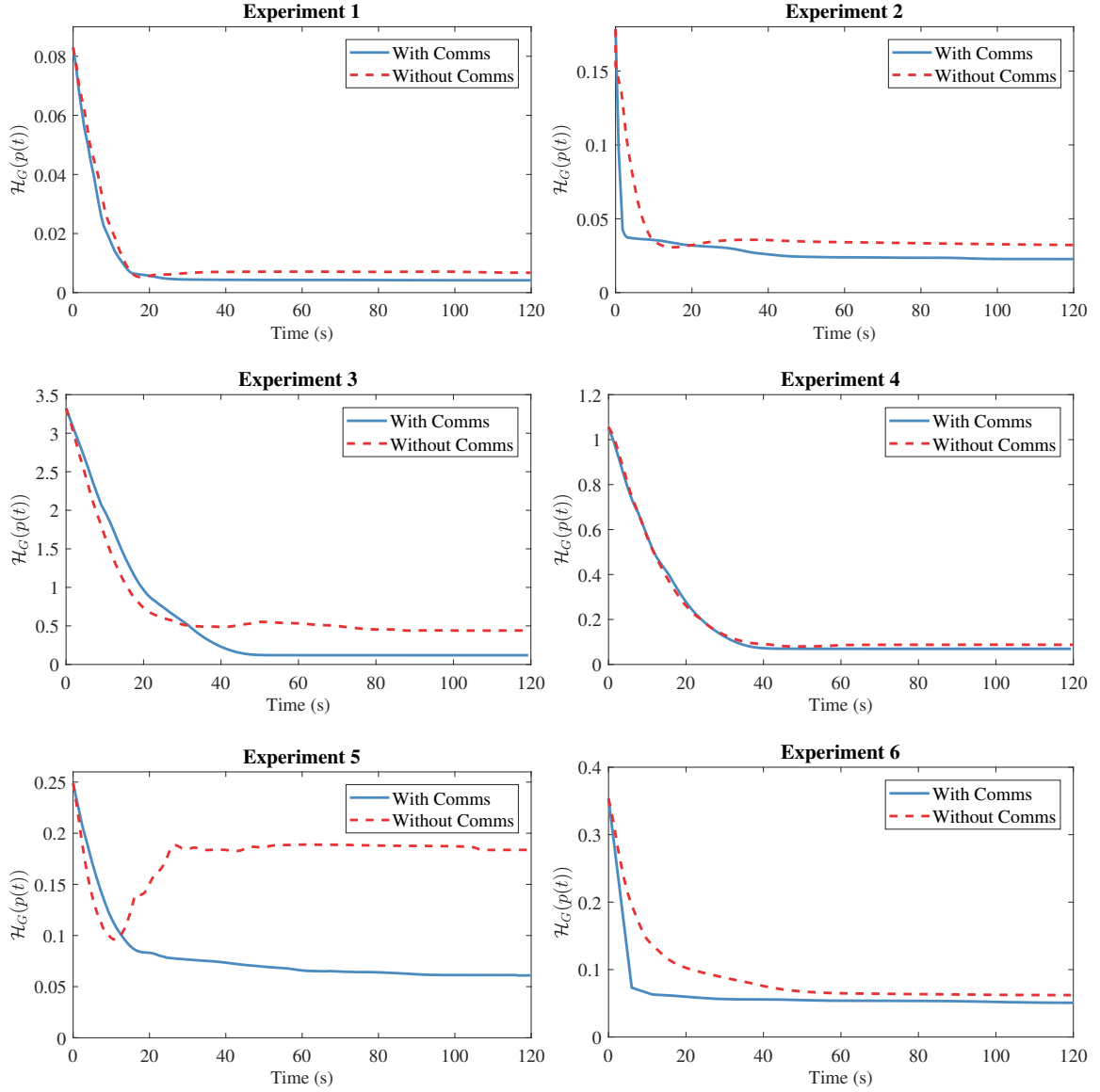


Figure 3.5: Evolution of the global performance cost, \mathcal{H}_G , for the proposed gradient descent algorithm in Theorem 3.2 and the controller without communications in Theorem 3.3. We can see how, throughout the six experiments, the cost attained by the proposed controller is consistently equal or smaller than the one attained by the other controller. The performance difference is particularly acute in the case of Experiment 5, where the controller that does not consider communications converges to a critical point of its cost that does not correspond to a good overall coverage of the domain.

corresponding density area in the middle, dividing the domain in two areas containing the same mass. In Experiment 6, several robots are equipped with multiple sensing capabilities. In this case, both algorithms successfully place the robots with shared sensors in between

the regions of high density, while the robots equipped with only one sensor occupy more dedicated positions with respect to their densities.

In general, defining the regions of dominance considering only those neighbors equipped with common sensors constitutes a major advantage of the proposed algorithm. Under this consideration, a robot can overcome locations populated by robots with which it does not share coverage responsibilities and reach areas with higher values of the density functions associated with its sensors, where it will coordinate with the corresponding robots in the team.

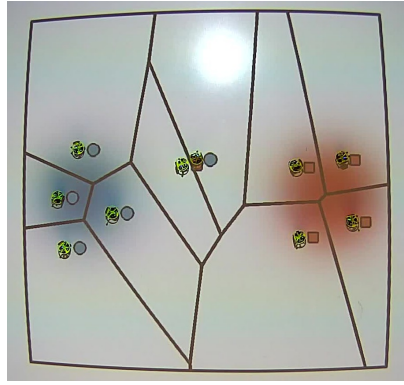
3.5 Conclusions

This chapter introduced a coverage control framework for multi-robot teams equipped with heterogeneous sensing capabilities, where a team of robots is tasked to monitor qualitatively different events in a domain. To this end, we consider a scenario where not all the robots in the team are equipped with all the sensors required to survey the domain events, but rather with a subset of them. Furthermore, the relative importance of the different features within the domain may vary. As a result, we no longer have a common density function that represents the importance of the points in the domain for all the robots, but rather a family of density functions associated with the different events.

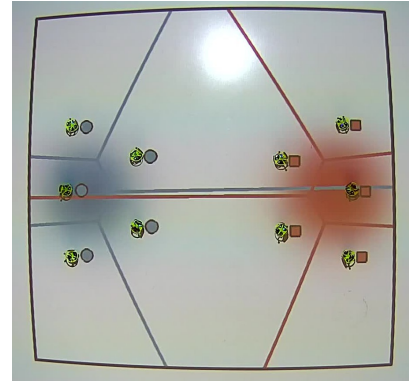
In order to encode the coverage performance of the multi-robot team, two different locational costs were proposed in this chapter. First, we considered a scenario where the robots are unaware of the sensor suites of their neighbors and, thus, compute their individual density functions by composing the densities associated with their sensor suites. Under this consideration, a locational cost balancing the coordination of the agents and the individual objectives with respect to each robot's density functions was introduced. Alternatively, we envisioned a situation where the robots had information about the sensor modalities of their neighbors. With this information flow, the regions of dominance of a robot were defined independently for each of its sensors as a function of its neighbors sensor equipments and we

presented a new locational cost that evaluates the performance of the team when covering the different density functions over such regions of dominance.

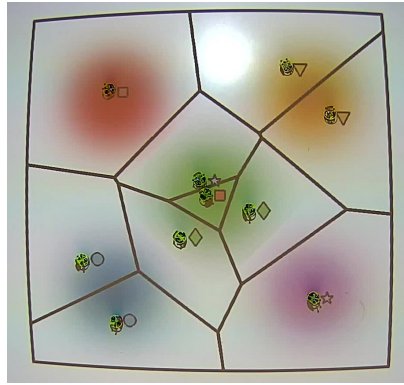
Gradient descent control laws that allow the multi-robot system to achieve a critical point of each of the costs were derived and their performance evaluated through a series of experiments on a team of differential-drive robots. The gradient descent flow on the communication-free scheme was evaluated against a heterogeneous version of Lloyd’s algorithm. In this case, the experiments suggested that the additional terms obtained due to the heterogeneous nature of the performance metric resulted in overall better coverage than a heterogeneous version of Lloyd’s algorithm for a number of different density configurations. Furthermore, we conducted a series of experiments to illustrate the influence of different regularizer values to balance the coordination between agents and their individual interests. The two gradient descent strategies—with and without communications about sensor suites—were compared through a series of experiments to highlight the importance of communications in the second approach. The experiments suggest that incorporating communications among the team members indeed improves the quality of coverage on the heterogeneous sensing capabilities scenario, as the proposed algorithm achieved better values of the performance metric for a number of different density and sensor configurations.



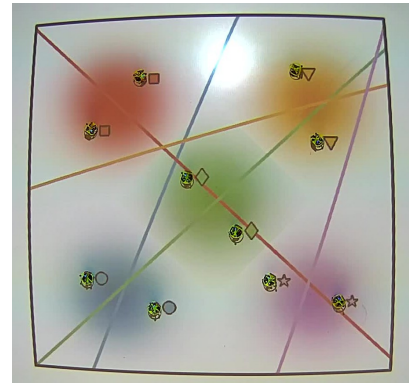
(a) Without communications, Exp. 2.



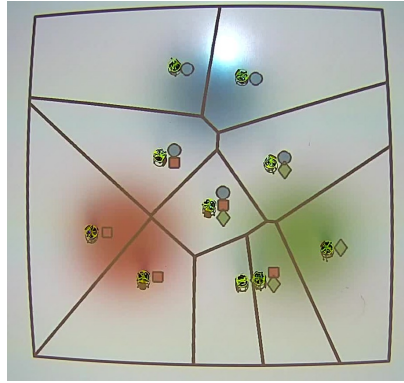
(b) With communications, Exp. 2.



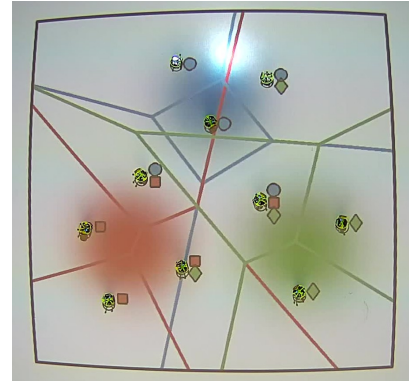
(c) Without communications, Exp. 4.



(d) With communications, Exp. 4.



(e) Without communications, Exp. 6.



(f) With communications, Exp. 6.

Figure 3.6: Final configurations of the multi-agent team for Experiments 2, 4 and 6. Figures (a), (c) and (e) correspond to the coverage control algorithm in Theorem 3.2, while Figs. (b), (d) and (f) illustrate the final spatial allocation of the team when running the algorithm in Theorem 3.3, which includes communications, for the same sensor configurations and initial conditions. The parts of the domain shaded with the different colors represent the areas of highest density, with each color identifying a different sensing modality. Each robot has a collection of symbols located to its right, which represents its sensor equipment and is color coded according to the associated density functions. With respect to the specifications in Table 3.4, the colors—blue, red, green, orange, and purple—correspond to the numerical identifiers 1 to 5 in the sensor equipments.

CHAPTER 4

COVERAGE CONTROL WITH TIME-VARYING DENSITY FUNCTIONS

Coverage control deals with the problem of distributing a collection of mobile robots in an environment such that the surveillance of its features/events is optimized [6, 7, 44]. The coverage performance of a team of robots over a domain \mathcal{D} is typically quantified with respect to a density function, $\phi : q \in \mathcal{D} \mapsto \phi(q) \in [0, \infty)$, that encodes the relative importance of the points in such a domain. While many aspects of the coverage problem have been considered in the literature, e.g. limitations on the robots' motion [21, 64], geometric variations on the sensors' footprints [20, 65], or different sensing capabilities [184, 185]; oftentimes the density functions ϕ considered are static and do not depend on time.

However, in some coverage applications, the importance of the points in the domain may evolve over time due to, for example, the tracking of moving targets [29, 82] or new area objectives specified by a human operator [8, 83]. In these cases, it may be advantageous to preserve most of the structure of the coverage problem in [6] and reflect the dynamic nature of these goals by considering the density function to be time-varying, $\phi : (q, t) \in \mathcal{D} \times \mathbb{R}_+ \mapsto \phi(q, t) \in \mathbb{R}_+$. Introducing this time dependence, however, has implications on how to design distributed control laws that allow the robots to effectively cover the density function. Past approaches to this problem rely on limitations on the rate of change of the density functions [29, 84], lack formal guarantees on the stability of the robots' input [82] or introduce approximations [83] to produce a distributed controller that optimizes the coverage performance over time.

In this chapter, we propose a constraint-based approach to the time-varying coverage problem that can be executed in an exact, decentralized fashion without imposing any conditions on the rate of change of the density functions [192]. In addition, this constraint-

based strategy naturally lends itself composable with additional behaviors that could be concurrently executed by the multi-robot team, e.g. energy saving, collision avoidance [86].

This chapter is organized as follows: In Section 4.1, we recall the formulation of the problem of multi-robot coverage (see Section 2.1 for a detailed explanation) and discuss some of the existing strategies for time-varying coverage control. Section 4.2 introduces the technical details of the constraint-based task execution framework. Using these results, the proposed strategy for time-varying coverage control is presented in Section 4.3. This algorithm is implemented on a real robotic platform and its performance is compared to other approaches in Section 4.4. The equations needed for implementing the constraint-based approach for time-varying coverage control in the heterogeneous scenario from Chapter 3 are included in Section 4.5. The conclusions of this chapter are presented in Section 4.6.

4.1 Time-Varying Density Functions

4.1.1 Homogeneous Coverage of Static Density Functions

The coverage control problem formulation in this thesis considers a team of N robots, whose positions are denoted by $p_i \in \mathbb{R}^d$, $i \in \{1, \dots, N\} := \mathcal{N}$, where $d = 2$ for planar robots and $d = 3$ in the case of aerial robots. The objective of the coverage control problem is to distribute this team of mobile robots in a domain $\mathcal{D} \subset \mathbb{R}^d$ with respect to a density function that encodes the relative importance of the points in \mathcal{D} , $\phi : \mathcal{D} \rightarrow [0, \infty)$. As shown in Section 2.1, one natural choice is to make Robot i , $i \in \mathcal{N}$, be in charge of covering the points that are closest to it,

$$V_i(p) = \{q \in \mathcal{D} \mid \|q - p_i\| \leq \|q - p_j\|, \forall j \in \mathcal{N}\},$$

that is, its Voronoi cell. The quality of coverage of the multi-robot team can then be encoded through the cost in [6],

$$\mathcal{H}(p) = \sum_{i=1}^N \int_{V_i(p)} \|p_i - q\|^2 \phi(q) dq, \quad (4.1)$$

with a lower value of the cost corresponding to a better coverage. Let

$$c_i(p) = \frac{\int_{V_i(p)} q \phi(q) dq}{\int_{V_i(p)} \phi(q) dq}$$

be the center of mass of the Voronoi cell of Robot i . A necessary condition for (4.1) to be minimized is that the position of each robot corresponds to the center of mass of its Voronoi cell [45], that is, the robots are in a *centroidal Voronoi tessellation* (CVT).

In order to approach the centroidal Voronoi tessellation, we can make the robots follow a direction of descent of the type

$$p^{(k+1)} = p^{(k)} - \alpha_k \frac{\partial J}{\partial p}(p^{(k)}),$$

where the superscript k denotes the time-step and $J(p)$ is a function whose stationary points are the centroidal Voronoi tessellations [45]. A natural choice for J is

$$J(p) = \sum_{i=1}^N \frac{1}{2} \|p_i - c_i(p)\|^2 = \sum_{i=1}^n J_i(p). \quad (4.2)$$

Taking the derivative of J_i with respect to p_i , one obtains,

$$\frac{\partial J_i}{\partial p_i} = (p_i - c_i(p))^T \left(I - \frac{\partial c_i(p)}{\partial p_i} \right), \quad (4.3)$$

where I is the identity matrix. Note that, even if $c_i(p)$ depends on the entire ensemble state of the robotic swarm, p , Robot i only requires information about its Delaunay neighbors to

compute it. Thus, the gradient in (4.3) can be calculated in a decentralized fashion.

4.1.2 Time-Varying Densities

The formulation of the coverage control problem in (4.1) considers a static density function, $\phi(q)$, over the domain of interest, that is, the relative importance of the points does not change over time. In situations where the importance of the points in the domain may vary with time, however, the density function of the domain is time-variant. Considering a time-varying density function $\phi : (q, t) \in \mathcal{D} \times \mathbb{R}_+ \mapsto \phi(q, t) \in \mathbb{R}_+$, results in the following locational cost,

$$\mathcal{H}(p, t) = \sum_{i=1}^N \int_{V_i(p)} \|q - p_i\|^2 \phi(q, t) dq. \quad (4.4)$$

Section 2.1.2 of this thesis includes a detailed summary of control laws for multi-robot teams to minimize the cost in (4.4), along with their limitations. In particular, recalling the approach in [3, 83], considering the time-varying version of the cost in (4.2),

$$J(p, t) = \sum_{i=1}^N \frac{1}{2} \|p_i - c_i(p, t)\|^2 = \sum_{i=1}^n J_i(p, t), \quad (4.5)$$

one can achieve a CVT, without imposing conditions on the variation of $\phi(q, t)$, by setting

$$u = \left(I - \frac{\partial c}{\partial p} \right)^{-1} \left(\kappa(c(p, t) - p) + \frac{\partial c}{\partial t} \right), \quad (4.6)$$

where $u = [u_1^T, \dots, u_N^T]^T$ and $c = [c_1^T, \dots, c_N^T]^T$.

However, inverting the matrix $I - \frac{\partial c}{\partial p}$ in (4.6) cannot be done in a decentralized fashion. For this reason, in [83], the inverse is approximated by a truncated Neumann series as

$$\left(I - \frac{\partial c}{\partial p} \right)^{-1} \approx I + \frac{\partial c}{\partial p} \quad (4.7)$$

which allows each robot to evaluate its corresponding term based solely on information about its Delaunay neighbors. This chapter presents a decentralized solution to the time-

varying coverage control problem which does not require us to make any such approximations. Next, we introduce some of the tools necessary to develop such an algorithm.

4.2 Constraint-Based Task Execution

This chapter uses the constraint-based task execution framework introduced in [86] to perform coverage control in the presence of time-varying density functions. Consequently, this section introduces some of the tools required to develop the proposed algorithm which will be presented in Section 4.3.

The execution of a task by a robot can be encoded using the following pointwise minimum-energy constrained optimization problem,

$$\min_u \|u\|^2 \quad \text{s.t.} \quad c_{task}(x, u) \geq 0,$$

where u is the control effort expended by the robot, x is its state, and c_{task} symbolizes a constraint function which ensures the execution of the task. Such a constraint-based formulation is advantageous in terms of its suitability for long-term autonomy applications as well as composability with other tasks that need to be performed [23, 193, 194, 195]. The initial formulation in this section considers constraints that do not explicitly depend on time. Later in the section, the time-varying formulation is presented.

The feasibility of this task execution framework is ensured by the introduction of slack variables in the constraint,

$$\begin{aligned} \min_{u, \delta} \|u\|^2 + |\delta|^2 \\ \text{s.t.} \quad c_{task}(x, u) \geq -\delta, \end{aligned} \tag{4.8}$$

where δ is the slack variable and signifies the extent to which the task constraint can be violated. An effective way of enforcing such constraints in a multi-robot system is to use control barrier functions, which are introduced next.

4.2.1 Control Barrier Functions

Consider a dynamical system in control affine form,

$$\dot{x} = f(x) + g(x)u,$$

where $x \in \mathbb{R}^n$, $u \in U \subseteq \mathbb{R}^m$, with f and g being Lipschitz continuous vector fields.

Consider a continuously differentiable function $h : \mathbb{R}^n \rightarrow \mathbb{R}$, and define the *safe set* S as its zero-superlevel set,

$$S = \{x \in \mathbb{R}^n \mid h(x) \geq 0\}. \quad (4.9)$$

The function h is called a (*zeroing*) *control barrier function (CBF)* if the following condition is satisfied,

$$\sup_{u \in U} \{L_f h(x) + L_g h(x)u + \alpha(h(x))\} \geq 0 \quad \forall x \in \mathbb{R}^n, \quad (4.10)$$

where α is a locally Lipschitz extended class \mathcal{K} function [196], and $L_f h(x)$ and $L_g h(x)$ denote the Lie derivatives of h in the directions f and g , respectively. The following theorem from [196, 86] summarizes two important properties of zeroing CBFs.

Theorem 4.1. *Given a dynamical system in control affine form $\dot{x} = f(x) + g(x)u$, where $x \in \mathbb{R}^n$ and $u \in \mathbb{R}^m$ denote the state and the input, respectively, f and g are locally Lipschitz, and a set $S \subset \mathbb{R}^n$ defined by a continuously differentiable function h as in (4.9), any Lipschitz continuous controller u such that (4.10) holds renders the set S forward invariant and asymptotically stable, i. e.,*

$$x(0) \in S \Rightarrow x(t) \in S \quad \forall t \geq 0$$

$$x(0) \notin S \Rightarrow x(t) \rightarrow \in S \text{ as } t \rightarrow \infty,$$

where $x(0)$ denotes the state x at time $t = 0$ and the notation $x(t) \rightarrow \in S$ indicates that

$x(t)$ asymptotically approaches the set S .

Proof. See [86] and [196]. □

In this chapter, we encode the execution of the time-varying coverage control task via a zeroing CBF-based constraint for each robot. Consequently, the zeroing CBFs themselves explicitly depend on time. To this end, the definition of zeroing CBFs given in [196] is extended for the time-varying case.

Definition 4.2 (Time-Varying CBFs [197]). *Given a function $h : \mathbb{R}^n \times \mathbb{R}_+ \mapsto \mathbb{R}$, continuously differentiable in both its arguments, consider a dynamical system in control affine form $\dot{x} = f(x) + g(x)u$, where $x \in \mathbb{R}^n$ and $u \in \mathbb{R}^m$ denote system state and input, respectively, f and g are locally Lipschitz, and the set $S = \{x \in \mathbb{R}^n \mid h(x, t) \geq 0\}$. The function h is a time-varying zeroing CBF defined on $\mathbb{R}^n \times \mathbb{R}_+$, if there exists a locally Lipschitz extended class \mathcal{K} function α such that, $\forall x \in \mathbb{R}^n, \forall t \in \mathbb{R}_+$,*

$$\sup_{u \in U} \left\{ \frac{\partial h}{\partial t} + L_f h(x, t) + L_g h(x, t) u + \alpha(h(x, t)) \right\} \geq 0. \quad (4.11)$$

We now demonstrate how CBFs can be incorporated into the constrained optimization problem (4.8) to accomplish the execution of robot tasks.

4.2.2 Minimum-Energy Gradient Descent

The execution of tasks which involve the minimization of a cost function J —such as the coverage control task investigated in this thesis—can be achieved by generating a control signal $u(t)$ using the optimization problem

$$\min_u J(x), \quad (4.12)$$

where x and u are coupled through the single integrator dynamics $\dot{x} = u$. In [86], we show that solving (4.12) in order to synthesize $u(t)$ is equivalent to solving the follow-

ing constraint-based optimization problem, in the sense that they both achieve the goal of minimizing the cost J ,

$$\begin{aligned} \min_{u, \delta} \quad & \|u\|^2 + |\delta|^2 \\ \text{s.t.} \quad & \frac{\partial h}{\partial x} u \geq -\alpha(h(x)) - \delta \end{aligned} \tag{4.13}$$

where $\delta \in \mathbb{R}$ is the slack variable signifying the extent to which the task constraint can be violated, α is an extended class \mathcal{K} function, and $h(x) = -J(x)$ is a zeroing CBF. The zero-superlevel set of h is $S = \{x \mid h(x) \geq 0\} = \{x \mid J(x) \leq 0\} = \{x \mid J(x) = 0\}$, where the last equality holds because the cost $J(x)$ is a non-negative function.

The following proposition, proved in [86], establishes how the constraint-based optimization problem given in (4.13), allows the accomplishment of the task encoded by $J(x)$.

Proposition 4.3. *The solution of the optimization problem (4.13), where $h(x) = -J(x)$ and α is an extended class \mathcal{K} function, solves (4.12), driving the state x of the dynamical system $\dot{x} = u$ to a stationary point of the cost J .*

In fact, for the special case when J is strictly convex and $J(0) = 0$, we have that

$$\frac{\partial J}{\partial x}(x) \neq 0, \quad \forall x \neq 0.$$

Consequently, using Theorem 4.1 we get $x \rightarrow \in S$, i. e. $J(x(t)) \rightarrow 0$, as $t \rightarrow \infty$.

Using the above described formulation, this chapter encodes the problem of covering a time-varying density function as a constraint-based optimization problem in Section 4.3. But first, we discuss the conditions under which the optimization problem in (4.13) can be solved in a decentralized fashion.

4.2.3 Decentralized Constraint-Based Control of Multi-Robot Systems

Assume that each robot in the multi-robot team is able to measure the relative positions of a subset of the robot team as described by an undirected graph $\mathcal{G} = (\mathcal{V}, \mathcal{E})$, where $\mathcal{V} = \{1, \dots, N\}$ is the set of vertices of the graph, representing the robots, and $\mathcal{E} \subseteq \mathcal{V} \times \mathcal{V}$

is the set of edges between the robots, encoding adjacency relationships. For example, the adjacency relationships for the multi-robot coverage control task investigated in this chapter is described by a Delaunay graph [6].

Let $p = [p_1^T, \dots, p_N^T]^T \in \mathbb{R}^{Nd}$ denote the ensemble state of the multi-robot team. As the robots are solving a time-varying coverage control problem, we consider a time-varying total cost $J(p, t)$. Then, a general expression for this cost that leads to decentralized control laws [3] is given by

$$J(p, t) = \sum_{i=1}^N \sum_{j \in \mathcal{N}_i} J_{ij}(\|p_i - p_j\|, t), \quad (4.14)$$

where \mathcal{N}_i is the neighborhood set of Robot i , and $J_{ij} : \mathbb{R}_+ \times \mathbb{R}_+ \rightarrow \mathbb{R}_+$, $J_{ij}(\|p_i - p_j\|, t) = J_{ji}(\|p_j - p_i\|, t)$ is a symmetric, pairwise cost between robots i and j . We assume that $J_{ij}(p, t) \geq 0$, $\forall (i, j) \in \mathcal{E}$, $\forall p \in \mathbb{R}^n, t \in \mathbb{R}_+$, so that $J(p, t) \geq 0$, $\forall p \in \mathbb{R}^n, t \in \mathbb{R}_+$. It should be noted that (4.5) can be written in the form of (4.14) as a consequence to the graph topology induced by the Voronoi partition.

The following proposition outlines the optimization problems whose solutions lead to a decentralized minimization of the cost $J(p, t)$ in (4.14).

Proposition 4.4 (Constraint-driven decentralized time-varying task execution). *Given the time-varying pairwise cost function J defined in (4.14), a collection of N robots, obeying single integrator dynamics, minimizes J in a decentralized fashion, if each robot executes the control input, solution of the following optimization problem:*

$$\begin{aligned} \min_{u_i, \delta_i} & \|u_i\|^2 + |\delta_i|^2 \\ \text{s.t.} & -\frac{\partial J_i}{\partial p_i} u_i \geq -\alpha(-J_i(p)) + \frac{\partial J_i}{\partial t} - \delta_i, \end{aligned} \quad (4.15)$$

where $J_i(p, t) = \sum_{j \in \mathcal{N}_i} J_{ij}(\|p_i - p_j\|, t)$ and α is an extended class \mathcal{K} function, $\alpha : p \in \mathbb{R} \mapsto \alpha(p) \in \mathbb{R}$, superadditive for $p < 0$, i.e. $\alpha(p_1 + p_2) \geq \alpha(p_1) + \alpha(p_2)$, $\forall p_1, p_2 < 0$.

Proof. Using (4.11) from Definition 4.2, the proof follows similar to [86]. \square

We are now ready to present a novel approach for executing decentralized approximation-free coverage control under time-varying density functions using a team of robots.

4.3 An Exact and Decentralized Approach to Time-Varying Coverage

As described in Section 4.1, effective coverage of a domain can be achieved by driving the robots to the stationary points of the time-varying cost functional $J(p, t)$ given in (4.5), which correspond to the CVT. To this end, we allow each Robot i to solve the optimization problem presented in (4.15). Plugging in expressions for the partial derivatives of $J_i(p, t)$ as pertaining to the time-varying coverage control problem, (4.15) yields,

$$\begin{aligned} \min_{u_i, \delta_i} & \|u_i\|^2 + |\delta_i|^2 \\ \text{s.t.} & - (p_i - c_i(p, t))^T \left(I - \frac{\partial c_i(p, t)}{\partial p_i} \right) u_i \\ & \geq -\alpha(-J_i(p, t)) - (p_i - c_i(p, t))^T \frac{\partial c_i(p, t)}{\partial t} - \delta_i, \end{aligned} \quad (4.16)$$

which is both exact and decentralized. The form of the partial derivatives of $c_i(p, t)$ can be found in [198],

$$\begin{aligned} \frac{\partial c_i(p, t)}{\partial p_i} &= \sum_{j \in \mathcal{N}_i} \frac{\int_{\partial V_{ij}(p)} (q - c_i(p, t)) \phi(q, t) (q - p_i)^T dq}{m_i(p, t) \|p_j - p_i\|}, \\ \frac{\partial c_i(p, t)}{\partial t} &= \frac{\int_{V_i(p)} (q - c_i(p)) \frac{\partial \phi(q, t)}{\partial t} dq}{m_i(p, t)}, \end{aligned}$$

with $m_i(p, t) = \int_{V_i} \phi(q, t) dq$ the mass in the Voronoi cell of Robot i .

Proposition 4.5. *Consider a team of N single-integrator robots, tasked with covering a region as specified by a time-varying density function. Under u^* , solution of (4.16), where α is a superlinear extended class \mathcal{K} function, the robots achieve a CVT.*

Proof. From Proposition 4.4, we know that executing u^* will drive the robots towards a stationary point of the cost function J . As discussed in Section 5.4 of [45], any search

algorithm that attains the stationary points of the cost J , achieves a CVT configuration. \square

We further demonstrate that, under the assumption that the robots do not have actuator limitations, the optimization problem presented in (4.16) can be reformulated to exclude slack variables in the optimization problem.

Proposition 4.6. *Consider a team of N single-integrator robots with no actuator constraints, i.e., $U = \mathbb{R}^m$, tasked with covering a region as specified by a time-varying importance density function. Let each robot solve the following problem:*

$$\begin{aligned} \min_{u_i} & \|u_i\|^2 \\ \text{s.t.} & -(p_i - c_i(p, t))^T \left(I - \frac{\partial c_i(p, t)}{\partial p_i} \right) u_i \\ & \geq -\alpha(-J_i(p, t)) - (p_i - c_i(p, t))^T \frac{\partial c_i(p, t)}{\partial t}. \end{aligned} \quad (4.17)$$

Under the control action generated by this optimization problem, the robots achieve a centroidal Voronoi tessellation (CVT).

Proof. The total time derivative of the time-varying coverage cost function $J(p, t)$ given in (4.5) can be expressed as,

$$\begin{aligned} \dot{J} &= \sum_{i=1}^N \dot{J}_i(p) = \sum_{i=1}^N \left(\frac{\partial J_i}{\partial p_i} u_i + \frac{\partial J_i}{\partial t} \right) \\ &= \sum_{i=1}^N (p_i - c_i(p, t))^T \left(I - \frac{\partial c_i(p, t)}{\partial p_i} \right) u_i - \sum_{i=1}^N (p_i - c_i(p, t))^T \frac{\partial c_i(p, t)}{\partial t}. \end{aligned}$$

Consequently, given the superadditivity property of α and summing over the constraints corresponding to each Robot $i \in \mathcal{N}$ in the optimization problem (4.17), we get,

$$\dot{J}(p, t) \leq \alpha(-J(p, t))$$

Let $\bar{\alpha}(r) = -\alpha(-r)$. Then, by the properties of extended class \mathcal{K} functions, $\bar{\alpha}$ is also an

extended class \mathcal{K} function. Thus,

$$\dot{J}(p, t) \leq -\bar{\alpha}(J(p, t)),$$

and thus, by applying the comparison lemma [199], one can observe that:

$$J(t) \leq \beta(J(p_0, 0), t),$$

with β a class \mathcal{KL} function and p_0 the configuration of the robots at time $t = 0$. Therefore, $J(p, t) \rightarrow 0$ as $t \rightarrow \infty$, that is, the system converges to a CVT since $J(p, t) = 0 \Leftrightarrow p_i(t) = c_i(p, t), \forall i \in \mathcal{N}$. \square

4.4 Simulations and Experimental Results

The performance of the proposed constraint-based approach is evaluated in simulation as well as on a team of differential drive robots on the Robotarium [191], a remotely accessible multi-robot testbed at the Georgia Institute of Technology. The experiment, uploaded via web, is remotely executed on the Robotarium and the data is made available to the user once the experiment is finalized. On each control iteration, the Robotarium provides the poses of the robots involved in the experiment and allows the user to specify the linear and angular velocities of each robot in the team.

The proposed constraint-based controller in (4.16) is compared in simulation with the standard Lloyd's algorithm [43], whereby $\dot{p}_i = \kappa(c_i(p) - p_i), \kappa > 0, \forall i \in \mathcal{N}$; and with the centralized strategy in (4.6) from Lee *et al.* [83] and its decentralized variant, which uses the Neumann approximation in (4.7). In order to minimize the influence of the proportional gain, the simulation parameter $\kappa = 1$ was chosen for all three controllers. In the case of the proposed controller, the extended class \mathcal{K} function was $\alpha(p) = p^{\frac{1}{3}}$. The simulations are implemented on the Robotarium simulator with the objective of providing a realistic frame-

work that considers robot dynamics and actuator bounds, thus providing a fair comparison between the different algorithms.

As presented in Sections 4.1 and 4.3, the considered coverage control algorithms assume that the robots move according to single integrator dynamics. However, the robots considered in this section have a differential drive kinematic configuration, whose movement is best described by the so-called unicycle dynamics,

$$\dot{p}_i = [v_i \cos \theta_i, v_i \sin \theta_i]^T, \quad \dot{\theta}_i = \omega_i,$$

where θ_i is the orientation of the robot. The control inputs v_i and ω_i are the linear and angular velocities, which can be calculated using the near-identity diffeomorphism in [200].

We consider the following time-varying density function to be covered by a team of 6 differential drive robots over a time interval of 60 seconds,

$$\begin{aligned} \phi_{exp}(q, t) = & 1 + 10^3 \frac{1 - \sin(2\pi 10^{-3}t)}{2} \exp\left(-\frac{(q_x + 0.2)^2 - (q_y + 0.1)^2}{0.4}\right) \\ & + 10^3 \frac{1 - \sin(2\pi 10^{-3}t - \frac{\pi}{2})}{4} \exp\left(-\frac{(q_x - 0.6)^2 - (q_y - 0.2)^2}{0.1}\right). \end{aligned} \quad (4.18)$$

In order to compare the performance of the different algorithms, one can compute the integral of the cost $J(p, t)$ over time [83], as a metric of how well the density function is being tracked by the robot team,

$$\int_0^t J(p(\tau), \tau) d\tau.$$

As it can be observed in Fig. 4.1, considering the effects of the time-varying density makes our approach and the controllers in [83] outperform Lloyd's algorithm, which was designed for the time-invariant case. However, while producing similar coverage of the density function, some algorithms may require higher control efforts from the robots than others. Therefore, we use the following metric to measure the amount of energy used by

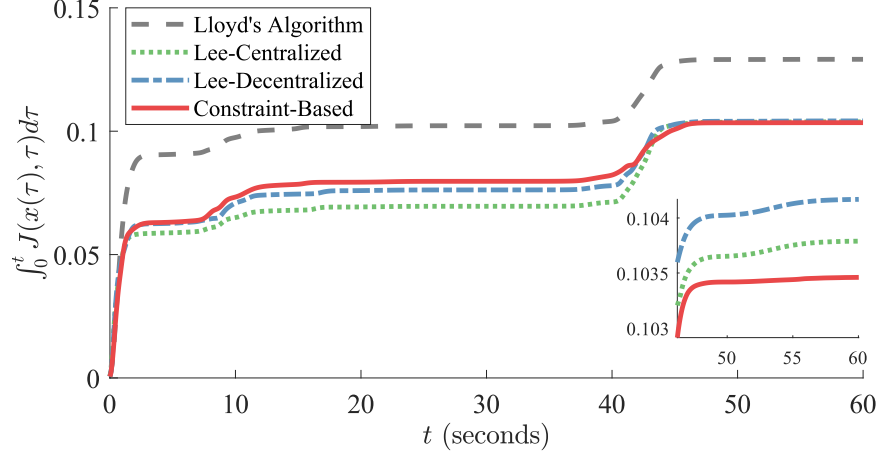


Figure 4.1: Evolution of the integral of the cost, $J(p, t)$, over time for the proposed constraint-based approach, Lloyd's algorithm [43] as well as the centralized and decentralized controllers in Lee *et al.* [83]. The final value of the cumulative cost for the proposed algorithm is very similar (although slightly lower) to the controllers that consider the effects of the time-varying densities by Lee *et al.* Ignoring the effects of a time-varying density function causes an appreciable difference in the case of Lloyd's algorithm. Inset highlights differences in costs towards the end of the experiment.

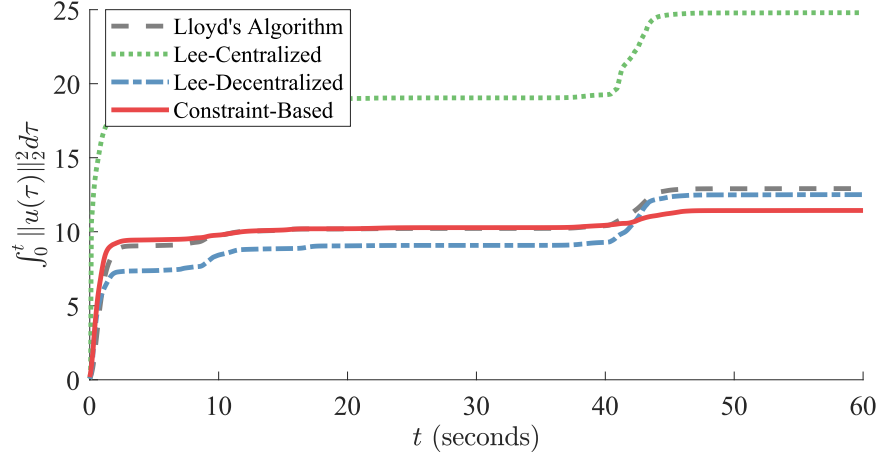


Figure 4.2: Comparison of the cumulative control effort for the proposed constraint-based approach, Lloyd's algorithm [43] as well as the centralized and decentralized controllers in [83]. While the performance of the algorithms in Lee *et al.* are similar to the proposed approach in terms of the final cost (see Fig. 4.1), the control effort required for the team to track the density functions is higher.

the robot team to cover the density function,

$$\int_0^t \|u(\tau)\|_2^2 d\tau.$$

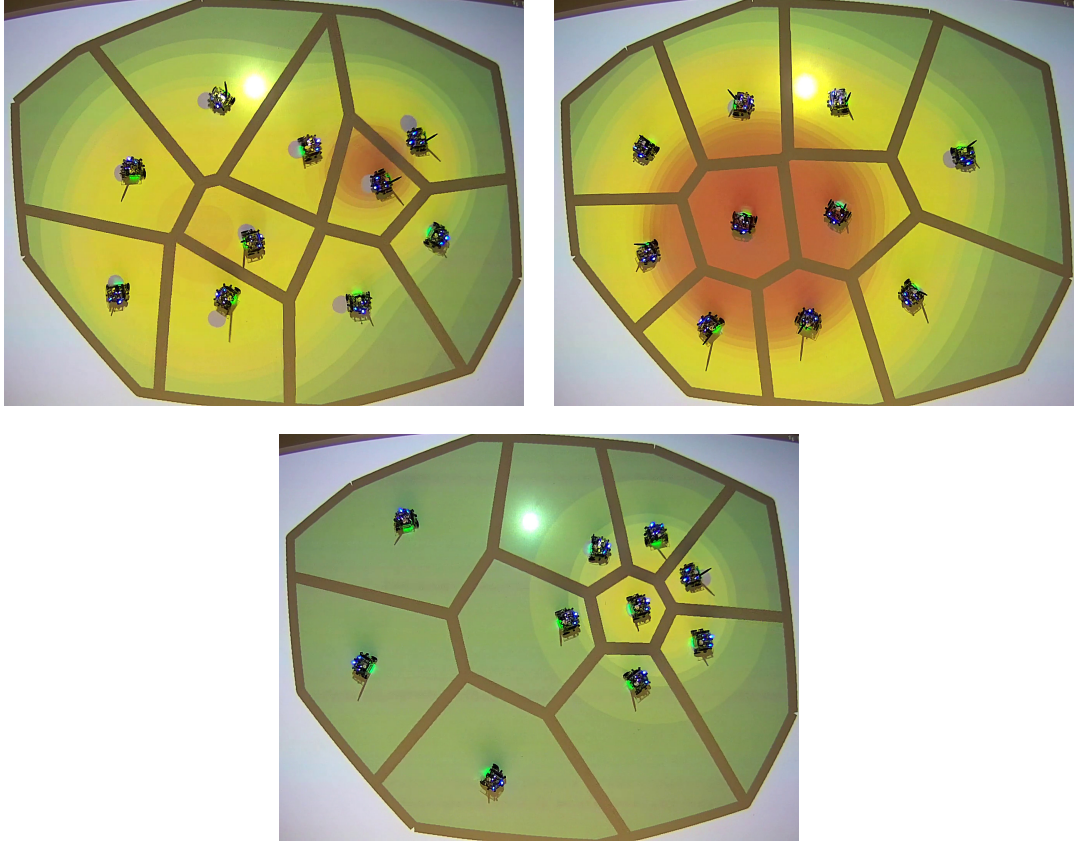


Figure 4.3: Snapshots from the time-varying coverage control experiment deployed on a multi-robot team operating on the Robotarium [191]. The time-varying density function is depicted by projecting its contour plot onto the testbed. As seen, using the constraint-based coverage algorithm, the robots track the centroids of their Voronoi cells, depicted as gray circles.

Figure 4.2 shows the control effort expended by the robots when executing the different algorithms considered. While the approaches from [83] produced similar cumulative costs in Fig. 4.1, we can observe that the control effort demanded by these controllers is higher than that of the proposed strategy in this chapter.

Figure 4.3 shows a series of snapshots of an experiment executed on the Robotarium. Ten GRITSBots were deployed to cover the density function in (4.18) for a total duration of 2 minutes. We can observe how the robots effectively track the centroids of their Voronoi cells as the density function changes over time. The evolution of the cost, $J(p, t)$, for this experiment is shown in Fig. 4.4, where the cost is kept close to zero. The temporary

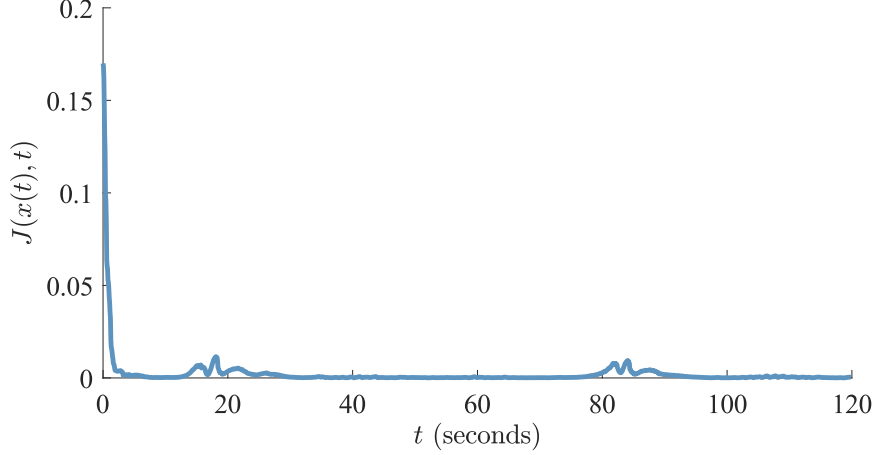


Figure 4.4: Evolution of the cost $J(p, t)$ for the proposed minimum energy coverage algorithm. The constraint-based approach drives the robots in a direction which reduces the overall coverage cost considered in (4.5) to zero. The temporary increases in the cost can be attributed to the fact that the robots have actuator constraints and thus cannot track arbitrarily high velocities generated by the optimization program. As the robots reduce the distance from the moving centroids of their Voronoi cells, the cost goes back towards zero.

increases in the cost around $t = 19\text{s}$ and $t = 85\text{s}$ are due to the actuator constraints of the robots, which limit their ability to maintain a CVT during rapid changes of the density function.

4.5 Time-Varying Coverage With Heterogeneous Sensing Capabilities

The constraint-based approach presented in this chapter was developed to accommodate a time-varying density function, $\phi : (q, t) \in \mathcal{D} \times \mathbb{R}_+ \mapsto \phi(q, t) \in \mathbb{R}_+$, into the homogeneous version of the coverage control problem. Due to its generality, however, this approach can be extended to the heterogeneous coverage scenario presented in Chapter 3, which considers a set of sensory modalities, \mathcal{S} , associated with a class of static density functions $\phi_j : \mathcal{D} \mapsto [0, \infty)$, $j \in \mathcal{S}$, with $\phi_j(q)$ representing the importance of a point $q \in \mathcal{D}$ according to sensor $j \in \mathcal{S}$. This section outlines the equations needed to execute both heterogeneous coverage approaches (see Sections 3.2 and 3.3 of this thesis for details) when these sensor-dependent densities are time-varying, i.e. when $\phi_j : (q, t) \in \mathcal{D} \times \mathbb{R}_+ \mapsto \phi_j(q, t) \in \mathbb{R}_+$, $j \in \mathcal{S}$.

4.5.1 Time-Varying Heterogeneous Coverage

The heterogeneous coverage control approach for qualitatively different sensing capabilities presented in Section 3.2 encodes the performance of the multi-robot team, equipped with sensory capabilities \mathcal{S} according to the family of density functions $\phi_j(q, t), j \in \mathcal{S}$, as the locational cost in (3.4),

$$\mathcal{H}_{het}(p, t) = \sigma \sum_{i \in \mathcal{N}} \int_{V_i(p)} \|q - p_i\|^2 \phi_{s(i)}(q, t) dq + (1 - \sigma) \sum_{i \in \mathcal{N}} \int_{\mathcal{D}} \|q - p_i\|^2 \phi_{s(i)}(q, t) dq, \quad (4.19)$$

where $\sigma \in (0, 1]$ acts as a regularizer term and $\phi_{s(i)}(q, t) = \bigoplus_{j \in s(i)} \phi_j(q, t)$ denotes the composition of the density functions associated with the subset of sensors that Robot i is equipped with, $s(i) \subset \mathcal{S}, i \in \mathcal{N}$.

According to Theorem 3.2, the following control law allows the multi-robot team to asymptotically achieve a spatial configuration that corresponds to a critical point to the locational cost (4.19),

$$u_i = -2\kappa (\sigma m_i(p_i - c_i) + (1 - \sigma) M_i(p_i - C_i)) + \sigma \kappa \sum_{j \in \mathcal{N}_i} (\mu_{ij}(p_i - \rho_{ij}) - \mu_{ji}(p_i - \rho_{ji})),$$

where $m_i(p, t)$ and $c_i(p, t)$ denote the mass and center of mass of the Voronoi cell $V_i(p)$, as defined in (3.8),

$$m_i(p, t) = \int_{V_i(p)} \phi_{s(i)}(q, t) dq, \quad c_i(p, t) = \frac{\int_{V_i(p)} q \phi_{s(i)}(q, t) dq}{m_i}; \quad (4.20)$$

$M_i(t)$ and $C_i(t)$ are the mass and center of mass over the whole domain, \mathcal{D} , as in (3.12),

$$M_i(t) = \int_{\mathcal{D}} \phi_{s(i)}(q, t) dq, \quad C_i(t) = \frac{\int_{\mathcal{D}} q \phi_{s(i)}(q, t) dq}{M_i};$$

and $\mu_{ij}(p, t)$ and $\rho_{ij}(p, t)$ represent the weighted mass and center of mass along the bound-

ary between Robot i and its neighbor j , $\partial V_{ij}(p)$, as in (3.10),

$$\mu_{ij}(p, t) = \int_{\partial V_{ij}(p)} \frac{\|q - p_i\|^2}{\|p_j - p_i\|} \phi_{s(i)}(q, t) dq, \quad (4.21)$$

$$\rho_{ij}(p, t) = \frac{\int_{\partial V_{ij}(p)} q \frac{\|q - p_i\|^2}{\|p_j - p_i\|} \phi_{s(i)}(q, t) dq}{\mu_{ij}}. \quad (4.22)$$

In Section 4.1.2, the cost $J(p, t)$ was defined in terms of the minimizer of the cost $\mathcal{H}(p, t)$. Analogously, for the heterogeneous case, one can define a cost $J_{het}(p, t)$ whose minimizer is also the minimizer of (4.19),

$$J_{het}(p, t) = \sum_{i=1}^N \frac{1}{2k^2} \|u_i\|^2 = \sum_{i=1}^n J_{het,i}(p, t).$$

In order to drive the robots to a stationary point of the time-varying cost, as in the homogeneous case, we let the robots solve the optimization problem in (4.15), this time with respect to J_{het} . To this end, we need the expressions for the partial derivatives of $J_{het,i}(p, t)$, $\partial J_{het,i}/\partial p_i$ and $\partial J_{het,i}/\partial t$. The remainder of this section presents the analytical form of this partial derivatives.

Computation of $\partial J_{het,i}/\partial p_i$

The derivative of $J_{het,i}(p, t)$ with respect to p_i takes the following form,

$$\begin{aligned} \frac{\partial J_{het,i}(p, t)}{\partial p_i} &= \frac{1}{\kappa^2} u_i^\top \frac{\partial u_i}{\partial p_i} \\ &= \frac{1}{\kappa} u_i^\top \left[2\sigma \left((p_i - c_i) \frac{\partial m_i}{\partial p_i} + m_i \left(I - \frac{\partial c_i}{\partial p_i} \right) \right) \right. \end{aligned} \quad (4.23)$$

$$\left. + 2(1 - \sigma) \left((p_i - c_i) \frac{\partial M_i}{\partial p_i} + M_i \left(I - \frac{\partial C_i}{\partial p_i} \right) \right) \right. \quad (4.24)$$

$$\left. - \sigma \sum_{j \in \mathcal{N}_i} \left[(p_i - \rho_{ij}) \frac{\partial \mu_{ij}}{\partial p_i} + \mu_{ij} \left(I - \frac{\partial \rho_{ij}}{\partial p_i} \right) \right. \right. \\ \left. \left. - (p_i - \rho_{ji}) \frac{\partial \mu_{ji}}{\partial p_i} + \mu_{ij} \left(I - \frac{\partial \rho_{ij}}{\partial p_i} \right) \right] \right], \quad (4.25)$$

where, immediately, one can observe that $\partial M_i(t)/\partial p_i = 0$ and $\partial C_i(t)/\partial p_i = 0$ in (4.24).

The partial derivatives in (4.23) can be obtained applying Leibniz integral rule (Lemma 3.1) to the mass and center of mass in the Voronoi cell, as defined in (4.20),

$$\begin{aligned} \frac{\partial m_i(p, t)}{\partial p_i} &= \sum_{j \in \mathcal{N}_i} \int_{\partial V_{ij}(p)} \phi_{s(i)}(q, t) n_{ij}(q)^\top \frac{\partial q}{\partial p_i} dq, \\ \frac{\partial c_i(p, t)}{\partial p_i} &= \frac{1}{m_i} \sum_{j \in \mathcal{N}_i} \int_{\partial V_{ij}(p)} (q - c_i) \phi_{s(i)}(q, t) n_{ij}(q)^\top \frac{\partial q}{\partial p_i} dq, \end{aligned}$$

where $n_{ij}(q)$ denotes the outward facing normal at q . Using the equivalence from (3.6), one can rewrite these two equations as,

$$\frac{\partial m_i(p, t)}{\partial p_i} = \sum_{j \in \mathcal{N}_i} \int_{\partial V_{ij}(p)} \phi_{s(i)}(q, t) \frac{(q - p_i)^\top}{\|p_j - p_i\|} dq \quad (4.26)$$

$$\frac{\partial c_i(p, t)}{\partial p_i} = \frac{1}{m_i} \sum_{j \in \mathcal{N}_i} \int_{\partial V_{ij}(p)} (q - c_i) \phi_{s(i)}(q, t) \frac{(q - p_i)^\top}{\|p_j - p_i\|} dq \quad (4.27)$$

The computation of the partial derivatives of the mass and center of mass on the boundary in (4.25), $\partial \mu_{ij}/\partial p_i$ and $\partial \rho_{ij}/\partial p_i$, is slightly more involved since both quantities (see

(4.21) and (4.22)) are defined as line integrals in a two dimensional space, where the domain of integration depends on the configuration of the multi-robot team, $\partial V_{ij}(p)$, and, thus, on the differentiation variable, p_i . To this end, we recall the Leibniz integral rule on the real line.

Lemma 4.7 (Leibniz Integral Rule [201]). *Suppose that f and $\partial f/\partial s$ are continuous in the rectangle $R = \{(s, q) : a \leq s \leq b, c \leq q \leq d\}$ and suppose that $u_1(s)$, $u_2(s)$ are continuously differentiable for $a \leq s \leq b$ with the range of u_1 and u_2 in (c, d) . Let*

$$F(s) = \int_{u_1(s)}^{u_2(s)} f(s, q) dq,$$

then,

$$\frac{\partial F(s)}{\partial s} = f(s, u_2(s)) \frac{\partial u_2}{\partial s} - f(s, u_1(s)) \frac{\partial u_1}{\partial s} + \int_{u_1(s)}^{u_2(s)} \frac{\partial f}{\partial s}(s, q) dq. \quad (4.28)$$

In order to apply Lemma 4.7 to the computation of $\partial \mu_{ij}/\partial p_i$ and $\partial \rho_{ij}/\partial p_i$, we need to rewrite (4.21) and (4.22) in terms of the real variable, s . If we denote as $v_{ij}^1(p)$ and $v_{ij}^2(p)$ the two endpoints of $\partial V_{ij}(p)$, the parametrization of the Voronoi boundary becomes

$$\partial V_{ij}(p, s) = v_{ij}^1(p) + (v_{ij}^2(p) - v_{ij}^1(p))s, \quad s \in [0, 1]. \quad (4.29)$$

Denoting as $\|\partial V_{ij}(p)\|$ the length of the Voronoi boundary, i.e. $\|\partial V_{ij}(p)\| = \|v_{ij}^2(p) - v_{ij}^1(p)\|$, the line integrals for $\mu_{ij}(p, t)$ and $\rho_{ij}(p, t)$ can be alternatively rewritten as

$$\mu_{ij}(p, t) = \int_0^1 \frac{\|\partial V_{ij}(p, s) - p_i\|^2}{\|p_j - p_i\|} \phi_{s(i)}(\partial V_{ij}(p, s), t) \|\partial V_{ij}(p)\| ds, \quad (4.30)$$

$$\rho_{ij}(p, t) = \frac{1}{\mu_{ij}} \int_0^1 q \frac{\|\partial V_{ij}(p, s) - p_i\|^2}{\|p_j - p_i\|} \phi_{s(i)}(\partial V_{ij}(p, s), t) \|\partial V_{ij}(p)\| ds. \quad (4.31)$$

What is left to fully characterize these integrals before differentiation is to have the analytical expressions for the endpoints of the Voronoi boundary, $v_{ij}^1(p)$ and $v_{ij}^2(p)$. To this

end, the line containing the segment $\partial V_{ij}(p)$ can be parameterized as,

$$l_{ij}(p) = \frac{p_i + p_j}{2} + s_{ij} t_{ij}(p), \quad s_{ij} \in \mathbb{R}, \quad (4.32)$$

where s_{ij} is the parameter and t_{ij} is the tangent vector to ∂V_{ij} . Given that the outward facing normal to $\partial V_{ij}(p)$ is given by $n_{ij} = (p_j - p_i) / \|p_j - p_i\|$, the tangent vector can be written as

$$t_{ij} = (n_{ij,y}, -n_{ij,x})^T = \left(\frac{p_{j,y} - p_{i,y}}{\|p_j - p_i\|}, -\frac{p_{j,x} - p_{i,x}}{\|p_j - p_i\|} \right)^T.$$

In the general case where the boundary $\partial V_{ij}(p)$ is delimited by the Voronoi boundaries of Robot i with Robots k and l , i.e. $\partial V_{ik}(p)$ and $\partial V_{il}(p)$, one can calculate the endpoints $v_{ij}^1(p)$ and $v_{ij}^2(p)$ as the intersection of the corresponding lines given as in (4.32),

$$\begin{aligned} v_{ij}^1(p) &= l_{ij} \cap l_{ik} = \frac{p_i + p_j}{2} + \frac{\langle p_k - p_i, p_j - p_i \rangle \|p_j - p_i\|}{2((p_j - p_i) \times (p_k - p_i))} t_{ij}(p), \\ v_{ij}^2(p) &= l_{ij} \cap l_{il} = \frac{p_i + p_j}{2} + \frac{\langle p_l - p_i, p_j - p_i \rangle \|p_j - p_i\|}{2((p_j - p_i) \times (p_l - p_i))} t_{ij}(p), \end{aligned} \quad (4.33)$$

with $p_a \times p_b^T := p_{a,x} p_{b,y} - p_{a,y} p_{b,x}$. Note that, while we do not explicitly include in this document the expression of Voronoi boundary endpoints delimited by domain boundary instead of neighboring robots' Voronoi cells, these cases can be calculated in a similar fashion.

Having the analytical expressions for $v_{ij}^1(p)$ and $v_{ij}^2(p)$, the integrals in (4.30) and (4.31), are completely determined. We can now apply Lemma 4.7, where only the last summation term in (4.28) applies since the limits of integration no longer depend on the position of the

robots,

$$\begin{aligned}\frac{\partial \mu_{ij}(p, t)}{\partial p_i} &= \int_0^1 \frac{\partial}{\partial p_i} \left(\frac{\|\partial V_{ij}(p, s) - p_i\|^2}{\|p_j - p_i\|} \phi_{s(i)}(\partial V_{ij}(p, s), t) \|\partial V_{ij}(p)\| \right) ds, \\ \frac{\partial \rho_{ij}(p, t)}{\partial p_i} &= \frac{1}{\mu_{ij}} \int_0^1 q \frac{\partial}{\partial p_i} \left(\frac{\|\partial V_{ij}(p, s) - p_i\|^2}{\|p_j - p_i\|} \phi_{s(i)}(\partial V_{ij}(p, s), t) \|\partial V_{ij}(p)\| \right) ds \\ &\quad - \frac{1}{\mu_{ij}} \rho_{ij} \frac{\partial \mu_{ij}}{\partial p_i}.\end{aligned}$$

The analytical expressions for these derivatives can be calculated by directly plugging the parameterized expression for the Voronoi boundary in (4.29) and its endpoints, as calculated in (4.33). The partial derivatives for $\partial \mu_{ji}/\partial p_i$ and $\partial \rho_{ji}/\partial p_i$ can be computed in an analogous fashion.

Having calculated all the partial derivatives needed in (4.23), (4.24) and (4.25), the analytical expression of $\partial J_{het}/\partial p_i$ is fully determined.

Computation of $\partial J_{het,i}/\partial t$

In order to solve the optimization problem in (4.15), the following derivative is needed,

$$\begin{aligned}\frac{\partial J_{het,i}(p, t)}{\partial t} &= \frac{1}{\kappa^2} u_i^T \frac{\partial u_i}{\partial t} \\ &= \frac{1}{\kappa} u_i^T \left[2\sigma \left((p_i - c_i) \frac{\partial m_i}{\partial t} - m_i \frac{\partial c_i}{\partial t} \right) \right.\end{aligned}\tag{4.34}$$

$$\left. + 2(1 - \sigma) \left((p_i - c_i) \frac{\partial M_i}{\partial t} - M_i \frac{\partial C_i}{\partial t} \right) \right.\tag{4.35}$$

$$\left. - \sigma \sum_{j \in \mathcal{N}_i} \left[(p_i - \rho_{ij}) \frac{\partial \mu_{ij}}{\partial t} - \mu_{ij} \frac{\partial \rho_{ij}}{\partial t} - (p_i - \rho_{ij}) \frac{\partial \mu_{ji}}{\partial t} - \mu_{ij} \frac{\partial \rho_{ij}}{\partial t} \right] \right].\tag{4.36}$$

The computation of the partial derivatives involved in $\partial J_{het,i}/\partial t$, however, is less involved than in the case of $\partial J_{het,i}/\partial p_i$ (detailed previously in this section), since none of the domains of integration depend on t . The partial derivatives in (4.34), (4.35) and (4.36) take

the following form,

$$\begin{aligned}
\frac{\partial m_i(p, t)}{\partial t} &= \int_{V_i(p)} \frac{\partial \phi_{s(i)}(q, t)}{\partial t} dq, & \frac{\partial c_i(p, t)}{\partial t} &= \frac{\int_{V_i(p)} q \frac{\partial \phi_{s(i)}(q, t)}{\partial t} dq}{m_i} - \frac{1}{m_i} c_i \frac{\partial m_i}{\partial t}, \\
\frac{\partial M_i(t)}{\partial t} &= \int_{\mathcal{D}} \frac{\partial \phi_{s(i)}(q, t)}{\partial t} dq, & \frac{\partial C_i(t)}{\partial t} &= \frac{\int_{\mathcal{D}} q \frac{\partial \phi_{s(i)}(q, t)}{\partial t} dq}{M_i} - \frac{1}{M_i} C_i \frac{\partial M_i}{\partial t}, \\
\frac{\partial \mu_{ij}(p, t)}{\partial t} &= \int_{\partial V_{ij}(p)} \frac{\|q - p_i\|^2}{\|p_j - p_i\|} \frac{\partial \phi_{s(i)}(q, t)}{\partial t} dq, \\
\frac{\partial \rho_{ij}(p, t)}{\partial t} &= \frac{\int_{\partial V_{ij}(p)} q \frac{\|q - p_i\|^2}{\|p_j - p_i\|} \frac{\partial \phi_{s(i)}(q, t)}{\partial t} dq}{\mu_{ij}} - \frac{1}{\mu_{ij}} \rho_{ij} \frac{\partial m_{ij}}{\partial t}.
\end{aligned}$$

Armed with the partial derivatives in $\partial J_{het,i}/\partial p_i$ and $\partial J_{het,i}/\partial t$, we can directly use the constraint-driven formulation in (4.15) and obtain a quadratic optimization problem similar to the one in (4.16) to solve the time-varying heterogeneous coverage problem in (4.19).

4.5.2 Time-Varying Communication-Aware Heterogeneous Coverage

The coverage problem with heterogeneous sensing capabilities was approach differently in Section 3.3, where the robots were allowed to communicate about their sensor suites to improve the overall coverage performance. Having information about its neighbors implies that Robot i can calculate its region of dominance with respect to Sensor $j \in s(i) \subset \mathcal{S}$,

$$V_i^j(p) = \{q \in \mathcal{D} \mid \|q - p_i\| \leq \|q - p_j\|, \forall k \in \mathcal{N}^j\}, \quad \mathcal{N}^j = \{i \in \mathcal{N} \mid j \in s(i)\}.$$

With these sensor-dependent partitions of the domain, the performance of the multi-robot team under the family of time-varying density functions $\phi_j(q, t), j \in \mathcal{S}$, can be encoded

through the locational cost analogous to (3.16),

$$\mathcal{H}_{com}(p, t) = \sum_{j \in \mathcal{S}} \sum_{i \in \mathcal{N}^j} \int_{V_i^j(p)} \|q - p_i\|^2 \phi_j(q, t) dq. \quad (4.37)$$

Note that, for simplicity, this section considers the degradation function for all sensors to be the square of the Euclidean distance, i.e. $d_j(q_1, q_2) = \|q_1 - q_2\|^2, \forall j \in \mathcal{S}$. Similar calculations to the ones outlined in this section can be applied to the time-varying version of the original communication-aware locational cost (3.16).

According to Theorem 3.3, the cost (4.37) can be minimized by letting Robot $i, i \in \mathcal{N}$ execute the control law,

$$u_i = 2 \sum_{j \in s(i)} m_i^j (c_i^j - p_i),$$

where $m_i^j(p, t)$ and $c_i^j(p, t)$ are given by

$$m_i^j(p, t) = \int_{V_i^j(p)} \phi_j(q, t) dq, \quad c_i^j(p, t) = \frac{\int_{V_i^j(p)} q \phi_j(q, t) dq}{m_i^j}.$$

Analogously to what was done for \mathcal{H}_{het} , we can define a cost $J_{com}(p, t)$ whose minimizer is the minimizer of the corresponding locational cost, i.e. (4.37),

$$J_{com}(p, t) = \sum_{i=1}^N \frac{1}{2} \|u_i\|^2 = \sum_{i=1}^n J_{com,i}(p, t).$$

In order to solve the optimization problem in (4.15), which asymptotically drives the robots to a stationary point of $J_{com}(p, t)$, we need the expressions for the partial derivatives of $\partial J_{com,i} / \partial p_i$ and $\partial J_{com,i} / \partial t$.

Computation of $\partial J_{com,i}/\partial p_i$

The derivative of the contribution of Robot i , $\partial J_{com,i}(p, t)$, with respect to its position, p_i , becomes,

$$\frac{\partial J_{com,i}(p, t)}{\partial p_i} = u_i^\top \frac{\partial u_i}{\partial p_i} = u_i^\top \left[2 \sum_{j \in s(i)} (c_i^j - p_i) \frac{\partial m_i^j}{\partial p_i} + m_i^j \left(\frac{\partial c_i^j}{\partial p_i} - I \right) \right],$$

Similarly to (4.26) and (4.27), the derivatives of the mass and center of mass of Robot i with respect to Sensor j can be written as

$$\begin{aligned} \frac{\partial m_i^j(p, t)}{\partial p_i} &= \sum_{j \in \mathcal{N}_i} \int_{\partial V_{ij}(p)} \phi_j(q, t) \frac{(q - p_i)^\top}{\|p_j - p_i\|} dq \\ \frac{\partial c_i^j(p, t)}{\partial p_i} &= \frac{1}{m_i} \sum_{j \in \mathcal{N}_i} \int_{\partial V_{ij}(p)} (q - c_i) \phi_j(q, t) \frac{(q - p_i)^\top}{\|p_j - p_i\|} dq. \end{aligned}$$

Computation of $\partial J_{com,i}/\partial t$

On the other hand, the derivative of $\partial J_{com,i}(p, t)$, with respect to time,

$$\frac{\partial J_{com,i}(p, t)}{\partial t} = u_i^\top \frac{\partial u_i}{\partial t} = 2u_i^\top \sum_{j \in s(i)} \left[(c_i^j - p_i) \frac{\partial m_i^j}{\partial t} + m_i^j \frac{\partial c_i^j}{\partial t} \right],$$

with

$$\frac{\partial m_i^j(p, t)}{\partial t} = \int_{V_i(p)} \frac{\partial \phi_j(q, t)}{\partial t} dq, \quad \frac{\partial c_i^j(p, t)}{\partial t} = \frac{\int_{V_i(p)} q \frac{\partial \phi_j(q, t)}{\partial t} dq}{m_i^j} - \frac{1}{m_i^j} c_i \frac{\partial m_i^j}{\partial t}.$$

With the partial derivatives $\partial J_{com,i}/\partial p_i$ and $\partial J_{com,i}/\partial t$ completely defined, the constraint driven formulation in (4.15) can be used to obtain a quadratic optimization problem similar to the one in (4.16). Thus, we obtain a decentralized controller to solve the time-

varying heterogeneous coverage problem specified by the locational cost (4.37).

4.6 Conclusions

This chapter develops an exact and decentralized algorithm for the multi-robot time-varying coverage control problem. In our approach, the coverage objective is encoded as a constraint in a minimum-energy optimization program executed by each robot. Slack variables encoded within the constraint ensure feasibility of the optimization program. The performance of our algorithm is compared with other approaches to demonstrate how the constraint-based method effectively covers a region with time-varying importance densities in a decentralized and approximation-free manner. The equations for the decentralized algorithm to be applied to the heterogeneous coverage problem included in Chapter 3 are also included in this chapter.

CHAPTER 5

MULTI-ROBOT PAINTING THROUGH COLORED MOTION TRAILS

The intersection of robots and arts has become an active object of study as both researchers and artists push the boundaries of the traditional conceptions of different forms of art (see Section 2.2 for a literature review on robots and art). In the context of robotic painting, the focus has been primarily on robotic arms capable of rendering input images according to some aesthetic specifications [103, 202], or even reproducing scenes from the robot’s surroundings—e.g. portraits [104] or inanimated objects [129]. The production of abstract paintings with similar robotic arm setups remains mostly unexplored, with some exceptions [134]. The idea of swarm painting has been primarily explored within computer generated paintings, where virtual painting agents move inspired by ant behaviors [136, 137, 138]. Regarding physical robotic swarms, the creation of artistic paintings is scarce, with existing examples relying on the use of preprogrammed controllers [118, 119], which hinder any interactive influence of the human artist once the creation process has begun. While other approaches to swarm painting [120] have consider the participation of the human artist on the creation process, their role has been relegated to that of a co-creator of the work of art, since they can add strokes to the painting but their actions do not influence the operation of the multi-robot team.

In this chapter, we present a multi-robot painting system based on ground robots that lay color trails as they move throughout a canvas, shown in Fig. 5.1. The novelty of this approach lies in the fact that an external user—the artist—can influence the movement of robots capable of painting specific colors, thus controlling the concentration of certain pigments on different areas of the painting canvas. Inspired by [8], this human-swarm interaction is formalized through the use of scalar fields—which we refer to as *density functions*—associated with the different colors such that, the higher the color density specified

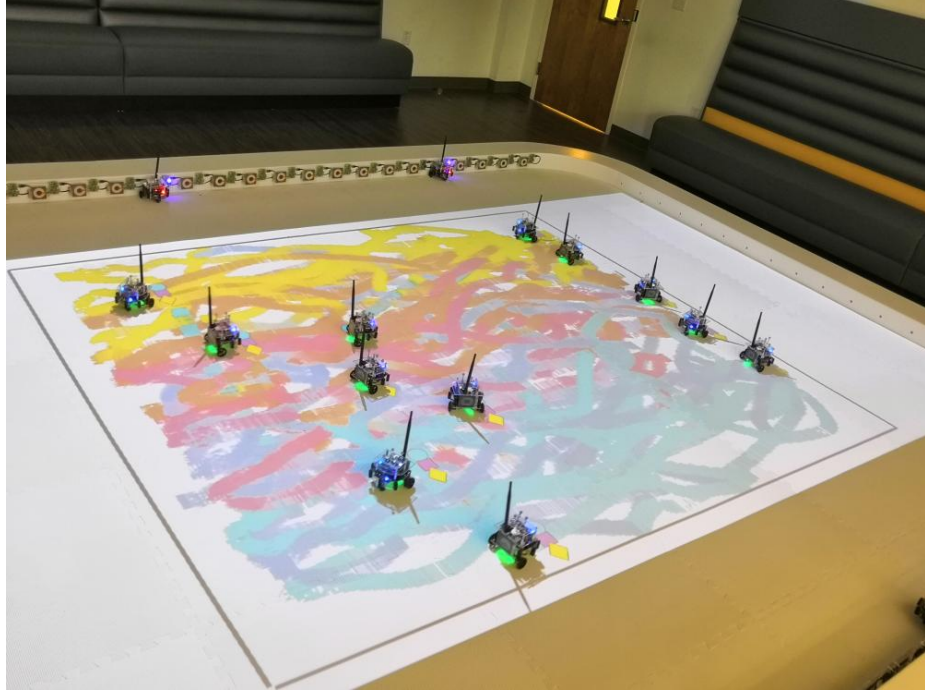


Figure 5.1: A group of 12 robots generating a painting based on the densities specified by a human user for 5 different color tones: cyan, blue, pink, orange and yellow. The robots lay colored trails as they move throughout the canvas, distributing themselves according to their individual painting capabilities. The painting arises as a result of the motion trails integrating over time.

at a particular point, the more attracted the robots equipped with that color will be to that location. Upon the specification of the color densities, the robots distribute themselves over the canvas in a distributed fashion by executing a controller that optimally covers the density objectives specified by the operator based on the heterogeneous painting capabilities of the robots in the team [184, 185]. Thus, the system provides the artist with a high-level way to control the painting behavior of the swarm as a whole, agnostic to the total number of robots in the team or the specific painting capabilities of each of them.

The remainder of the chapter is organized as follows: In Section 5.1, we recall the problem of coverage control and its extension to heterogeneous robot capabilities as it enables the human-swarm interaction modality used in this chapter. Section 5.2 elaborates on the generation of color densities to be tracked by the multi-robot system along with the color selection strategy adopted by each robot for its colored trail. A series of experiments

conducted on a team of differential-drive robots is presented in Section 5.3, where different painting compositions arise as a result of assigning different painting capabilities—both in terms of paints given to the individual robots as well as total paint available—to the multi-robot team. The effects of this heterogeneous resources on the final color distributions observed on the paintings are discussed in Section 5.4. Section 5.5 concludes the chapter.

5.1 Density-Based Multi-Robot Control

The interactive multi-robot painting system presented in this chapter operates based on the specification of desired concentration of different colors over the painting canvas. This color preeminence is encoded through color density functions that the artist can set over the domain to influence the trajectories of the robots and, thus, produce the desired coloring effect. In this section, we recall the formulation of the coverage control problem as it serves as the mathematical backbone for the human-swarm interaction modality considered in this chapter.

5.1.1 Coverage Control

The coverage control problem deals with the question of how to distribute a team of N robots with positions $p_i \in \mathbb{R}^d, i \in \{1, \dots, N\} =: \mathcal{N}$, to optimally cover the environmental features of a domain $\mathcal{D} \in \mathbb{R}^d, d = 2$ for ground robots (see Section 2.1 for a detailed explanation of this problem formulation). The question of how well the team is covering a domain is typically asked with respect to a density function, $\phi : \mathcal{D} \mapsto [0, \infty)$, that encodes the importance of the points in the domain. Denoting the aggregate positions of the robots as $p = [p_1^T, \dots, p_N^T]^T$, the performance of the multi-robot team with respect to ϕ can then be encoded through the locational cost in [6],

$$\mathcal{H}(p) = \sum_{i=1}^N \int_{V_i(p)} \|p_i - q\|^2 \phi(q) dq, \quad (5.1)$$

with a lower value of the cost corresponding to a better coverage. $V_i(p) = \{q \in \mathcal{D} \mid \|q - p_i\| \leq \|q - p_j\|, \forall j \in \mathcal{N}\}$ denotes the Voronoi cell of Robot i with respect to the Euclidean distance.

A necessary condition for (5.1) to be minimized is that the position of each robot corresponds to the center of mass of its Voronoi cell [45], given by

$$c_i(p) = \frac{\int_{V_i(p)} q \phi(q) dq}{\int_{V_i(p)} \phi(q) dq}.$$

This spatial configuration, referred to as a centroidal Voronoi tessellation, can be achieved by letting the multi-robot team execute the well-known Lloyd's algorithm [43], whereby

$$\dot{p}_i = \kappa(c_i(p) - p_i). \quad (5.2)$$

The power of the locational cost in (5.1) lies on its ability to influence which areas of the domain the robots should concentrate by specifying a single density function, ϕ , irrespectively of the number of robots in the team. This makes coverage control an attractive paradigm for human-swarm interaction, as introduced in [8], since a human operator can influence the collective behavior of an arbitrarily large swarm by specifying a single density function. In this paper, however, we consider a scenario where a human operator can specify multiple density functions associated with the different colors to be painted and, thus, a controller encoding such color heterogeneity must be considered. The following section recalls a formulation of the coverage problem for multi-robot teams with heterogeneous capabilities and a control law that allows the robots to optimally cover a number of different densities.

5.1.2 Coverage With Heterogeneous Painting Capabilities

The human-swarm interaction modality considered in this chapter allows the artist to specify a set of density functions associated with different colors to produce desired concentra-

tions of colors over the canvas. To this end, we recover the heterogeneous coverage control formulation from Section 3.3. Let \mathcal{P} be the set of paint colors and $\phi_j : \mathcal{D} \mapsto [0, \infty)$, $j \in \mathcal{P}$, the family of densities associated with the colors in \mathcal{P} defined over the convex domain, \mathcal{D} , i.e. the painting canvas. In practical applications, the availability of paints given to each individual robot may be limited due to payload limitations, resource depletion, or monetary constraints. To this end, let Robot i , $i \in \mathcal{N}$, be equipped with a subset of the paint colors, $\pi(i) \subset \mathcal{P}$, such that it can paint any of those colors individually or a color that results from their combination. The specifics concerning the color mixing strategy executed by the robots are described in detail in Section 5.2.

Analogously to (5.1), the quality of coverage performed by Robot i with respect to Color j can be encoded through the locational cost

$$h_i^j(p) = \int_{V_i^j(p)} \|p_i - q\|^2 \phi_j(q) dq, \quad (5.3)$$

where V_i^j is the region of dominance of Robot i with respect to Color j , delimited by those robots also capable of painting Color j . If we denote as \mathcal{N}^j the set of robots equipped with Color j , $\mathcal{N}^j = \{i \in \mathcal{N} \mid j \in \pi(i) \subset \mathcal{P}\}$, then the region of dominance of Robot i with respect to Color $j \in \pi(i)$ is the Voronoi cell in the tessellation whose generators are the robots in \mathcal{N}^j ,

$$V_i^j(p) = \{q \in \mathcal{D} \mid \|p_i - q\| \leq \|p_k - q\|, \forall k \in \mathcal{N}^j\}.$$

Note that, if Robot i is the only robot equipped with Color j , then the robot is in charge of covering the whole canvas, i.e. $V_i^j = \mathcal{D}$.

With the regions of dominance defined, we can now evaluate the cost in (5.3) and, thus, recover the *heterogeneous locational cost* in (3.16), here instantiated with the square of the

Euclidean distance as the degradation function,

$$\mathcal{H}_{com}(p) = \sum_{j \in \mathcal{P}} \sum_{i \in \mathcal{N}^j} \int_{V_i^j(p)} \|p_i - q\|^2 \phi_j(q) dq, \quad (5.4)$$

with a lower value of the cost corresponding to a better coverage of the domain with respect to the family of color density functions ϕ_j , $j \in \mathcal{P}$.

According to Theorem 3.3, the cost in (5.4) can be minimized by letting each robot follow a negative gradient,

$$\dot{p}_i = \kappa \sum_{j \in \pi(i)} m_i^j(p) (c_i^j(p) - p_i), \quad \kappa > 0 \quad (5.5)$$

where $m_i^j(p)$ and $c_i^j(p)$ are, respectively, the *heterogeneous mass* and *center of mass* of Robot i with respect to Color j , defined as in (3.27),

$$m_i^j(p) = \int_{V_i^j(p)} \phi_j(q) dq, \quad c_i^j(p) = \frac{\int_{V_i^j(p)} q \phi_j(q) dq}{m_i^j}. \quad (5.6)$$

Therefore, the controller that minimizes the heterogeneous locational cost in (5.4) makes each robot move according to a weighted sum where each term corresponds with a continuous-time Lloyd descent—analogueous to (5.2)—over a particular color density ϕ_j , weighted by the mass corresponding to that painting capability.

The controller in (5.5) thus enables an effective human-swarm interaction modality for painting purposes where the artist only has to specify color density functions for the desired color composition and the controller allows the robots in the team to distribute themselves over the canvas according to their heterogeneous painting capabilities. Note that, while other human-swarm interaction paradigms based on coverage control have considered time-varying densities to model the input provided by an external operator [8], in the application considered in this chapter heterogeneous formulation of the coverage control problem, while considering static densities, suffices to model the information exchange

between the artist and the multi-robot system.

5.2 From Coverage Control to Painting

In Section 5.1, we established a human-swarm interaction paradigm that allows the artist to influence the team of robots so that they distribute themselves throughout the canvas according to a desired distribution of color and their painting capabilities. But how is the painting actually created? In this section, we present a strategy that allows each robot to choose the proportion in which the colors available in its equipment should be mixed in order to produce paintings that reflect, to the extent possible, the distributions of color specified by the artist.

The multi-robot system considered in this chapter is conceived to create a painting by means of each robot leaving a trail of color as it moves over a white canvas. While the paintings presented in Section 5.3 do not use physical paint but, rather, projected trails over the robot testbed, the objective of this section is to present a color model that both allows the robots to produce a wide range of colors with minimal painting equipment and that closely reflects how the color mixing would occur in a scenario where physical paint were to be employed. To this end, in order to represent a realistic scenario where robots lay physical paint over a canvas, we use the subtractive color mixing model (see [203] for an extensive discussion in color mixing), which describes how dyes and inks are to be combined over a white background to absorb different wavelengths of white light to create different colors. In this model, the primary colors that act as a basis to generate all the other color combinations are cyan, magenta and yellow (CMY).

The advantage of using a simple model like CMY is twofold. Firstly, one can specify the desired presence of an arbitrary color in the canvas by defining in which proportion these should mix at each point and, secondly, the multi-robot system as a collective can generate a wide variety of colors being equipped with just cyan, magenta and yellow paint, i.e. $\mathcal{P} = \{C, M, Y\}$ in the heterogeneous multi-robot control strategy in Section 5.1.2.

The first aspect reduces the interaction complexity between the human and the multi-robot system: the artist can specify a desired set of colors \mathcal{C} throughout the canvas by defining the CMY representation of each color $\beta \in \mathcal{C}$ as $[\beta_C, \beta_M, \beta_Y]$, $\beta_j \in [0, 1]$, $j \in \mathcal{P}$, and its density function over the canvas $\phi_\beta(q)$, $q \in \mathcal{D}$. Note that a color specified in the RGB color model (red, green and blue), represented by the triple $[\beta_R, \beta_G, \beta_B]$, can be directly converted to the CMY representation by subtracting the RGB values from 1, i.e. $[\beta_C, \beta_M, \beta_Y] = 1 - [\beta_R, \beta_G, \beta_B]$. Given that the painting capabilities of the multi-robot system are given by $\mathcal{P} = \{C, M, Y\}$, the densities that the robots are to cover according to the heterogeneous coverage formulation in Section 5.1.2 can be obtained as,

$$\phi_j(q) = \bigoplus_{\beta \in \mathcal{C}} \beta_j \phi_\beta(q), \quad j \in \mathcal{P},$$

where \oplus is an appropriately chosen composition operator. The choice of composition operator reflects how the densities associated with the different colors should be combined in order to compute the overall density function associated with each CMY primary color. For example, one way to combine the density functions is to compute the maximum value at each point,

$$\phi_j(q) = \max_{\beta \in \mathcal{C}} \beta_j \phi_\beta(q), \quad j \in \mathcal{P}.$$

The question remaining is how a robot should combine its available pigments in its color trail to reflect the desired color density functions. The formulation of the heterogeneous locational cost in (5.4) implies that Robot i is in charge of covering Color j within the region dominance V_i^j and of covering Color k within V_i^k , $j, k \in \pi(i) \subset \mathcal{P}$. However, depending on the values of the densities ϕ_j and ϕ_k within these Voronoi cells, the ratio between the corresponding coverage responsibilities may be unbalanced. In fact, such responsibilities are reflected naturally through the heterogeneous mass, $m_i^j(p)$, defined in (5.6). Let us denote as $[\alpha_i^C, \alpha_i^M, \alpha_i^Y]$, $\alpha_i^j \in [0, 1]$, $\alpha_i^C + \alpha_i^M + \alpha_i^Y = 1$, the color proportion in the CMY basis to be used by Robot i in its paint trail. Then, a color mixing strategy that

reflects the coverage responsibilities of Robot i can be given by,

$$\alpha_i^j = \frac{m_i^j(p)}{\sum_{k \in \pi(i)} M_i^k(p)}, \quad j \in \pi(i) \subset \mathcal{P}. \quad (5.7)$$

Note that, when $m_i^j(p) = 0, \forall j \in \pi(i) \subset \mathcal{P}$, the robot is not covering any density and, thus, $\alpha_i^j, j \in \mathcal{P}$, can be undefined.

Figure 5.2 illustrates the operation of this painting mechanism for three different density color specifications. Firstly, the mechanism is simulated for a robot equipped with all three colors—cyan (C), magenta (M) and yellow (Y)—in Figs. 5.2a, 5.2c and 5.2e. As seen, the robot lays a cyan trail as it moves to optimally cover a single cyan density function in Fig. 5.2a. In Fig. 5.2c, two different density functions are specified, one magenta and one yellow, and the robot lays down a trail whose color is a combination of both paints. Finally, in Fig. 5.2e, the robot is tasked to cover a density that is a combination of the CMY colors. Since the robot is equipped with all three colors, the trail on the canvas exactly replicates the colors desired by the user.

For the same input density specifications, Figs. 5.2b, 5.2d, and 5.2f illustrate the trails generated by a team of 3 robots equipped with different subsets of the color capabilities. As seen, the color of the individual robot trails evolve as a function of the robot's equipment, the equipments of its neighbors, and the specified input density functions.

5.3 Experimental Results With Projected Trails

The proposed multi-robot painting system is implemented on the Robotarium, a remotely accessible swarm robotics testbed at the Georgia Institute of Technology [191]. The human-swarm interaction paradigm for color density coverage presented in Section 5.1 and the trail color mixing strategy from Section 5.2 are illustrated experimentally on a team of 12 differential drive robots tasked to paint a set of user-defined color density functions over a 2.4×2 m canvas. In order to study how the limited availability of painting resources affects

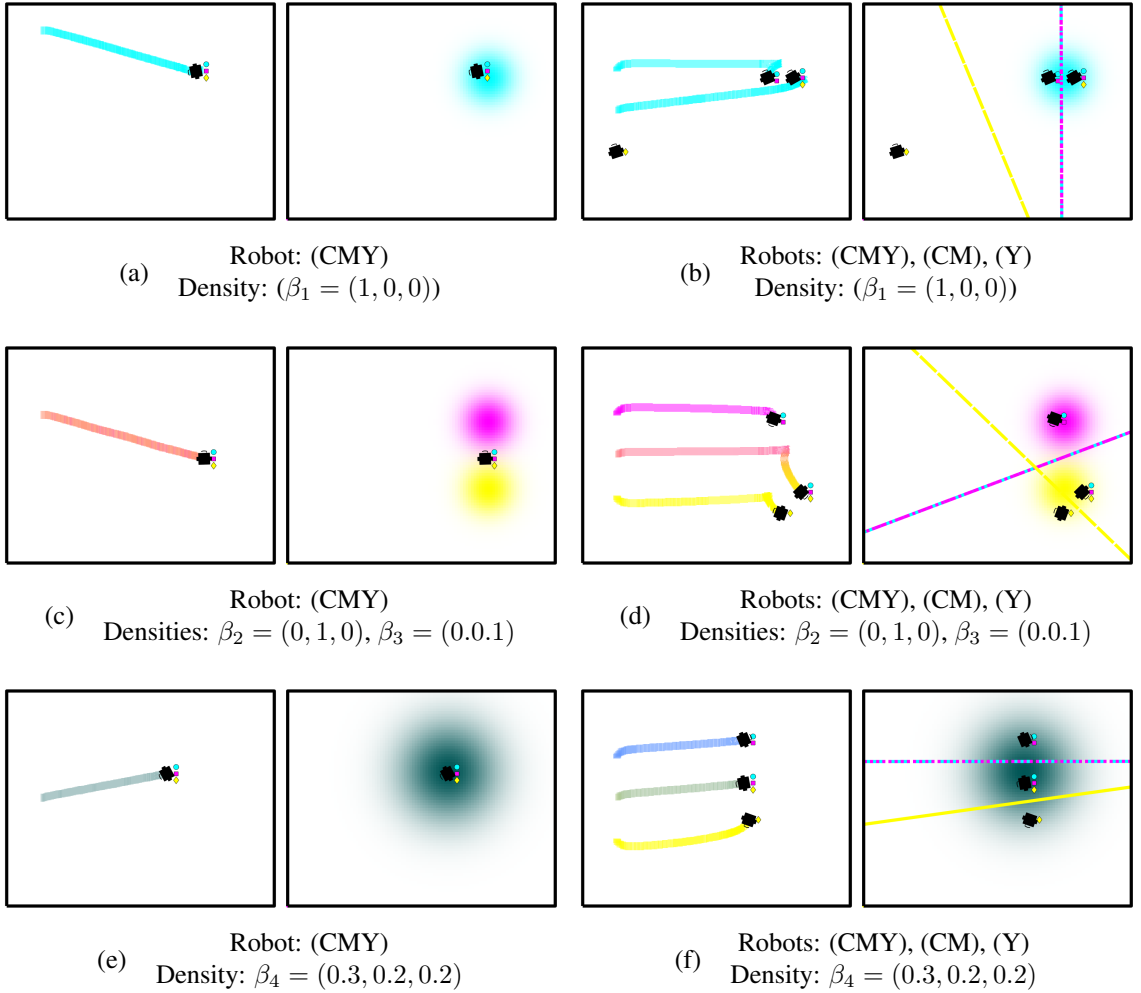








Figure 5.2: Painting mechanism based on heterogeneous coverage control. Each subfigure shows the color trails laid by the robots (left) as they move to optimally cover a user-specified color density function (right) by executing the controller in (5.5). The symbols located to the right of the robot indicate its painting capabilities. Figures (a), (c) and (e) show the operation of the painting mechanism in Section 5.2 for a single robot equipped with all three colors, i.e. cyan (C), magenta (M) and yellow (Y), thus capable of producing all color combinations in the CMY basis. In (a), the robot lays a cyan trail according to the density color specification β_1 . The robot equally mixes magenta and yellow in (c) according to the color mixing strategy in (5.7), producing a color in between the two density color specifications, β_2 and β_3 . Finally, in (e), the robot exactly replicates the color specified by β_4 . On the other hand, Figures (b), (d) and (f) depict the operation of the painting mechanism with a team of 3 robots, where the Voronoi cells (color coded according to the CMY basis) are shown on the density subfigures.

the resulting painting, for the same painting task, 9 different experimental setups in terms of paint equipment assigned to the multi-robot team are considered. While no physical

Table 5.1: Experimental parameters associated with the user-specified color density functions.

β	Color	β_C	β_M	β_Y	K	μ_x	μ_y	σ_x	σ_y	A_x	A_y	f_x	f_y
1		.0000	.0863	.5569	60	0	.8	.22	.22	1.1	0.1	1/40	0
2		.0000	.3529	.5569	40	0	.4	.22	.22	1.1	0.1	1/37	2/15
3		.0549	.5529	.3451	40	0	0	.22	.22	1.1	0.1	1/35	0
4		.4314	.3098	.1373	60	0	-.4	.22	.22	1.1	0.1	1/33	2/15
5		.9686	.0353	.0275	40	0	-.8	.22	.22	1.1	0.1	1/30	0
6		0	0	1	60	0.5	.3	.125	.125	0.1	0.1	1/5	1/5

paint is used in the experiments included in this chapter, the effectiveness of the proposed painting system is illustrated by visualizing the robots' motion trails over the canvas with an overhead projector.

The experiment considers a scenario where the multi-robot team has to simultaneously cover a total of six different color density functions over a time horizon of 300 seconds. The color density functions are of the form,

$$\phi_\beta(q) = \frac{K}{2\pi\sigma_x\sigma_y} \exp\left(-\frac{(q_x - \bar{\mu}_x)^2 + (q_y - \bar{\mu}_y)^2}{2\sigma_x^2\sigma_y^2}\right), \quad (5.8)$$

with $\beta \in \{1, \dots, 6\} = \mathcal{C}$, $q = [q_x, q_y]^T \in D$. The color associated with each density as well as its parameters are specified in Table 5.1, and $\bar{\mu}_x$ and $\bar{\mu}_y$ are given by

$$\begin{aligned} \bar{\mu}_x &= \mu_x - A_x \sin(2 * \pi f_x t), \\ \bar{\mu}_y &= \mu_y - A_y \sin(2 * \pi f_y t). \end{aligned}$$

Figure 5.3 illustrates the evolution of the painting for a specific equipment setup as the robots move to cover these densities at $t = 100s$ and $t = 300s$.

In order to evaluate how the heterogeneous painting capabilities of the multi-robot team

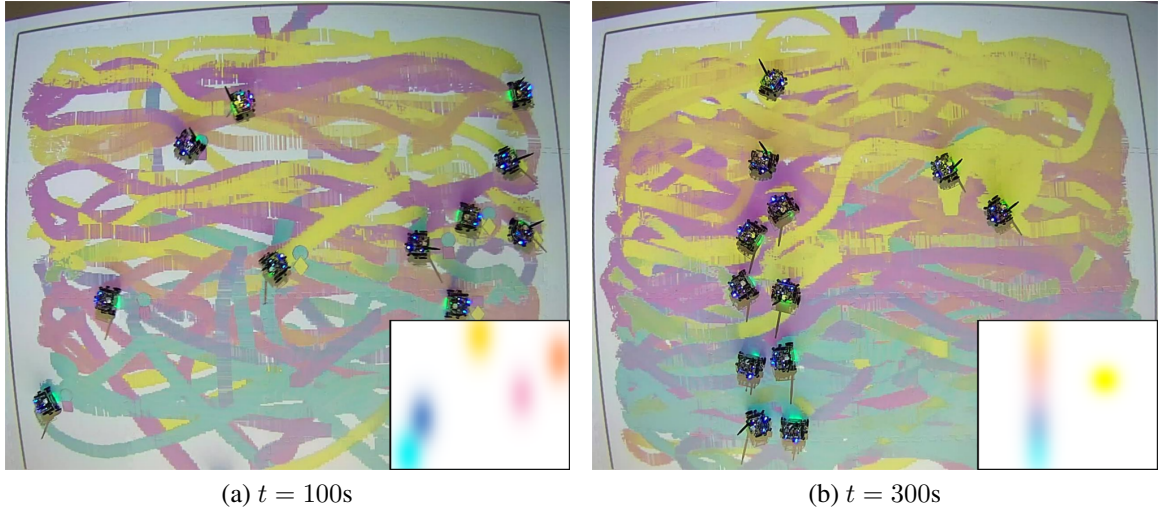


Figure 5.3: Evolution of the painting according to the density parameters in Table 5.1, for the Setup 3 given as in Table 5.2. The robots distribute themselves over the domain in order to track the density functions as they evolve through the canvas. The color distribution of the color trails reflects the colors specified for the density functions within the painting capabilities of the robots. Even though none of the robots is equipped with the complete CMY equipment and, thus, cannot reproduce exactly the colors specified by the user, the integration of the colors over time produce a result that is close to the user’s density specification.

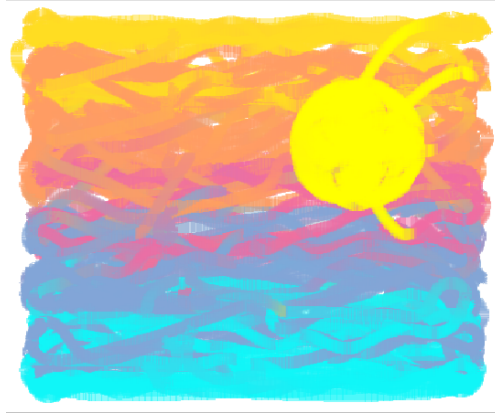
affect the outcome of the painting process, the coverage of the color densities is evaluated for 9 different equipment configurations. Table 5.2 outlines the color painting capabilities available to each of the robots in the different experimental setups. The paintings which result from five of these configurations (the ones with an odd setup ID) are shown in Fig. 5.4. For the purpose of benchmarking, a simulated painting is generated for painting setup 1, i.e. with complete painting capabilities, under the same heterogeneous density coverage control and color mixing strategies as in the robotic experiments (Fig. 5.4a). Given the paintings in Figs. 5.4b to 5.4f, we can observe how the closest color distribution to the simulated painting is achieved in Fig. 5.4b, which corresponds to the case where all the robots have all the painting capabilities—i.e. the team is homogeneous—and, thus, can reproduce any combination of colors in the CMY basis.

It is interesting to note the significant changes in the characteristics of the painting for different equipment configurations of the robots. For equipment setups 3, 5, 7 and 9,

Table 5.2: Paint equipment for the different experimental setups.

Setup ID	Paint Equipment																	Heterogeneity	
	ID	1	2	3	4	5	6	7	8	9	10	11	12	13	14	15	Total	Sunset	8-bit RGB
1	C	×	×	×	×	×	×	×	×	×	×	×	×				12	0	0
	M	×	×	×	×	×	×	×	×	×	×	×	×				12		
	Y	×	×	×	×	×	×	×	×	×	×	×	×	×			12		
2	C	×			×		×	×	×	×	×	×	×	×	×	×	12	.2786	.2680
	M		×		×	×		×	×	×	×	×	×	×	×	×	12		
	Y			×		×	×	×	×	×	×	×	×	×	×	×	12		
3	C	×	×			×	×	×	×			×	×				8	.3060	.2963
	M	×	×	×	×			×	×	×	×						8		
	Y			×	×	×	×			×	×	×	×				8		
4	C	×		×	×	×		×		×	×	×	×				9	.3340	.3121
	M		×	×		×	×	×	×		×	×	×				9		
	C		×	×		×	×		×	×	×	×	×				9		
5	C	×			×		×	×	×	×	×	×	×				9	.3921	.3783
	M		×		×	×		×	×	×	×	×	×				9		
	Y			×		×	×	×	×	×	×	×	×	×			9		
6	C	×	×					×	×	×	×	×	×				8	.4488	.4398
	M			×	×			×	×	×	×	×	×				8		
	Y					×	×	×	×	×	×	×	×	×			8		
7	C	×			×	×			×	×	×	×	×				8	.5686	.5498
	M		×		×	×	×	×			×	×	×				8		
	Y			×			×	×	×	×	×	×	×	×			8		
8	C	×	×	×								×	×	×			6	.6904	.6835
	M				×	×	×				×	×	×				6		
	Y							×	×	×	×	×	×	×			6		
9	C	×	×					×	×			×	×				6	.8148	.8004
	M			×	×			×	×	×	×						6		
	Y					×	×			×	×	×	×				6		

where some robots—or all—are not equipped with all the color paints, the corresponding paintings do not show as smooth color gradients as the one in Fig. 5.4b. However, the



(a) Simulated painting, Setup 1



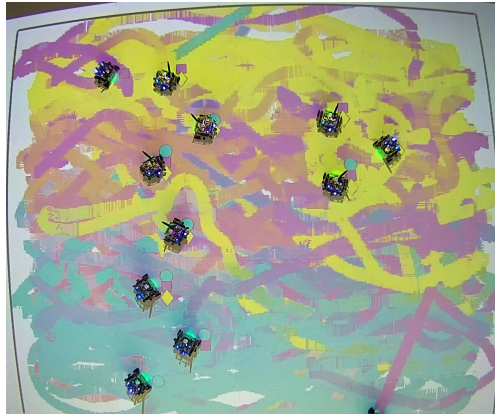
(b) Setup 1



(c) Setup 3



(d) Setup 5



(e) Setup 7



(f) Setup 9

Figure 5.4: Paintings generated for the densities in (5.8), with the team of 12 robots in their final positions. Figure 5.4a corresponds to a simulated painting and it is used for benchmarking. According to the painting equipment setups in Table 5.2 we can see how, as the robots in the team are equipped with more painting capabilities, the color gradients become smoother and more similar to the ideal outcome.

distribution of color for these paint setups still qualitatively reflects the color specification given by the densities in Table 5.1. Even in the extreme case of Equipment 9 (see Fig. 5.4f), where none of the robots is equipped with all CMY paints—in fact, half of the robots only have one paint and the other half have pairwise combinations—the robot team still renders a painting that, while presenting colors with less smooth blending than the other setups, still represents the color distribution specified by the densities in Table 5.1. For setups 3 and 7, the team has the same total number of CMY painting capabilities but the distribution is different among the team members: in Setup 3 none of the robots are equipped with the three colors, while in Setup 7 there are some individuals that can paint any CMY combination and others can paint only one color. Observing the Figs. 5.4c and 5.4e, while the resulting colors are less vibrant for the equipment in Setup 3, there seems to be a smoother blending between them along with the vertical axis. Setup 7 produces a painting where overall the colors are more faithful to the ideal outcome presented in Fig. 5.4a, but that also contain stronger trails corresponding to the pure primary colors appear throughout the painting. If we compare Figs. 5.4e and 5.4d we can see how, by adding a small amount of painting capabilities to the system, the color gradients are progressively smoothed. This observation suggests to further analyze the variations that appear on the paintings as a function of the heterogeneous equipment configurations of the different setups. This will be the focus of the next section.

5.4 Discussion

The robotic painting system developed in this chapter generates illustrations via an interaction between the color density functions specified by the user and the different color equipment present on the robots. In particular, the different equipments not only affect the color trails left by the robots, but also affect their motion as they track the density functions corresponding to their equipment. While Fig. 5.4 qualitatively demonstrates how the nature of the painting varies with different equipment setups, this section presents a quanti-

tative analysis of the variations among paintings resulting from different equipment setups. We also analyze the reproducibility characteristics of the multi-robot painting system, by investigating how paintings vary among different realizations using the same equipment setups.

Let S denote the number of distinct equipment setups of the robots in the team—where each unique configuration denotes a robot *species*. We denote $s_\iota \in [0, 1]$ as the probability that a randomly chosen agent belongs to species ι , $\iota \in \mathcal{S} = \{1, \dots, S\}$, such that

$$\sum_{\iota=1}^S s_\iota = 1, \quad \text{and } s = [s_1, \dots, s_S]^T.$$

For each equipment setup in Table 5.2, these probabilities can be calculated as a function of how many agents are equipped with each subset of the paint colors.

We adopt the characterization developed in [204], and quantify the heterogeneity of a multi-robot team as,

$$H(s) = E(s)Q(s), \tag{5.9}$$

where $E(s)$ represents the *complexity* and $Q(s)$, the *disparity* within the multi-robot system for a given experimental setup, s . More specifically, $E(s)$ can be modeled as the *entropy* of the multi-agent system,

$$E(s) = - \sum_{\iota=1}^S s_\iota \log(s_\iota),$$

and $Q(s)$ is the *Rao's Quadratic Entropy*,

$$Q(s) = \sum_{\iota=1}^S \sum_{\kappa=1}^S s_\iota s_\kappa \delta(\iota, \kappa)^2, \tag{5.10}$$

with $\delta : \mathcal{S} \times \mathcal{S} \mapsto \mathbb{R}_+$ a metric distance between species of robots. More specifically, δ represents the differences between the abilities of various species *in the context of performing a particular task*. For example, if we have three robots, one belonging to species s_5 ($\pi(s_5) = \{C\}$) and two belonging to species s_8 ($\pi(s_8) = \{C, M, Y\}$) and we have to paint

only cyan, then the distance between agents should be zero, since all of them can perform the same task. However, if the task were to paint a combination of yellow and magenta, then the species s_5 could not contribute to that task and, therefore, $\delta > 0$.

Similar to [204], we formalize this idea by introducing a task space, represented by the tuple (T, γ) where T denotes the set of tasks, and $\gamma : T \mapsto \mathbb{R}_+$ represents an associated weight function. In this chapter, the set of tasks T simply correspond to the different colors specified by the user, as shown in Table 5.1. Consequently, a task $t_\beta^j \in T$ corresponds to the component j , $j \in \{C, M, Y\}$, of color input $\beta \in \mathcal{C}$. The corresponding weight functions for the tasks are calculated as,

$$\gamma(t_\beta^j) = \frac{\beta_j}{\sum_{\tilde{\beta} \in \mathcal{C}} \sum_{k \in \mathcal{P}} \tilde{\beta}_k}.$$

With this task-space, the task-map, $\omega : \mathcal{S} \mapsto 2^T$, as defined in [204], directly relates the different robot species with the CMY colors, i.e., if the color equipment of species ι is denoted as $\pi(\iota)$, then it can execute tasks t_β^j if $j \in \pi(\iota)$.

Having defined the task-space, (T, γ) , and the task-map, ω , the distance between two agents i and j can be calculated as in [204],

$$\delta(T, \gamma, \omega)(\iota, \kappa) = \frac{\sum_{t \in (\omega(\iota) \cup \omega(\kappa)) \setminus (\omega(\iota) \cap \omega(\kappa))} \gamma(t)}{\sum_{u \in (\omega(\iota) \cup \omega(\kappa))} \gamma(u)}.$$

This task-dependent distance metric between different robot species can then be used to compute the *disparity* as shown in (5.10).

Having completely characterized the disparity, $Q(s)$, and the complexity, $E(s)$, of an experimental setup under a specific painting task, one can compute the heterogeneity measure associated with them according to (5.9). To this end, the third column in Table 5.2 represents the heterogeneity measure of the different setups. The heterogeneity values have been computed for the sunset-painting task from Table 5.1, as well as for a generic

painting task that considers the whole 8-bit RGB color spectrum as objective colors to be painted by the team. This latter task is introduced in this analysis with the purpose of serving as a baseline to evaluate the comprehensiveness of the proposed sunset painting task. As it can be observed in Table 5.2, the heterogeneity values obtained for the sunset and the 8-bit RGB tasks are quite similar and the relative ordering of the setups with respect to the heterogeneity measure is the same, thus suggesting that the sunset task used in this chapter requires a diverse enough set of painting objectives for all the equipment setups proposed. Armed with this quantification of team heterogeneity, we now analyze how the spatial characteristics of the painting differ as the equipment configurations change.

5.4.1 Color Distance

We first analyze the complex interplay between motion trails and equipment setups by computing the spatial distance between the mean location of the desired input density function specified by the user, and the resulting manifestation of the color in the painting. To this end, we use the *color distance* metric introduced in [205] to characterize the distance from the color obtained in every pixel of the resulting painting to each of the input colors specified in Table 5.1.

Let $\rho(q)$ represent the 8-bit RGB vector value for a given pixel q in the painting. Then, the color distance between two pixels q_i and q_j is given as,

$$d_p(q_i, q_j) = 1 - \left[1 - \frac{2}{\pi} \cos^{-1} \left(\frac{\rho(q_i) \cdot \rho(q_j)}{\|\rho(q_i)\| \|\rho(q_j)\|} \right) \right] \left[1 - \frac{\|\rho(q_i) - \rho(q_j)\|}{\sqrt{3 \cdot 255^2}} \right] \quad (5.11)$$

Using (5.11), we can compute the distance from the color of each pixel to each of the input colors specified by the user (given in this chapter by Table 5.1). For a given pixel in the painting q and input color β , these distances can be interpreted as a color-distance

density function over the domain, denoted as φ

$$\varphi(q, \beta) = \exp \left(-\frac{d_p(q, \beta)}{\varsigma^2} \right),$$

where, with an abuse of notation, $d_p(q, \beta)$ represents the color distance between the color β and the color at pixel q . For the experiments conducted in this chapter, ς^2 was chosen to be 0.1.

Since we are interested in understanding the spatial characteristics of colors in the painting, we compute the center of mass of a particular color β in the painting,

$$C_\beta = \frac{\int_{\mathcal{D}} q \varphi(q, \beta) dq}{\int_{\mathcal{D}} \varphi(q, \beta) dq}. \quad (5.12)$$

The covariance ellipse for the color β at a pixel q is given as,

$$V_\beta(q) = \sqrt{(\varphi(q))}(q - C_\beta). \quad (5.13)$$

For each of the input colors, Fig. 5.5 illustrates the extent to which the color center of masses (computed by (5.12) and depicted by the square filled by the corresponding color) are different from the mean locations of the input density functions (depicted by the circle). For all the painting equipment setups in Fig. 5.5, as the heterogeneity of the team increases, the mean of the input density function for each color and the resulting center of mass become progressively more distant. This phenomenon is illustrated in Fig. 5.6, where the mean distance between the input density and the resulting color center of mass is plotted as a function of the heterogeneity of the equipment of the robots. For a given painting P , this distance is computed as,

$$d_c(P) = \frac{\sum_{\beta \in \mathcal{C}} \|\mu_\beta - C_\beta\|}{|\mathcal{C}|}, \quad (5.14)$$

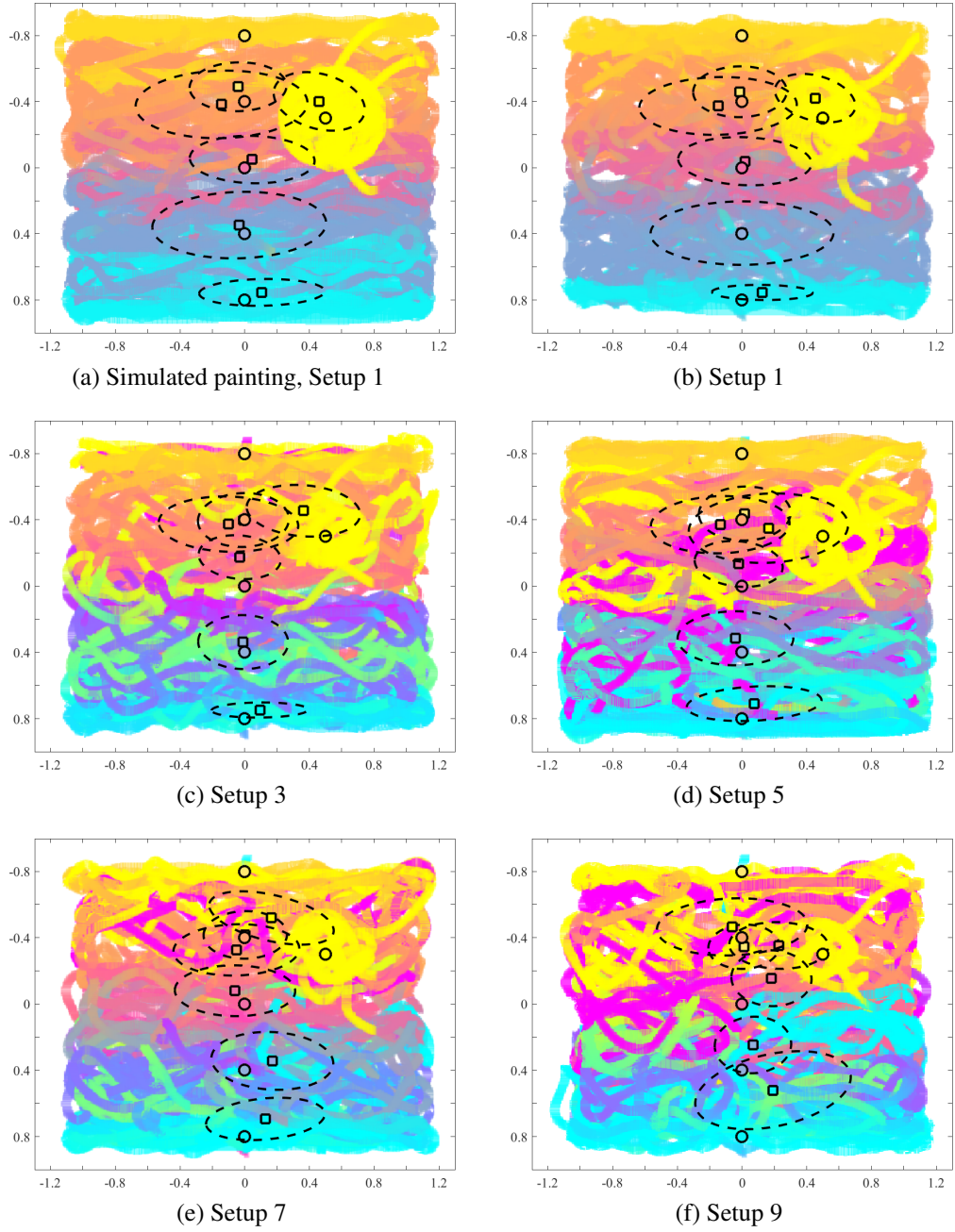


Figure 5.5: For each input color (given in Table 5.1): mean of the input density function (circle), and center of mass of the resulting color according to (5.12). The dotted lines depict the covariance ellipse according to (5.13). As seen the heterogeneity of the multi-robot team (as defined in (5.9)) impacts how far the colors are painted from the location of the input, as given by the user.

where \mathcal{C} represents the set of input colors, and μ_β represents the mean of the input density function for color β . As seen, with increasing heterogeneity, the mean distance increases

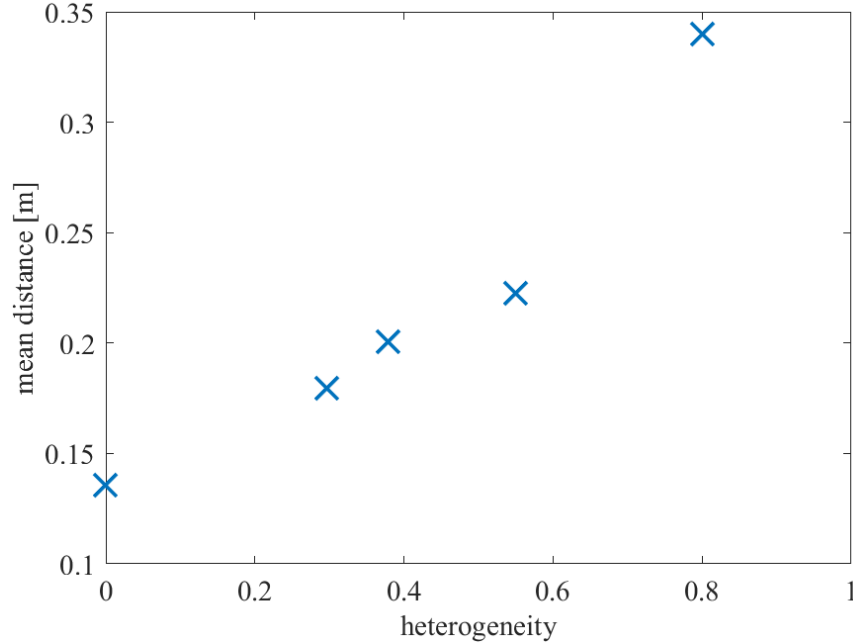


Figure 5.6: Average distance from mean density input to the resulting center of mass over the input colors of the painting as a function of the heterogeneity among the robots (as defined in (5.9)). As seen, with increasing sparsity of painting equipment on the robots (signified by increasing heterogeneity), the mean distance increases, indicating that colors get manifested farther away from where the user specifies them.

because lesser painting capabilities on the robots do not allow them to exactly reproduce the input color distributions. However, even with highly heterogeneous setups, such as Setups 7 or 9, the multi-robot team is still able to preserve highly distinguishable color distributions throughout the canvas, which suggests that the coverage control paradigm for multi-robot painting is quite robust to highly heterogeneous robot teams and resource deprivation.

5.4.2 Chromospectroscopy

The second method we utilize to quantify the differences among the paintings as a function of the heterogeneity in the robot team is using *chromospectroscopy* [206], which analyzes the frequency of occurrence of a particular color over the canvas. To this end, the painting is divided according to the sectors described in Table 5.3, which are closely related to the areas of high incidence of the objective color densities in Table 5.1. A histogram represent-

Table 5.3: Color sectors throughout the painting used for the chromospectroscopy analysis, according to the density parameters specified in Table 5.1.

Sector ID	Objective Color	$x_{min}[\text{m}]$	$x_{max}[\text{m}]$	$y_{min}[\text{m}]$	$y_{max}[\text{m}]$
1	Yellow	-1.2	1.2	1	0.6
2	Orange	-1.2	1.2	0.6	0.2
3	Pink	-1.2	1.2	0.2	0.2
4	Blue	-1.2	1.2	-0.2	-0.6
5	Cyan	-1.2	1.2	-0.6	-1
6	Yellow Sun	0.3	0.7	0.5	0.1

ing the frequency of occurrence of each input color per sector is described in Fig. 5.7. For the purposes of the chromospectroscopy analysis, the 8-bit RGB color map of the canvas is converted into a 5-bit RGB color map, by reducing the resolution of the color map and grouping very similar colors together, i.e., for an input color $\beta \in [0, 255]^3$, the modified color for the chromospectroscopy analysis in Fig. 5.7 is computed as $\bar{\beta} = \frac{\beta}{b}$, with $b = 2^3$.

As seen in Fig. 5.7, the heterogeneity of the robot team significantly affects the resulting color distribution within each sector. More specifically, as the heterogeneity of the team increases, thus depriving the team of painting capabilities, the canvas presents more outlier colors which are present outside the corresponding target sectors. This is apparent in highly heterogeneous teams (Setup 9), where magenta-like colors appear in the top-most sector and cyan appears in the central sector. The three central sectors show a high occurrence of non-target colors. For slightly lesser heterogeneous teams, while the occurring colors often do not correspond with the target colors in the sectors—e.g. green in Sector 4 of Setup 3—, the colors seem consistent in their presence and correspond to limitations on the equipment of the robots: in Setup 3, all robots are equipped with only two colors, thus no robot is able to exactly replicate any target color with 3 CMY components by itself. In the case of teams with low heterogeneity, e.g., Setup 1 and Setup 3, resulting colors are mostly consistent with the input target colors. The presence of some colors which do not match the input

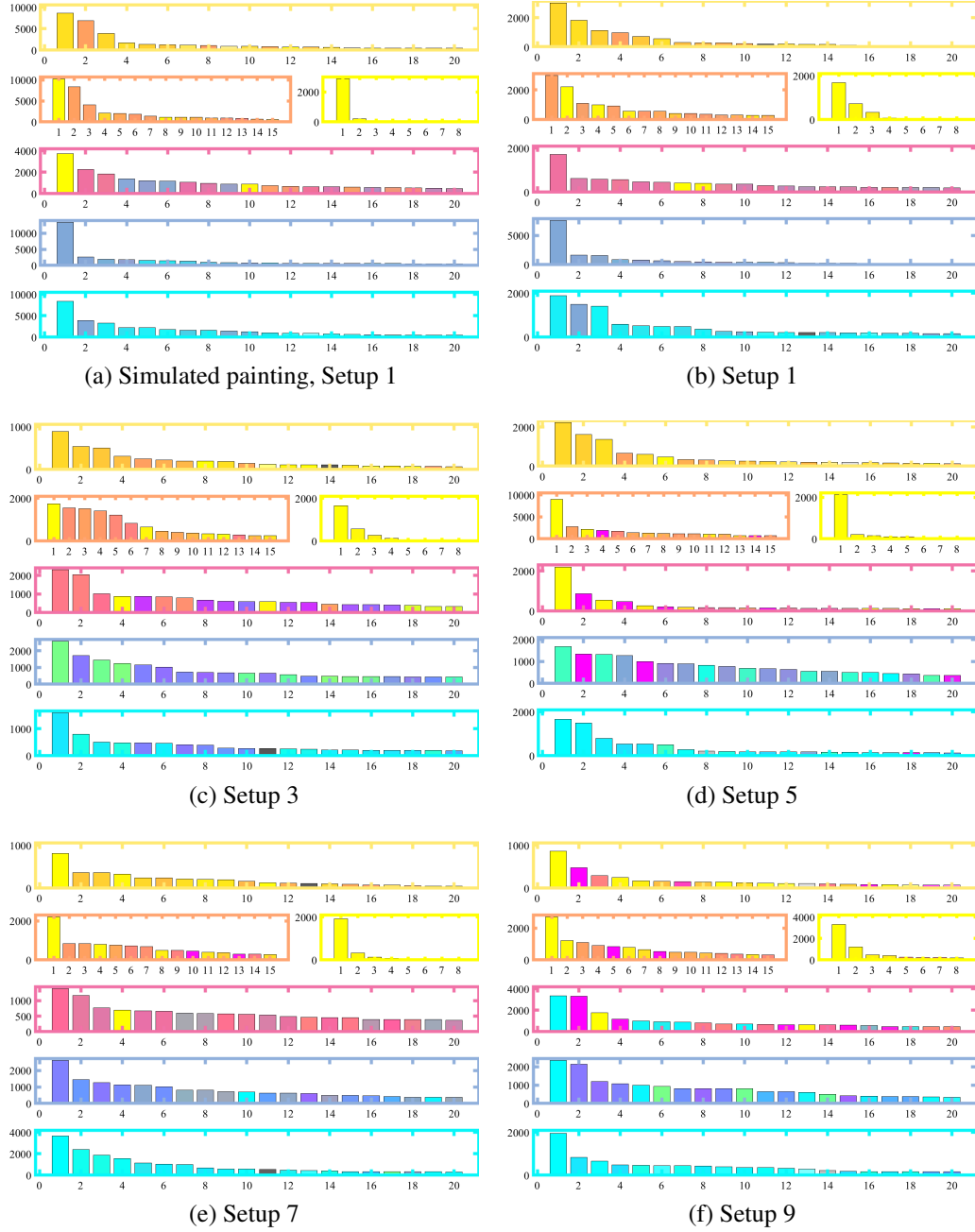


Figure 5.7: Chromospectroscopy by sectors on the canvas (as indicated in Table 5.3) for each equipment configuration (as specified in Table 5.2). With increasing heterogeneity, and consequently, sparser painting capabilities of the robots, colors distinctly different from the target colors begin to appear in each sector. For teams with lower heterogeneity (Setups 1-3), anomalous colors in the chromospectroscopy typically appear from neighboring sectors only.

corresponds to colors belonging to the neighboring sectors. Some specific examples of this include: (i) Setup 1: the presence of yellow in Sector 3, orange in Sector 2, and Blue in

Sector 5, (ii) Setup 3: the presence of orange in Sector 1, and blue in Sector 5, (iii) Setup 5: magenta and cyan-like colors in Sector 4.

Indeed, as one could expect, the chromospectroscopy reveals that color distributions become less precise as the differences in the painting capabilities of the robots become more acute—observable as distinct paint streaks in Fig. 5.4 which stand out from the surrounding colors. Nevertheless, the distribution of colors on each sector still matches the color density inputs even for the case of highly heterogeneous teams, which suggests that the multi-robot painting paradigm presented in this chapter is robust to limited painting capabilities on the multi-robot team due to restrictions on the available paints, payload limitations on the robotic platforms, or even the inherent resource depletion that may arise from the painting activity.

5.4.3 Statistical Results

In order to understand if the statistics reported above remain consistent for multiple paintings generated by the robotic painting system, we ran 10 different experiments for each of the 9 equipment configurations described in Table 5.2. Figure 5.8 shows the average of the paintings generated for each equipment, along with the color density averages, computed using (5.12). Although averaging the 10 rounds seems to dampen the presence of outliers, we can still observe how the distance between the objective color (represented by a circle) and the resulting color distribution (square) generally increases as the team becomes more heterogeneous. Furthermore, if we observe the color gradient along the vertical axis of the painting, the blending of the colors becomes more uneven as the heterogeneity of the team increases. This phenomenon becomes quite apparent if we compare the top row of Fig. 5.8—(a) to (c)—to the bottom row—(g) to (i).

Quantitatively, this distancing between objective and obtained color density distribution is summarized in Fig. 5.9, which shows the mean distance between the input density and the resulting colors. Analogously to the analysis in Fig. 5.6, which contained data for one

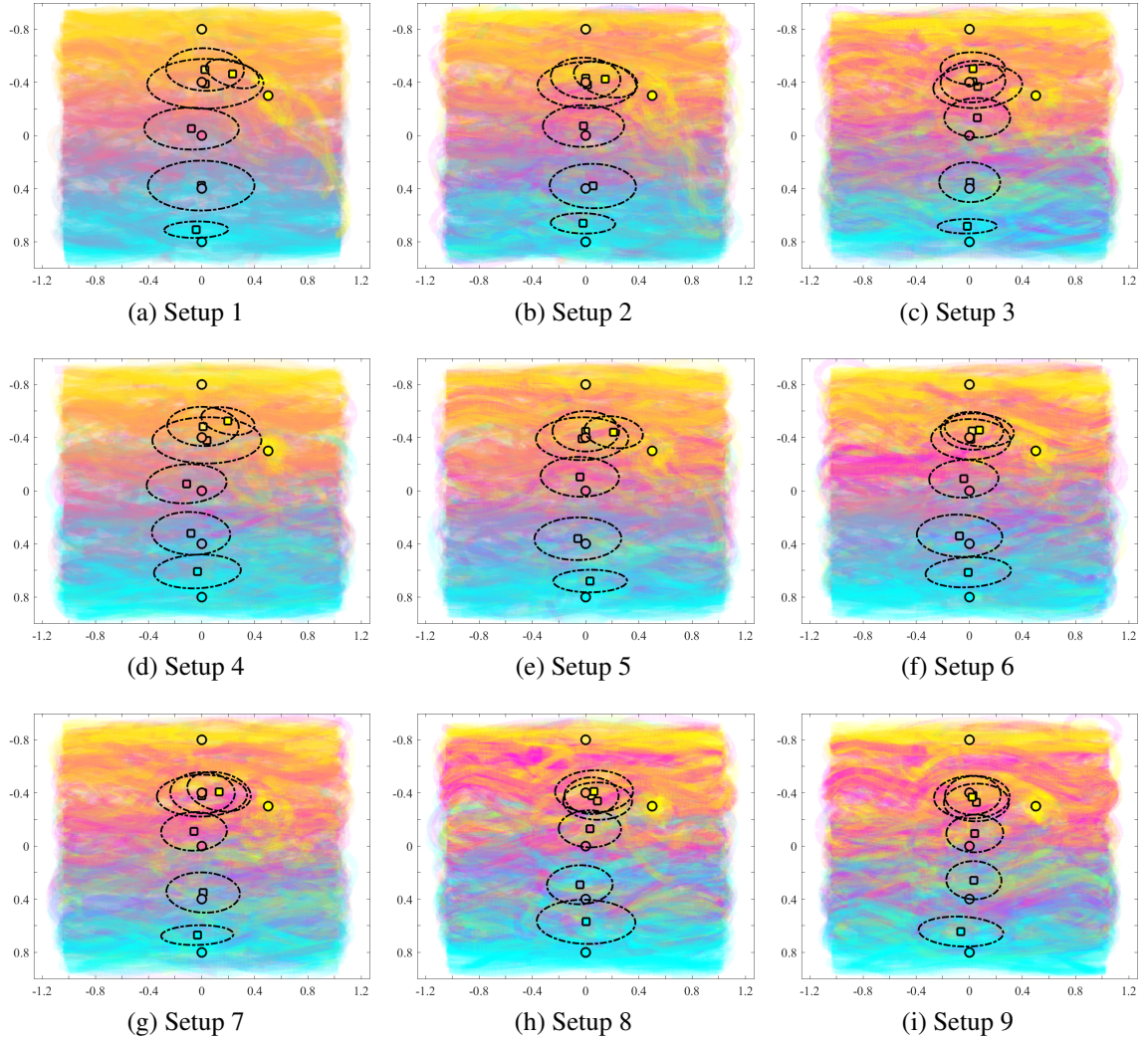


Figure 5.8: Averaged paintings over 10 trials. Mean of the input densities (circle), center of mass of the resulting colors according to φ from (5.12) (square), and covariance ellipse (dotted lines). The heterogeneity in the painting equipment of the robots has a significant impact on the nature of the paintings.

run in the Robotarium for five out of the nine setups, the average distances shown in Fig. 5.9 show that the resulting color distributions tend to deviate from the objective ones as the team becomes more heterogeneous.

The results observed in this statistical analysis, thus, support the observations carried out in the analysis of the paintings obtained in the Robotarium. Therefore, the characterization of the painting outcome with respect to the resources of the team seems consistent throughout different runs and independent of the initial spatial conditions of the team.

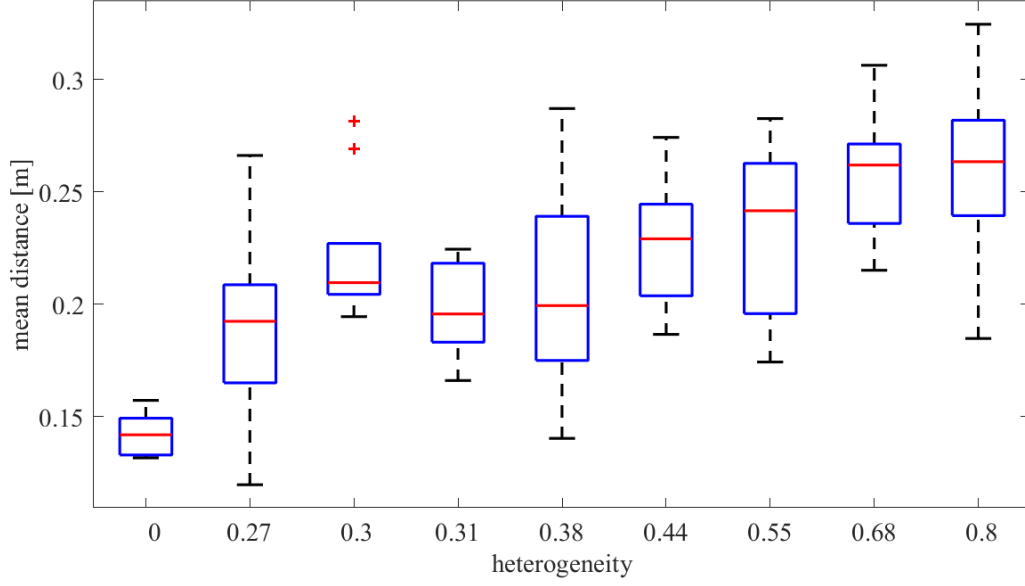


Figure 5.9: Box plots of the average distance between mean density input to resulting center of mass as computed in (5.14) for the 9 different equipment configurations. The results are presented for 10 different experiments conducted for each equipment. As seen, the average distance increases with increasing heterogeneity among the robots' painting equipment.

5.5 Conclusions

This chapter presents a robotic swarm painting system based on mobile robots leaving trails of paint as they move where a human user can influence the outcome of the painting by specifying desired color densities over the canvas. The interaction between the human artist and the painting is enabled by means of a heterogeneous coverage paradigm where the robots distribute themselves over the domain according to the desired color outcomes and their painting capabilities, which may be limited. A color mixing strategy is proposed to allow each robot to adapt the color of its trail according to the color objectives specified by the user, within the painting capabilities of each robot. The proposed multi-robot painting system is evaluated experimentally to assess how the proposed color mixing strategy and the color equipments of the robots affect the resulting painted canvas. A series of experiments are run for a set of objective density functions, where the painting capabilities of the team are varied with the objective of studying how varying the painting equipment

among the robots in the team affects the painting outcome. Analysis of the resulting paintings suggests that, while higher heterogeneity results in bigger deviations with respect to the user-specified density functions—as compared to homogeneous, i.e. fully equipped, teams—the paintings produced by the control strategy in this chapter still achieve a distribution of color over the canvas that closely resembles the input even when the team has limited resources.

CHAPTER 6

EMOTIONALLY EXPRESSIVE ROBOTIC SWARMS

Robots have progressively migrated from purely industrial environments to more social settings where they interact with humans in quotidian activities such as education [207], companionship [208, 209], or health care and therapy [210, 211]. In these scenarios, on top of performing tasks related to the specific application, there may be a need for the robots to effectively interact with people in an entertaining, engaging, or anthropomorphic manner [144].

The need for enticing interactions between social robots and humans becomes especially pronounced in artistic applications. Robots have been progressively intertwined with different forms of artistic expression, where they are used, among others, to interactively create music [92], dance [93, 94, 95, 97], act in plays [99, 100, 101], support performances [5], or be the object of art exhibits by themselves [106, 108, 109]. As in the traditional expressions of these performing arts, where human artists instill expressive and emotional content [142, 143], robots are required to convey artistic expression and emotion through their actions.

While expressive interactions have been extensively studied in the context of performing arts, the focus has been primarily on anthropomorphic robots, especially humanoids [99, 145, 146]. However, for faceless robots or robots with limited degrees of freedom for which mimicking human movement is not an option, creating expressive behaviors can pose increased difficulty [27, 147, 148]. We are interested in exploring the expressive capabilities of a swarm of miniature mobile robots, for which the study of expressive interactions is sparse [114, 115, 116]. This can be contrasted with more anthropomorphic robots, for which there is already a preconceived understanding of emotive expressiveness. This choice is driven in part by the increased prevalence of multi-robot applications and

the envisioned, resulting large-scale human-robot teams [24, 212, 213]; and in part by the expressive possibilities of the swarm as a collective in contrast to the robots as individuals. While using teams of mobile robots to create artistic effects in performances is not something new [5, 111], our aim is to provide a framework to use these types of robotic teams in performances without the need for a choreographer to specify the parameters of the robots' movements, as in [27].

Social psychology has extensively studied which motion and shape descriptors are associated with different fundamental emotions, e.g. [169, 170, 173, 179, 214]. In this chapter, we study how such attributes can be incorporated into the movements of a swarm of mobile robots to represent emotions. In particular, a series of swarm behaviors associated with the so-called fundamental emotions are designed and evaluated in a user study in order to determine if a human can identify the different fundamental emotions by observing the swarm aggregate behavior and movement of the individual robots [113, 215].

The remainder of the chapter is organized as follows: In Section 6.1, we outline the motion and shape characteristics psychologically linked to the different fundamental emotions. The behaviors included in the user study, implemented on the swarm according to the features described in the social psychology literature, are characterized in Section 6.2. The procedure and results of the study conducted with human subjects are presented in Section 6.3, along with the discussion. An implementation of the proposed swarm behaviors on a real robotic platform is presented in Section 6.4. Section 6.5 summarizes the main takeaways on this study on expressive swarm behaviors. To conclude the chapter, Appendices 6.A and 6.B contain detailed explanations for the implementation of the different behaviors and individual robot control.

6.1 Emotionally Expressive Movement

For robotic swarms to participate in artistic expositions and effectively convey emotional content, the swarm's behavior when depicting a particular emotion should be recognizable

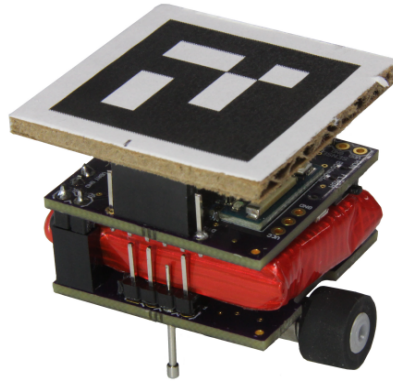


Figure 6.1: The GRITSBot, a 3cmx3cm miniature mobile differential drive robot. The robotic swarm considered in this study is composed of 15 GRITSBots. The top view of these robots is used in the simulations shown to the study participants when evaluating the different swarm behaviors.

by the audience, thus producing the effect intended by the artist. However, the lack of anthropomorphism in a robotic swarm can pose a challenge when creating expressive motions for human spectators. In this section, we present a summary of motion and shape features that have been linked to different emotions in the social psychology literature, which will serve as inspiration to create expressive behaviors for swarms of mobile robots.

In this study, we focus on the so-called *fundamental emotions* [214, 216]—i.e. happiness, sadness, anger, fear, surprise and disgust—to produce a tractable set of emotion behaviors to be executed by the robotic swarm. An emotion is considered *fundamental* or *basic* if it is inherent to human mentality and adaptive behavior, and remains recognizable across cultures [217]. In addition, fundamental emotions provide a basis for a wider range of human emotions, which appear at the intersection of the basic emotions with varying intensities [218].

The robotic system considered for this study is a swarm of miniature differential-drive robots, the GRITSBots [189]. As shown in Fig. 6.1, the GRITSBots are faceless robots that do not possess any anthropomorphic features. While Laban Movement Analysis [149] has been used in robotic systems to convey emotional content through acceleration pat-

terns [150, 151, 152, 154], when considering large robot swarms, the individual robots may be limited in size and actuation capabilities, thereby restricting their ability to use acceleration as their expressive means. For this reason, along with the characteristic non-anthropomorphism of a swarm and the possibilities of its collective behavior, we draw inspiration from abstract shape and motion descriptors associated with different fundamental emotions [168] to create different swarm behaviors.

Table 6.1 presents a summary of the shape, movement and size attributes of abstract objects associated with some fundamental emotions and emotion valences. Among these characterizations, those related to shape and size represent the impact of the form of an object on its emotion attribution. In particular, angular shape contours are typically associated with emotions with a negative valence and high arousal¹—i.e. anger, fear and disgust—while round shape contours are linked to positive emotions (happiness and surprise) or emotions with very low activation levels (sadness) [175, 179]. The size of a particular object also affects its emotional perception, with bigger objects being typically associated with larger emotion arousal (e.g. surprise) and smaller sizes with emotions with low activation [168]. Table 6.1 also presents how the features of different movement patterns are related to perceived emotions [170]. Analogously to shape contours, smoothness of movement is related to the pleasantness of the motion, thus evoking emotions with positive valence [169], while an angular movement trace—interpreted as the trajectory taken by the robot over time—is linked to negative emotions [170]. Speed of movement also influences the emotion attribution, with higher peak velocities being identified with angry states [170] and slower movements that integrate into smaller trajectories over time being connected to fearful and sad emotional states [170, 173].

While the summary of features related to emotions in Table 6.1 provides a good starting

¹In this context, the term *valence* designates the intrinsic attractiveness (positive valence) or aversiveness (negative valence) of an event, object, or situation [166]. The valence of an emotion thus characterizes its positive or negative connotation. Among the fundamental emotions, happiness and surprise have positive valence, while the remaining four—sadness, fear, disgust and anger—are classified under negative valence [167]. On the other hand, the term *arousal* refers the activation or deactivation associated with an emotion.

Table 6.1: Movement and shape attributes associated with different emotions and emotion valences.

Shape Features		Size Features	Movement Features
Emotion	Happiness	roundness, curvilinearity [179]	smoothness [169]
	Surprise	roundness [179]	very big [168]
	Sadness	roundness [179]	small [168]
	Anger		small, slow [170, 173]
	Fear	downward pointing triangles [175]	large, fast, angular [170] small, slow [170, 173]
Valence	Positive	roundness [175, 179]	rounded movement trace [175, 179]
	Negative	angularity [175, 179]	angular movement trace [175, 179]

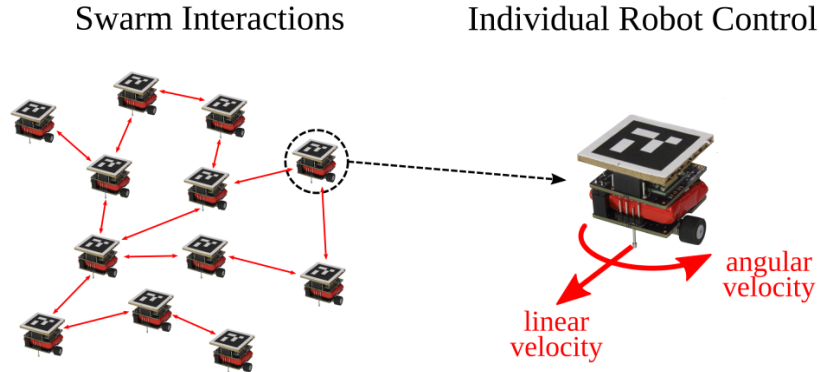


Figure 6.2: The behavior of a robotic swarm depends on which interactions are considered between the robots, which information is exchanged through those interactions, and how each robot acts on such information. Different interaction schemes and control laws produce distinct swarm behaviors.

point for generating swarm behaviors for most fundamental emotions, literature on motion characterizations of *disgust* is scarce. In order to get some intuition about which traits the swarm behavior should portray when embodying this emotion, we direct our attention towards characterizations associated with emotion valence. The shape and motion characterizations of positive and negative emotion valences in the lower part of Table 6.1 serve as a basis to design the swarm behavior associated with disgust.

The behavior of a robotic swarm depends on how the interactions are established between members of the swarm and what control commands are executed by the individuals based on the information exchanged in those interactions, as illustrated in Fig. 6.2. While the GRITSBots as individuals cannot change their shape, the collective behavior of the swarm may embody the *shape* and *size* attributes included in Table 6.1. On the other hand, the *movement* features in Table 6.1 can be depicted through the movement trace that each individual robot executes as it progresses towards the collective shape. In the next section, we describe how all these attributes are implemented in the controller of the robots to produce the behaviors that embody the different fundamental emotions.

6.2 Swarm Behavior Design

For our swarm of robots to be expressive, we need to decide which interactions a robot should establish with the robots in its vicinity and its environment, and which control law the robot should execute with the information obtained through those interactions to produce an appropriate swarm behavior. In this work, we draw inspiration from standard algorithms for multi-robot teams, namely cyclic pursuit [219, 220, 221] and coverage control [6, 8], to design the interactions and the control laws for the swarm. This section describes how the shape and movement features described in Section 6.1 are incorporated into the control laws of a swarm of 15 GRITSBots in order to create expressive behaviors.

6.2.1 Collective Behavior

The attributes presented in Section 6.1 characterize how the motion and shape of an abstract object can convey emotion. Here we treat the GRITSBots as objects capable of reconfiguring themselves on a stage in order to generate an expressive behavior.

Among the attributes presented in Table 6.1, it seems natural for those related to *shape* and *size* to be depicted by the collective behavior of the swarm, given that the individual robots can move within the planar environment but cannot change their individual shape. To this end, the feature of *roundness* is incorporated into the behaviors of happiness, surprise and sadness. Those behaviors are thus based on the robots following some kind of circular contour, as illustrated in Figs. 6.3, 6.4 and 6.5, respectively. In the case of the happiness behavior, a sinusoid is superimposed to the base shape of a circle, producing ripples on the circle contour to embody the *curvilinearity* feature; and the corresponding size attribute—*big*—is incorporated through the circle dimensions with respect to the domain.

As for the surprise emotion, the *very big* size attribute was included in the behavior by making the radius of the circle grow with time, thus producing a sensation of increasing size. Finally, the circular path dimension was reduced (*small* attribute) in the case of the

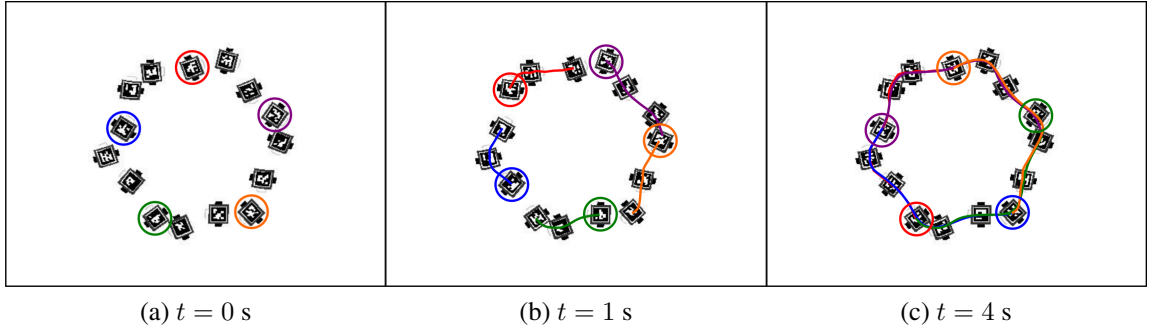


Figure 6.3: Sequence of snapshots of the *happiness* behavior. Each robot follows a point that travels along a circular sinusoid, visually producing a circular shape with small ripples. The trajectories of five robots have been plotted using solid lines. See the full video at https://youtu.be/q_FenI1DdRY.

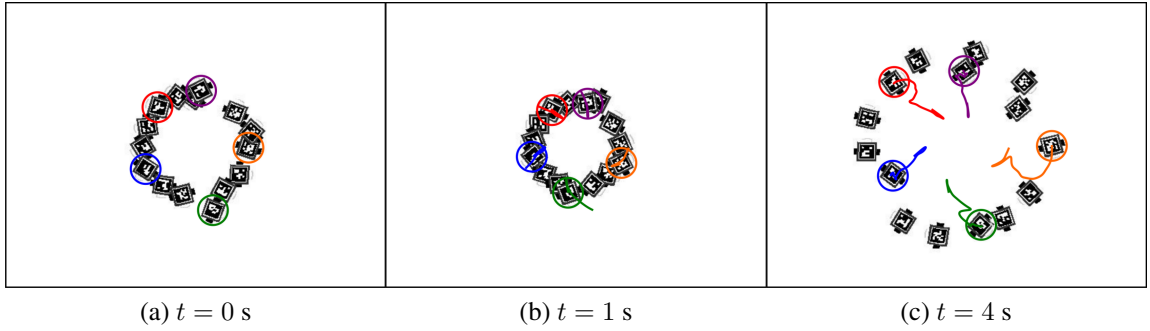


Figure 6.4: Sequence of snapshots of the *surprise* behavior. The robots move along a circle of expanding radius, thus creating a spiral effect. The trajectories of five robots have been plotted using solid lines. See the full video at <https://youtu.be/VYIJ5hBeOIU>.

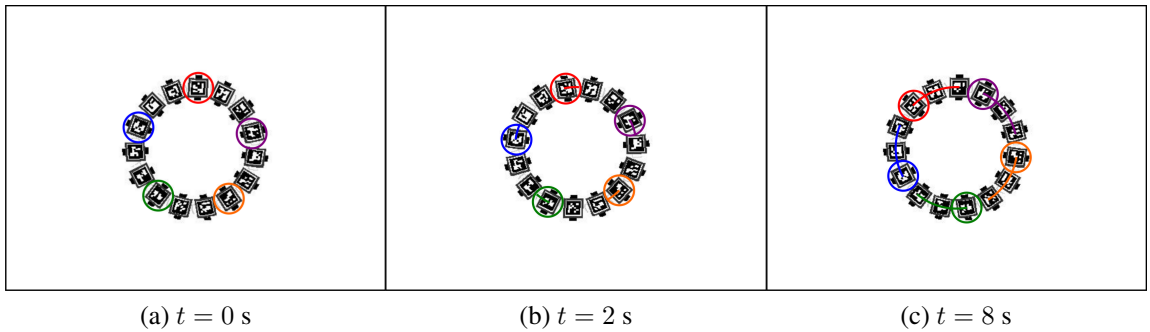


Figure 6.5: Sequence of snapshots of the *sadness* behavior. The robots move along a small circle at a low speed. The trajectories of five robots have been plotted using solid lines. After 8 seconds, each robot has only displaced approximately an eighth of the circumference. See the full video at <https://youtu.be/rfHZcFnRFg8>.

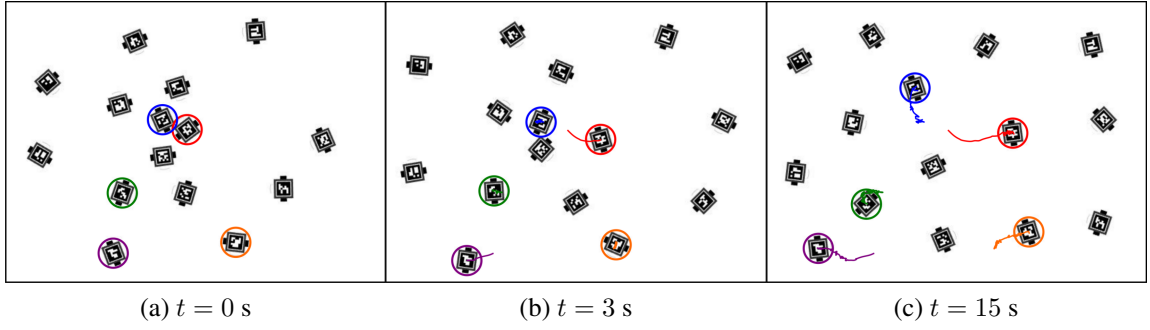


Figure 6.6: Sequence of snapshots of the *fear* behavior. The robots spread out uniformly over the domain. As it can be observed from the trajectories, they displace slowly with a non-smooth, angular movement trace. See the full video at <https://youtu.be/jz-5INUd8wc>.

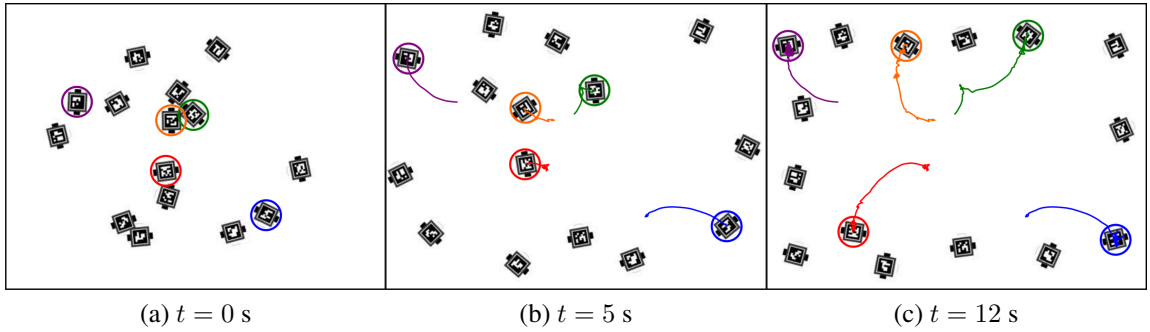


Figure 6.7: Sequence of snapshots of the *disgust* behavior. The robots spread out slowly towards the boundaries of the domain, with a trajectory with a non-smooth, angular trace. See the full video at <https://youtu.be/EprfuCsuuRM>.

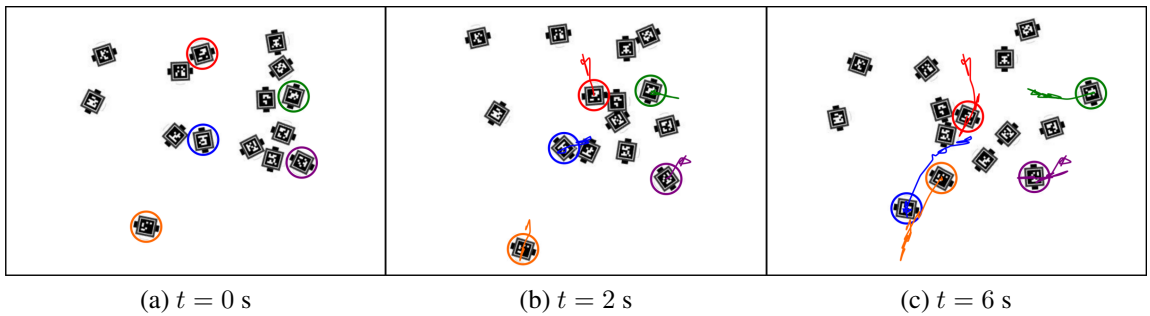


Figure 6.8: Sequence of snapshots of the *anger* behavior. The density function is defined as a Gaussian at the center of the domain, causing the robots to concentrate around this area. However, the fact that the robots move with high speed causes overshoots in their positions, thus producing a significantly angular movement trace. See the full video at <https://youtu.be/kAGBrMkOtyY>.

sadness behavior, incorporating also the *slowness* attribute by making the robots follow the contour at a very low speed.

The scarcity of shape characterizations for the other three emotions—fear, disgust and anger—motivates a different approach for the design of the collective behavior of the swarm. For these emotions, we choose to specify which areas of the domain the robots should concentrate around. We do so by defining a density function, ϕ , that characterizes the areas of the domain where we want the robots to group. In all three behaviors, the robots are initially distributed at random positions within the domain to then spread according to the particular density function selected. In the case of fear, the density function is uniform across the domain, so that it makes the robots scatter as far as possible from their neighbors, as shown in Fig. 6.6. For the disgust motion, Fig. 6.7, the density is chosen to be high around the boundaries, making the robots move from the center towards the exterior of the domain—the stage—, giving the sensation of animosity between robots. Finally, in order to show anger, the robots are made to stay closer to the center of the domain. This strategy, combined with the individual robot control that will be explained in Section 6.2.2, is intended to give the sensation of a heated environment, a riot.

The control laws needed to achieve these behaviors are explained in detail in Appendix 6.A. In each of those laws, a robot in the swarm is treated as a point that can move omnidirectionally. However, the GRITSBots (see Fig. 6.1) are differential drive robots and, thus, are unable to move perpendicularly to the direction of their wheels. This movement restriction is used to our advantage in the individual control strategies described in Section 6.2.2, where we exploit the limitations on the planar movement of the differential drive robots to implement the *movement features* in Table 6.1.

6.2.2 Individual Robot Control

The swarm behavior strategies and corresponding control laws introduced in Section 6.2.1 and detailed in Appendix 6.A treat each robot in the swarm as if it could move omnidirec-

tionally. That is, if we denote by $p \in \mathbb{R}^2$ the position of a robot, then its movement could be expressed using *single integrator dynamics*,

$$\dot{p} = u, \quad (6.1)$$

with $u \in \mathbb{R}^2$ denoting the control action given by the chosen behavior. However, the differential drive configuration of the GRITSBot implies that it cannot execute single integrator dynamics. Instead, the motion of a differential drive robot is described by the so-called *unicycle dynamics*,

$$\dot{x} = v \cos \theta, \quad \dot{y} = v \sin \theta, \quad \dot{\theta} = \omega,$$

with $p = (x, y)^T$ being the robot's Cartesian position and θ its orientation in the plane. The control inputs, v and ω , correspond to the linear and angular velocities of the robot, respectively, as shown in Fig. 6.2.

In order to convert the input u in (6.1) into the executable control commands in (6.2.2), we use the near-identity diffeomorphism in [200]. The details of this transformation are described in detail in Appendix 6.B. Using this transformation between the single integrator and the unicycle dynamics, we get to tune two scalar parameters, l and K , that regulate how *smooth* the movement trace of each robot is and how *fast* it travels when executing a certain control input, respectively. Figure 6.9 illustrates the differences between directly executing the single integrator dynamics in (6.1), and performing two different diffeomorphisms on the single integrator control value, u . We can observe how choosing a small value for the diffeomorphism parameter l results in an angular movement trace, while a smooth trajectory is observed when selecting a bigger value for this parameter.

Given the ability to regulate the angularity and the speed of the movement trace of a robot, we are in a position to implement the movement features included in Table 6.1. The *smoothness* feature of the happiness emotion is translated into a smooth and fast individual control. Analogous diffeomorphism parameters are chosen to show surprise, given the

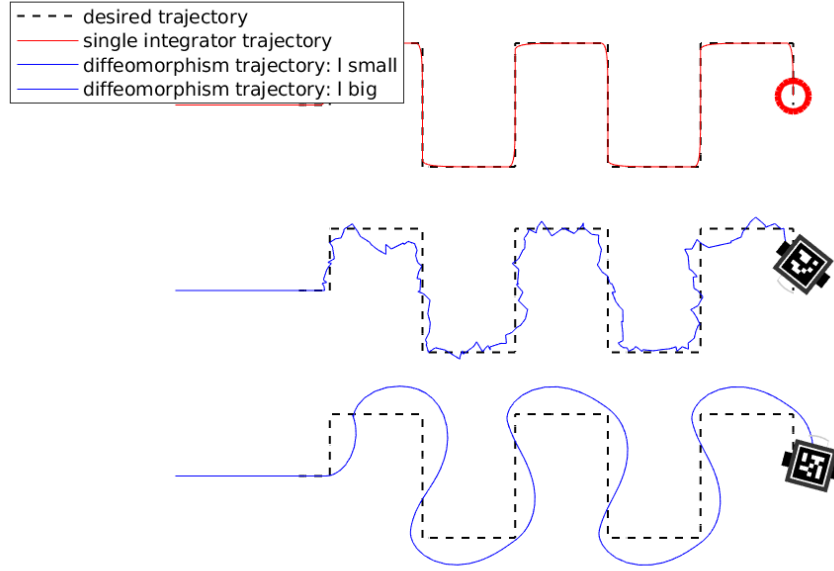


Figure 6.9: Effect of the diffeomorphism parameter, l , on the movement trace of an individual robot. In all cases, the controller is following a particle that moves along the black dashed line—the desired trajectory. The top figure illustrates how an agent capable of executing the single integrator dynamics in 6.1 follows closely the desired trajectory. The other two trajectories, in blue, illustrate two different diffeomorphisms performed over the control action of the single integrator. In the middle, a small value of l results in an angular movement trace that follows quite closely the desired trajectory. In contrast, at the bottom, a large value of l results on a very smooth movement trace, at the expense of following more loosely the desired trajectory.

roundness and *very big size* attributes associated with this emotion. As for sadness, even though it is a negative emotion, we focus on its specific characterizations provided in Table 6.1 to characterize the motion as slow and smooth. We can observe how, indeed, the trajectories depicted in Figs. 6.3, 6.4 and 6.5 are smooth given the choice of a large l in the diffeomorphism. The speed of the robots is illustrated by the total distance covered in time: while significant distances are traveled within 4 seconds for the behaviors of happiness and surprise, the robots in the sadness behavior displace very little in 8 seconds.

Table 6.1 associates an *angular movement trace* with the emotions with negative valence. Consequently, a controller that produces an angular movement trace, corresponding to a small l in the diffeomorphism, is selected for the remaining emotions—fear, disgust

Table 6.2: Motion and shape attributes selected for the behaviors associated with the fundamental emotions.

Emotion	Swarm Behavior	Robot Control
Happiness	sinusoid over circle	fast, smooth
Surprise	expanding circle	fast, smooth
Sadness	small circle	very slow, smooth
Fear	uniform coverage	slow, angular
Disgust	coverage on boundaries	slow, angular
Anger	coverage on center	fast, angular

and anger. The *movement features* presented in Table 6.1 for anger and fear are translated into fast and slow control, respectively. Given the lack of characterization for the speed of disgust, we opt to implement a slow motion. We can observe how, for Figs. 6.6 to 6.8, the trajectory traces have sharp turns and angularities, specially in the case of the anger behavior, which is accentuated by the proportional gain corresponding to a large velocity.

The swarm behavior selected for each of the emotions according to the shape characterizations discussed in Section 6.2.1 and the diffeomorphism parameters in this section are summarized in Table 6.2.

6.3 User Study

The behaviors described in Section 6.2 were implemented in simulation on a team of 15 differential drive robots, producing a video for each of the emotions. Snapshots generated from each of the videos, along with the URL links, are included in Figs. 6.3 to 6.8.

6.3.1 Procedure

A user study was conducted to evaluate if the swarm interactions and individual robot control strategies selected in Section 6.2 produce expressive swarm behaviors that correspond to the fundamental emotions. The hypothesis to test was the following,

H1: Overall Classification. Participants will perform better than chance in identifying the fundamental emotion each swarm behavior is intended to represent.

A total of 45 subjects (32 males and 13 females) participated in the study, with 29 of them not having any academic or professional background in robotics. As for the age of the participants, the distribution was as follows: 31.1% between 18 and 24 years old, 60.0% between 25 and 34 years old, 6.7% between 35 and 44 years old, and 2.2% between 45 and 54 years old. After responding to the demographic questions, each subject was shown 6 videos, each of them corresponding to the behaviors designed for each of the fundamental emotions. The videos were shown sequentially, one behavior at a time, and in a random order. The human subjects were instructed to watch each video in full, after which they were presented with a multiple choice (single answer) question to select the emotion that *best described the movement of the robots in the video*, with the possible answers being the 6 fundamental emotions. The participants had no time limit when classifying the videos and were allowed to rewatch them as many times as desired. Furthermore, at any point, the participants were allowed to navigate to previous questions in the survey and modify their answers, if desired, before submitting the survey responses.

6.3.2 Results and Discussion

The responses of the survey were collected and summarized in Table 6.3. The columns are labeled *signaled emotion* and each of them contains the responses given to the video of the behavior designed for a fundamental emotion. In the confusion matrix in Table 6.3, the emotions are ordered counterclockwise from positive to negative valence according to the circumplex model in Fig. 6.10.

The diagonal terms of the confusion matrix, boldfaced in Table 6.3, correspond to the percentage of responses that identified the emotion in the video as the one intended by the authors. For all the diagonal values, the percentage is much higher than the one given by chance (16.67%), and in most cases—happiness, sadness, anger and surprise—this value

Table 6.3: Confusion matrix calculated with the survey responses.

	Signaled Emotion					
	Happiness	Surprise	Anger	Fear	Disgust	Sadness
Response(%)	Happiness	64.44	17.78	8.89	4.44	13.33
	Surprise	11.11	57.78	8.89	2.22	0.00
	Anger	8.89	0.00	55.56	13.33	4.44
	Fear	6.67	13.33	20.00	40.00	15.56
	Disgust	6.67	4.44	4.44	26.67	2.22
	Sadness	2.22	6.67	2.22	13.33	64.44

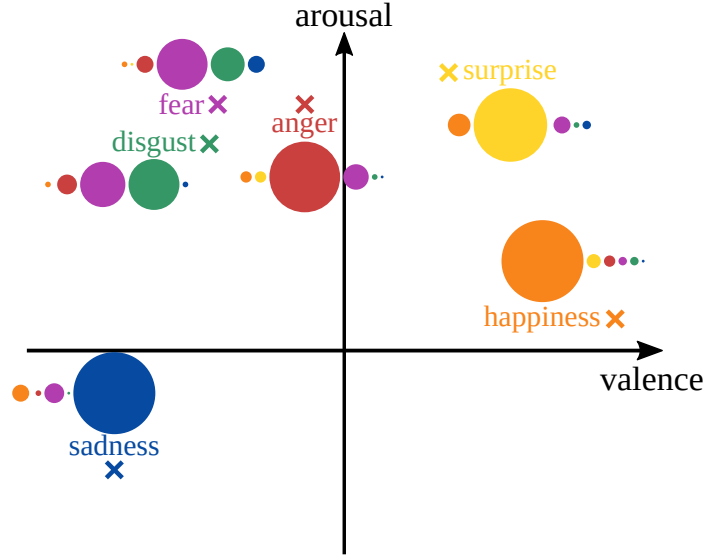


Figure 6.10: Representation of the survey responses in the valence-arousal plane. The location of each emotion is represented with a color-coded cross according to the circumplex model of affect [167, 222]. Next to each emotion, a sequence of color-coded circles represent how the human subjects identify each behavior, with the diameter of each circle being proportional to the amount of responses given to the corresponding emotion. We can observe how, in general, the majority of users labels the behavior according to the signaled emotion, with most variations occurring generally with those emotions closest in the plane. In the cases of fear and disgust, while the relative majority of subjects still labels their behaviors according to the hypothesis, we observe a significant amount of confusion among them, which may be due to the proximity of such emotions in terms of valence and arousal.

reaches the absolute majority (greater than 50%). In the cases of fear and disgust, while the relative majority of the responses identified the emotion according to our hypothesis (40% for both emotions), the values are lower than 50%. This can be potentially caused by the proximity of such emotions in terms of valence and arousal, as illustrated in Fig. 6.10. A Pearson’s chi-squared test goodness of fit was performed for the responses given to each swarm behavior, confirming that, at $p < 0.0001$, the frequency distributions for each emotion differ significantly with respect to a uniform distribution where all the emotions are considered equally likely to be chosen. Therefore, the assignment of an emotion to each of the videos was not made at random by the participants, but rather the movement and shape features incorporated in the swarm behaviors were effectively identified as the intended emotions.

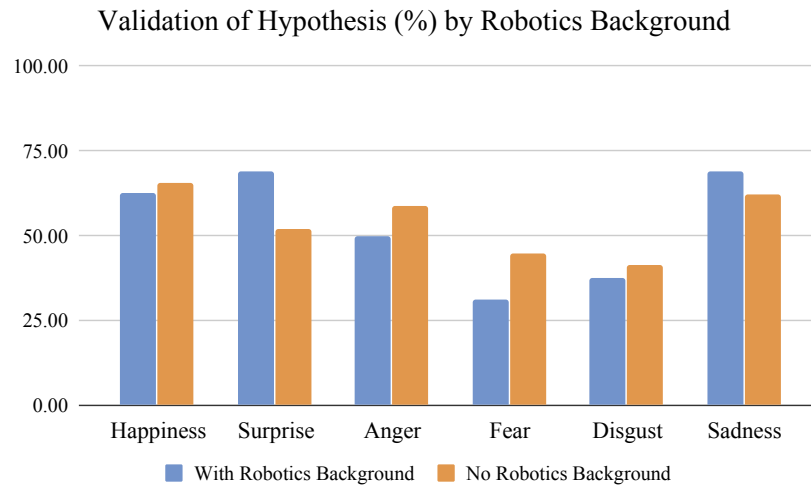


Figure 6.11: Percentage of subjects that identified each emotion in the video according to the hypothesis, classified according the robotics background of the subjects. There is no substantial difference between the responses given by the subjects that had experience studying or researching in robotics and those who did not.

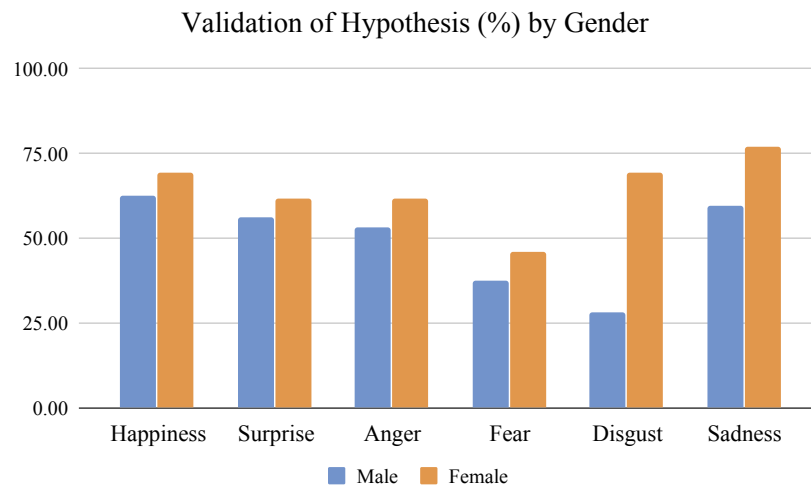


Figure 6.12: Percentage of subjects that successfully assigned the emotion to the corresponding video, according to the hypothesis, according to the gender of the participants. We can observe how the responses of the female subjects are consistently more aligned with the hypothesized behavior for each of the videos.

Based on the demographic data collected, the validation of hypothesis H1 was not affected significantly by the robotics background of the subjects. As shown in Fig. 6.11, for the 4 emotions for which the majority of the aggregate responses in Table 6.3 aligned with

the hypothesis—i.e. happiness, surprise, anger and sadness—all subjects, regardless of their background in robotics, identified the emotions according to the hypothesis in more than 50% of the cases. In fact, the Pearson’s chi-square test discards, at $p < 0.01$, the random assignment of emotions from the responses of participants both with and without robotics background. For the emotions of fear and disgust—those with the lowest accuracies in Table 6.3—the responses aligned better with hypothesis H1 for those subjects without a robotics background, for which the Pearson’s chi-square test discards the fitting of the data under a uniform distribution at a significance level of $p < 0.01$. While the subjects with robotics background still validated hypothesis H1 for these two emotions, the significance levels for the test are slightly higher ($p < 0.05$ for fear and $p < 0.1$ for disgust), possibly due to the fact that there were only 16 subjects with robotics background.

In contrast, when performing an analysis by gender, the validation of hypothesis H1 was consistently larger in the case of female subjects, as shown in Fig. 6.12. While the male participants still validated hypothesis H1 for all emotions, the accuracy was higher among the female subjects, being in 5 out of the 6 emotions higher than 50%. Only in the case of fear the accuracy for the female participants was slightly under the majority threshold (46.15%). As for the statistical significance of the responses, the frequency of distributions for each emotion differs from a uniform distribution at $p < 0.05$ for the male participants and at $p < 0.01$ for the female ones. Thus, while neither of the populations assign emotions to the behaviors at random, the motion and shape characterizations selected for the swarm behaviors were more clearly identified by the female participants in the study.

The methodology adopted in this work, however, poses certain limitations on the conclusiveness of the user study. Future inquiries on this matter may consider adopting a free-choice format to select the emotion that best describes the swarm behavior in each video, as opposed to the forced-choice question contemplated in this work, with the purpose of not constricting the participants’ answers to only the target emotions. Furthermore, the independence of the results obtained for each of the expressive behaviors could be boosted by

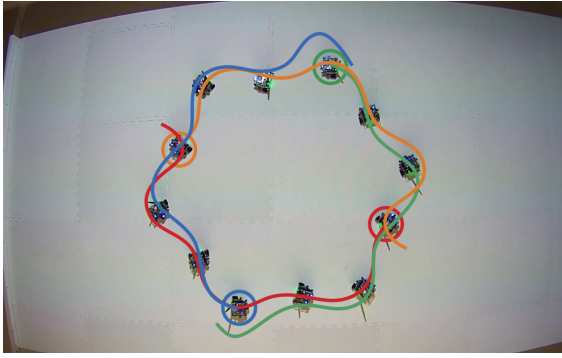
preventing participants from changing their previous answers, as being able to modify them may promote identification by comparison rather than independent association. Finally, the conclusiveness of a subsequent study could be strengthened with supplementary hypotheses involving the identification of other emotional traits in the behaviors (e.g. perceived valence or arousal), which would support the main hypotheses considered in this study.

In conclusion, the data collected in the user study supports hypothesis H1, thus confirming that the swarm behaviors and individual robot control paradigms designed in Section 6.2 effectively depict each of the fundamental emotions. Therefore, the behaviors considered in this study provide a collection of motion primitives for robotic swarms to convey emotions in artistic expositions, whose trait effectuality could be further evaluated in subsequent studies.

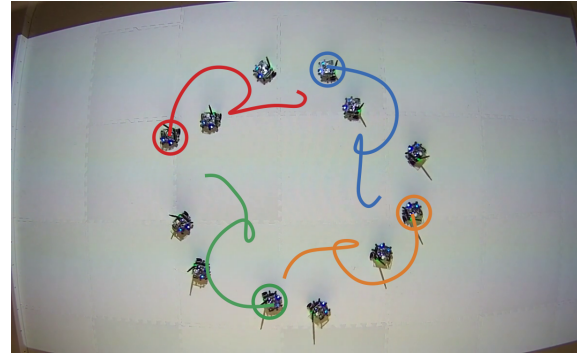
6.4 Robotic Implementation

The swarm behaviors proposed in Section 6.2 and simulated for the user study in Section 6.3 were implemented on a real robotic platform to evaluate their efficacy. Each behavior was executed by a team of 12 GRITSBots X on the Robotarium, a remotely accessible swarm robotics testbed at the Georgia Institute of Technology [191]. Similarly to the GRITSBot (Fig. 6.1), the GRITSBot X has a differential-drive configuration, but with a bigger size: a $10\text{cm} \times 10\text{cm}$ footprint. The robots move on the Robotarium arena, a $4.3\text{m} \times 3.6\text{m}$ surface. The setup is shown in Figs. 6.13 and 6.14.

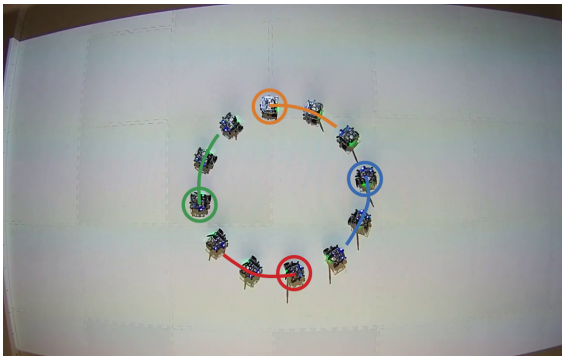
The transition from the simulated behaviors in Section 6.2 and Appendices 6.A and 6.B to their implementation on a real robotic platform involved the tuning of the parameters of the shapes and density functions associated with the behaviors, in accordance to the changes in size of the individual robots as well as of the Robotarium arena. Furthermore, the diffeomorphism parameters (l and K in Section 6.2.2), while still reflected the specifications in Table 6.2 qualitatively, were adjusted to accommodate the dynamics and actuator limits of the GRITSBot X.



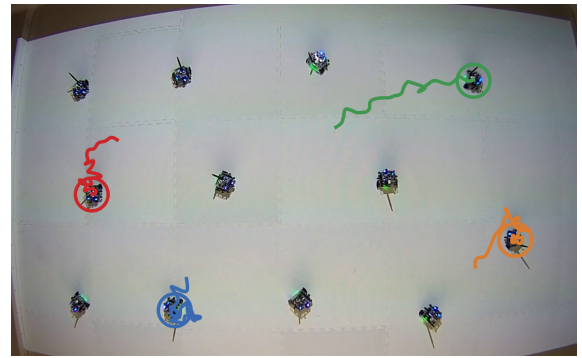
(a) **Happiness**
<https://youtu.be/HQ6YkoADMBg>.



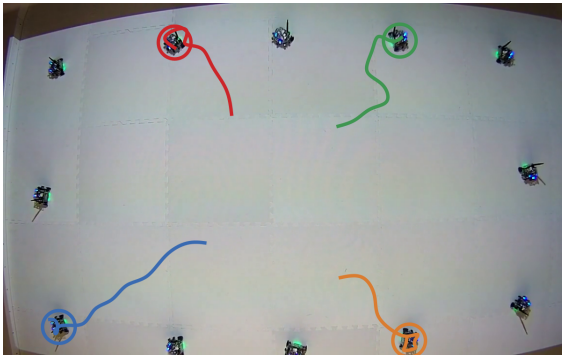
(b) **Surprise**
<https://youtu.be/xhPTQg4iLvM>.



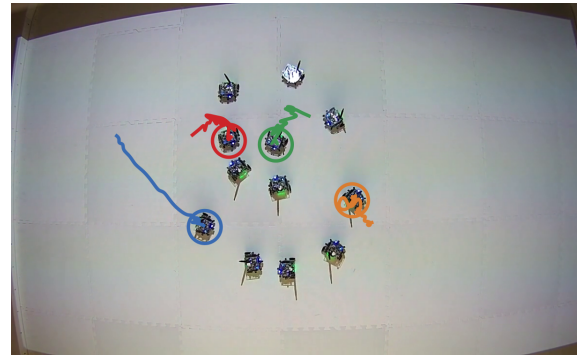
(c) **Sadness**
https://youtu.be/i7cLP_GcL54.



(d) **Fear**
<https://youtu.be/6xqb-sQck6I>.



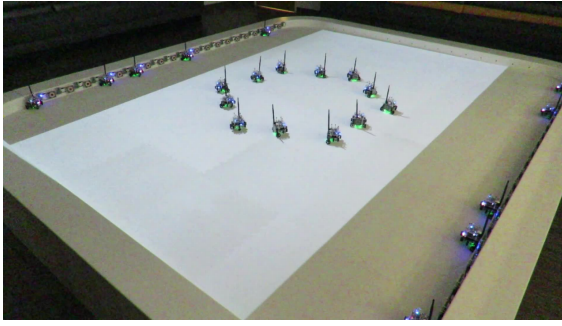
(e) **Disgust**
<https://youtu.be/RgPyXVuprX8>.



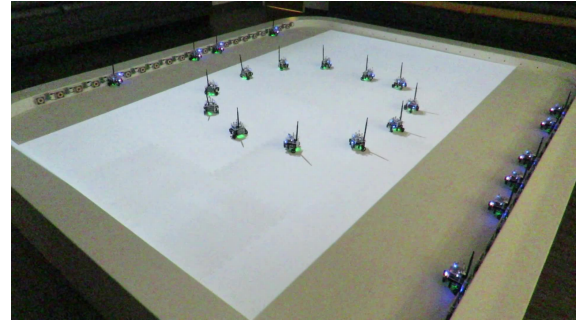
(f) **Anger**
<https://youtu.be/VG1LPJG1wvo>.

Figure 6.13: Snapshots of the swarm behaviors implemented on a team of 12 GRITSBot X, taken in the Robotarium with an overhead camera that provides an analogous perspective to the one used in the simulations (Figs. 6.3 to 6.8). The trajectories of four robots have been plotted using solid lines. A link to the full video of each behavior is provided below each snapshot.

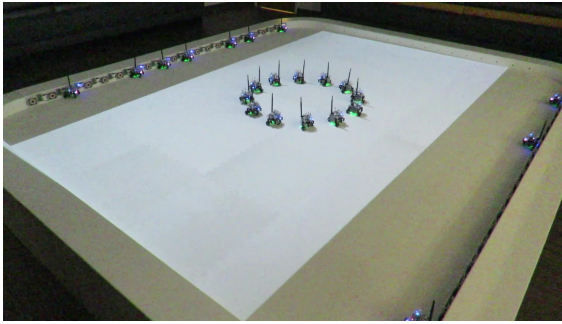
The resulting robotic behaviors are illustrated in Figs. 6.13 and 6.14. Figure 6.13 presents a top view, analogous to the perspective used in the simulations (Figs. 6.3 to



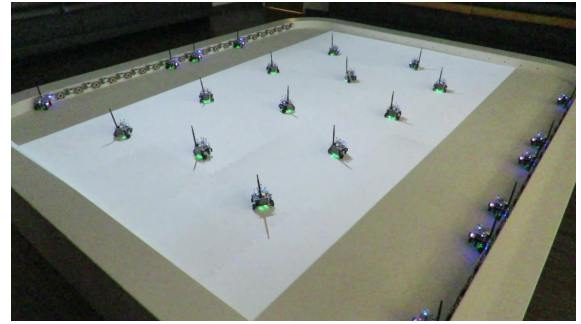
(a) **Happiness.**
<https://youtu.be/EeEyIGn2BV0>.



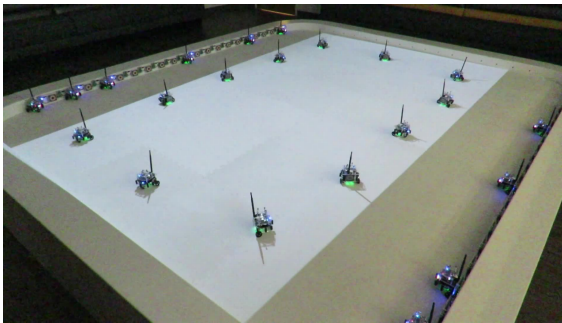
(b) **Surprise**
<https://youtu.be/hHMjYMv6Ojo>.



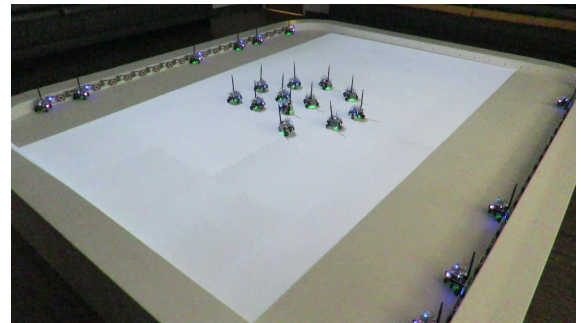
(c) **Sadness**
<https://youtu.be/jFWMtu5oYEo>.



(d) **Fear**
<https://youtu.be/j72EXA14Scs>.



(e) **Disgust**
https://youtu.be/py_cUXCkgZM.



(f) **Anger**
<https://youtu.be/Thj5s1vQvYA>.

Figure 6.14: Snapshots of the swarm behaviors implemented on a team of 12 GRITSBot X in the Robotarium, from a perspective point of view. The snapshots, taken with a camera located 1.70m over the Robotarium surface, provide a similar angle view to that of a human spectator. A link to the full video is provided for each behavior.

6.8), with the purpose of showing the similarity between the simulated behaviors and the real behaviors. As can be observed in the snapshots and linked videos, for most emotions the simulated and real behavior do not present significant differences. The biggest contrast emerges for the anger emotion, where the actuator limits and safety constraints of the

GRITSBot X prevent an exact replication of the simulated behavior, where very high peak velocities were executed by some individuals. Nevertheless, the behavior still portrays its characteristic features as described in Section 6.2. A perspective view of the experiments taken at 1.70m over the Robotarium surface is presented in Fig. 6.14. Despite changing the angle of view to that of an average person, the behaviors are still identifiable and highly distinctive.

6.5 Conclusions

In this chapter, we investigated how motion and shape descriptors from social psychology can be integrated into the control laws of a swarm of robots to express fundamental emotions. Based on such descriptors, a series of swarm behaviors were developed, and their effectiveness in depicting each of the fundamental emotions was analyzed in a user study. The results of the survey showed that, for all the swarm behaviors created, the relative majority of the subjects classified each behavior with the corresponding emotion according to the hypothesis, being this ratio over 50% for 4 of the 6 fundamental emotions.

Some confusion was observed in the classification of the behaviors of fear and disgust, which can be attributed both to the similarity between both emotions in terms of valence and arousal, as well as to the lack of descriptors existent in the literature for the disgust emotion, which complicated the characterization of its associated swarm behavior. Further analysis of the results showed that the robotics background of the participants had no influence on the classification of the behaviors, while the responses of the female participants were more aligned with the hypothesis in comparison to their male counterparts.

The proposed behaviors were implemented on a team of differential drive robots with the objective of illustrating the feasibility of the proposed behaviors on real robotic platforms. While some differences arose between the simulated and the physical implementation due to the dynamics of the robots, each behavior still displayed its characteristic features. This suggests that the control laws proposed for the different emotions are poten-

tially transferable to other ground robotic systems or even to aerial swarms.

In conclusion, the motion and shape descriptors extracted from social psychology afforded the development of distinct expressive swarm behaviors, identifiable by human observers under one of the fundamental emotions, thus providing a starting point for the design of expressive behaviors for robotic swarms to be used in artistic expositions.

6.A Collective Swarm Behavior

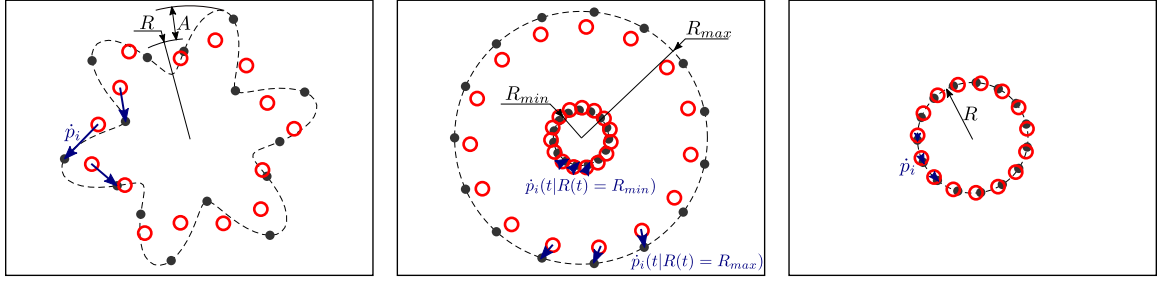
In Section 6.2.1, a series of swarm behaviors were designed based on the movement and shape attributes associated with the different fundamental emotions. This appendix includes the mathematical expressions of the control laws used to produce the different swarm behaviors. Note that all the control laws included here treat each robot in the swarm as a point that can move omnidirectionally according to single integrator dynamics as in (6.1). The transformation from single integrator dynamics to unicycle dynamics is discussed in detail in Appendix 6.B.

6.A.1 Happiness

The swarm movement selected for the happiness behavior consists of the robots following the contour of a circle with a superimposed sinusoid. This shape is illustrated in Fig. 6.15a and can be parameterized as

$$\begin{aligned} x_h(\theta) &= (R + A \sin(f\theta)) \cos \theta, \\ y_h(\theta) &= (R + A \sin(f\theta)) \sin \theta, \end{aligned} \quad \theta \in [0, 2\pi), \quad (6.2)$$

where R is the radius of the main circle and A and f are the amplitude and frequency of the superposed sinusoid, respectively. For the shape in Fig. 6.15a, the frequency of the superimposed sinusoid is $f = 6$.



(a) Happiness: The robots follow points moving along a circle of radius R with a superposed sinusoid of amplitude A .

(b) Surprise: The robots follow points moving along a circle of expanding radius. Two snapshots, corresponding to $R(t) = \{R_{min}, R_{max}\}$, are shown here.

(c) Sadness: The robots follow points that move slowly along the contour of a small circle with respect to the dimensions of the domain.

Figure 6.15: Shapes selected for the happiness, surprise and sadness swarm behaviors. Each agent—here depicted as a red circle—follows a point (black circle) that moves along the dashed trajectory. The go-to-go controller that makes each agent follow the corresponding point is illustrated with blue arrows for 3 of the agents.

If we have a swarm of N robots, we can initially position Robot i according to

$$p_i(0) = [x_h(\theta_i(0)), y_h(\theta_i(0))]^T, \quad i = 1, \dots, N,$$

with

$$\theta_i(0) = 2\pi i/N. \quad (6.3)$$

Then the team will depict the desired shape if each robot follows a point evolving along the contour in (6.2),

$$\dot{p}_i = [x_h(\theta_i(t)), y_h(\theta_i(t))]^T - p_i, \quad (6.4)$$

with θ_i a function of time $t \in \mathbb{R}_+$,

$$\theta_i(t) = \text{atan2}(\sin(t + \theta_i(0)), \cos(t + \theta_i(0))). \quad (6.5)$$

6.A.2 Surprise

In the case of the surprise emotion, each robot follows a point moving along a circle with expanding radius, as in Fig. 6.15b. Such shape can be parameterized as,

$$\begin{aligned} x_{sur}(\theta, t) &= R(t) \cos \theta, \\ y_{sur}(\theta, t) &= R(t) \sin \theta, \end{aligned} \quad \theta \in [0, 2\pi),$$

with $R(t) = \text{mod}(t, R_{max} - R_{min}) + R_{min}$, $t \in \mathbb{R}_+$, to create a radius that expands from R_{min} to R_{max} .

Analogously to the procedure described in Section 6.A.1, in this case the robots can be initially located at

$$p_i(0) = [x_{sur}(\theta_i(0), 0), y_{sur}(\theta_i(0), 0)]^T, \quad i = 1, \dots, N,$$

with $\theta_i(0)$ given by (6.3). The controller for each robot is then given by,

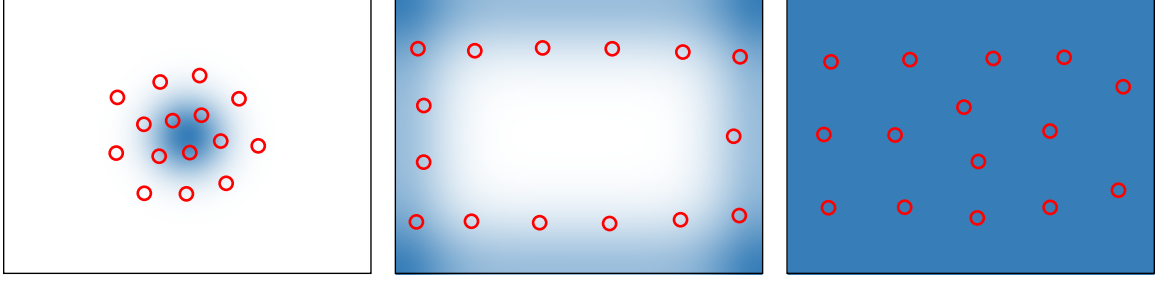
$$\dot{p}_i = [x_{sur}(\theta_i(t), 0), y_{sur}(\theta_i(t), 0)]^T - p_i, \quad (6.6)$$

with $\theta_i(t)$ as in (6.5).

6.A.3 Sadness

For the case of the sadness emotion, the robots move along a circle of small dimension as compared to the domain. The strategy is analogous to the ones in (6.4) and (6.6), with the parameterization of the contour given by,

$$\begin{aligned} x_{sad}(\theta) &= R \cos \theta, \\ y_{sad}(\theta) &= R \sin \theta, \end{aligned} \quad \theta \in [0, 2\pi), \quad R > 0.$$



(a) Anger: the Gaussian density makes the robots concentrate around the center of the domain. This choice, along with the selection of a large proportional gain in the diffeomorphism in (6.10), makes the robots stay in each other's vicinity and react to each others movement, producing a jarring movement trace.

(b) Disgust: the density function presents high values along the boundaries of the domain. This choice allows the team to spread along the boundary, giving the sensation of animosity between robots.

(c) Fear: the density function is chosen to be uniform across the domain. With this choice, the robots scatter evenly over the domain from their initial positions.

Figure 6.16: Density functions associated to represent the emotions of anger (a), disgust (b) and fear (c). The higher the density (darker color), the higher the concentration of robots will be in that area. The red circles represent the position of the agents once the control law in (6.7) has converged.

6.A.4 Anger, Fear and Disgust

For the remaining emotions—anger, disgust and fear—the swarm coordination is based on the *coverage control* strategy, which allows the user to define which areas the robots should concentrate around.

If we denote by \mathcal{D} the domain of the robots, the areas where we want to position the robots can be specified by defining a density function, $\phi : \mathcal{D} \mapsto [0, \infty)$, that assigns higher values to those areas where we desire the robots to concentrate around. We can make the robots distribute themselves according to this density function by implementing the coverage control strategy detailed at Section 2.1, i.e.

$$\dot{p}_i = \kappa(c_i(p) - p_i), \quad (6.7)$$

where $p = [p_1^T, \dots, p_N^T]^T$ denotes the aggregate positions of the robots and $\kappa > 0$ is a

proportional gain. In the controller in (6.7), $c_i(p)$ denotes the center of mass of the Voronoi cell of Robot i ,

$$c_i(p) = \frac{\int_{V_i(p)} q \phi(q) dq}{\int_{V_i(p)} \phi(q) dq},$$

with the Voronoi cell being characterized as,

$$V_i(p) = \{q \in \mathcal{D} \mid \|q - p_i\| \leq \|q - p_j\|, j \in \{1, \dots, N\}, j \neq i\}.$$

Fig. 6.16 shows the densities selected for each of the emotions, where the red circles represent the positions of the robots in the domain upon convergence, achieved by running the controller in (6.7).

6.B Individual Robot Control

The swarm behaviors described in Appendix 6.A assume that each robot in the swarm can move omnidirectionally according to

$$\dot{p}_i = u_i, \tag{6.8}$$

with $p_i = (x_i, y_i)^T \in \mathbb{R}^2$ the Cartesian position of Robot i in the plane and $u_i = (u_{ix}, u_{iy})^T \in \mathbb{R}^2$ the desired velocity. However, the GRITSBot (Fig. 6.1) has a differential-drive configuration and cannot move omnidirectionally as its motion is constrained in the direction perpendicular to its wheels. Instead, its motion can be expressed as unicycle dynamics,

$$\dot{x}_i = v_i \cos \theta_i, \quad \dot{y}_i = v_i \sin \theta_i, \quad \dot{\theta}_i = \omega_i, \tag{6.9}$$

with θ_i the orientation of Robot i and $(v_i, \omega_i)^T$ the linear and angular velocities executable by the robot, as shown in Fig. 6.17.

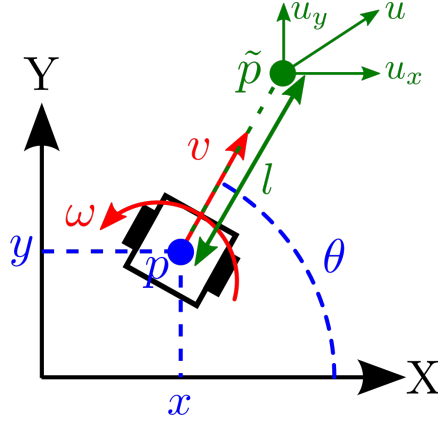


Figure 6.17: Parameters involved in the near-identity diffeomorphism in (6.10), used to transform the single integrator dynamics in (6.8) into unicycle dynamics (6.9), executable by the GRITSBots. The pose of the robot is determined by its position, $p = (x, y)^T$, and its orientation, θ . The single integrator control, u , is applied to a point \tilde{p} located at a distance l in front of the robot. The linear and angular velocities, v and ω , that allow the robot to track \tilde{p} are obtained applying the near-identity diffeomorphism in (6.10).

In this study, the single integrator dynamics in (6.8) are converted into unicycle dynamics, as in (6.9), using a near-identity diffeomorphism [200],

$$\begin{pmatrix} v_i \\ \omega_i \end{pmatrix} = K \begin{pmatrix} \cos \theta_i & \sin \theta_i \\ -\frac{\sin \theta_i}{l} & \frac{\cos \theta_i}{l} \end{pmatrix} \begin{pmatrix} u_x \\ u_y \end{pmatrix}, \quad K, l > 0. \quad (6.10)$$

A graphical representation of this transformation is included in Fig. 6.17: the input $u = (u_x, u_y)^T$ is applied to a point located at a distance of l in front of the robot, \tilde{p} , which can move according to the single integrator dynamics in (6.8). The effect of the parameter l in the movement of the robot is illustrated in Fig. 6.9. The parameter K acts as a proportional gain.

CHAPTER 7

CONCLUSIONS AND FUTURE DIRECTIONS

Robotic swarms, with their inherent features such as redundancy, increased spatial coverage, and reduced price, constitute coveted robotic systems for applications such as environmental monitoring, search and rescue or precision agriculture. Furthermore, the spatial reconfigurability that these platforms offer has become especially attractive for entertainers, which have commercially deployed robotic swarms in performances and exhibitions. However, controlling the robotic swarm as a whole can pose technical challenges for human operators, which may be unable to simultaneously deal with tens or hundreds of robots. Coverage control provides an effective swarm robotics control strategy where the task to be performed by the team can be modeled as a density function over the domain where the robots move.

This thesis explored two fundamental aspects of the coverage control problem. The first part of the thesis, Chapters 3 and 4, dived into the distributed coordination of the multi-robot team under different scenarios concerning the density functions over the domain. In particular, this thesis investigated how the control of the robotic swarm should be performed when the robots, equipped with different sensors—i.e. being a heterogeneous team in terms of sensing capabilities, are tasked with covering different types of events over the domain, possibly time-varying. In contrast, the second part of the thesis, Chapters 5 and 6, focused on the use of coverage control as an interaction strategy for humans to control robotic swarms for different types of artistic expositions, namely artistic painting and expressive motion.

In Chapter 3, we introduced heterogeneity in the coverage problem formulation to reflect qualitatively different sensing modalities among the robots. In contrast to previous approaches to introducing heterogeneity in the coverage control problem, which consid-

ered differences among the robots but maintained the relative importance of the points in the domain common to all the agents, our problem formulation considered different density functions that could be detected by the different types of sensors of the team. The chapter presented two different approaches to this problem, with varying levels of information exchange among the robots in the team, and developed distributed control laws to optimize the coverage of the different events in the domain. Based on the results presented in this thesis, possible extensions on the topic of heterogeneous coverage could involve contemplating limitations on the individual robotic platforms—e.g. restrictions on computational power or payload—which could potentially hinder the simultaneous surveillance of multiple events and, in consequence, impact the collective performance of the team. Along these lines, other issues to consider within this framework could involve optimizing sensor equipment allocation within the team as a function of the domain events or considering sequencing among the robots’ monitoring activities with respect to different events in order to reflect different progress or needs about information gathering in the environment.

The topic of coverage of time-varying density functions was the object of study of Chapter 4. Although this was not a first stab at this problem in the literature, this thesis presented an exact and decentralized constraint-based solution to this problem. While the approach was developed in detail for the case of time-varying density functions in the homogeneous coverage control case (i.e. the relative importance of each point in the domain, while subject to change over time, is common to all the agents in the team), the generality of the formulation afforded its extension to the two heterogeneous coverage strategies from Chapter 3. The constraint-based approach presented in Chapter 4, therefore, seems to smoothly accommodate the introduction of time-varying density functions on other instantiations of the coverage problem, as long as the performance of the multi-robot system is adequately characterized by a locational cost and its corresponding critical points. Furthermore, as explained in Chapter 4, the attractiveness of this approach also relies on its composability with other tasks to be executed concurrently by the multi-robot team. Some

extensions of this work could involve studying the limitations of the constraint-based approach for different instantiations of the coverage problem, as well as the effects of task addition through other constraints on the performance of the original task—i.e. how would the concurrent execution of other tasks affect the coverage performance of the team.

The second part of the thesis focused on exploring coverage as an interaction paradigm between artists and robotic swarms for different forms of artistic expression. In particular, the heterogeneous coverage formulation from Chapter 3 was used in Chapter 5 as an interaction paradigm between artists and multi-robot systems to produce artistic paintings based on the specification of desired color densities over the domain. This chapter explored not only the ability of coverage control to provide an effective interaction modality, but also the implications that different levels of heterogeneity within the team have in the resulting painting. In Chapter 6, the homogeneous coverage control strategy developed by Cortés, along with another standard multi-robot control algorithm (i.e. cyclic pursuit), were used as a basis to create emotionally expressive behaviors for swarms to be used in artistic exhibitions. Taking advantage of the collective behaviors provided by these swarm control strategies, as well as of the types of trajectories individual robots can execute, a series of swarm behaviors associated with the different fundamental emotions were developed in this chapter, and evaluated through a user study.

The developments in this thesis lead to many possible connections between robotic swarms and different forms of art. The proposed solutions for artistic painting and expressive motion constitute specific instantiations of robot swarms being used for such applications, with many other swarm control algorithms (e.g. consensus/dissensus, flocking, formation control) and interaction modalities among the robots (e.g. distance-based, pheromone-based) yet to be evaluated for the same purposes. Furthermore, an interesting extension of the work presented in this thesis—and within the context of swarm robotics and arts in general—would entail evaluating the preferred human-swarm interaction modalities for human artists to interact with the robots. Regarding the use of coverage control for

artistic applications, one could continue regarding density functions as a way to command the artist's intent to the swarm, as in the artistic painting scenario in Chapter 5 or the expressive swarm behaviors in Chapter 6. However, a particular work of art could also be seen as the generator of the densities to be covered by the robots, being the swarm movement the result of this robot-art interaction: e.g. the robots could move according to densities generated from music progressions or poetry structures. Nevertheless, the intersection of swarm robotics and arts remains mostly unexplored, with endless possibilities to be developed in this realm.

REFERENCES

- [1] M. Brambilla, E. Ferrante, M. Birattari, and M. Dorigo, “Swarm robotics: A review from the swarm engineering perspective”, *Swarm Intelligence*, vol. 7, no. 1, pp. 1–41, Mar. 2013.
- [2] C. A. Kitts and M. Egerstedt, “Design, control, and applications of real-world multirobot systems [from the guest editors]”, *IEEE Robotics Automation Magazine*, vol. 15, no. 1, pp. 8–8, Mar. 2008.
- [3] J. Cortes and M. Egerstedt, “Coordinated control of multi-robot systems: A survey”, *SICE Journal of Control, Measurement, and System Integration*, vol. 10, no. 6, pp. 495–503, 2017.
- [4] A. Vitanza, P. Rossetti, F. Mondada, and V. Trianni, “Robot swarms as an educational tool: The thymios way”, *International Journal of Advanced Robotic Systems*, vol. 16, no. 1, p. 1 729 881 418 825 186, 2019.
- [5] E. Ackerman, “Flying LampshadeBots Come Alive in Cirque du Soleil”, *IEEE Spectrum*, 2014.
- [6] J. Cortes, S. Martinez, T. Karatas, and F. Bullo, “Coverage control for mobile sensing networks”, *IEEE Transactions on Robotics and Automation*, vol. 20, no. 2, pp. 243–255, Apr. 2004.
- [7] F. Bullo, J. Cortes, and S. Martinez, *Distributed Control of Robotic Networks: A Mathematical Approach to Motion Coordination Algorithms*, ser. Applied Mathematics Series. Princeton, NJ, USA: Princeton University Press, 2009.
- [8] Y. Diaz-Mercado, S. G. Lee, and M. Egerstedt, “Distributed Dynamic Density Coverage for Human-Swarm Interactions”, in *American Control Conference (ACC)*, 2015, Jul. 2015, pp. 353–358.
- [9] G. Theraulaz, E. Bonabeau, and J.-L. Deneubourg, “Response threshold reinforcement and division of labour in insect societies”, *Proceedings: Biological Sciences*, vol. 265, no. 1393, pp. 327–332, 1998.
- [10] M. Waibel, D. Floreano, S. Magnenat, and L. Keller, “Division of labour and colony efficiency in social insects: Effects of interactions between genetic architecture, colony kin structure and rate of perturbations”, *Proceedings of the Royal Society B: Biological Sciences*, vol. 273, no. 1595, pp. 1815–1823, 2006.

- [11] L. A. Curral, R. H. Forrester, J. F. Dawson, and M. A. West, “It’s what you do and the way that you do it: Team task, team size, and innovation-related group processes”, *European Journal of Work and Organizational Psychology*, vol. 10, no. 2, pp. 187–204, 2001.
- [12] R. T. Keller, “Cross-functional project groups in research and new product development: Diversity, communications, job stress, and outcomes”, *The Academy of Management Journal*, vol. 44, no. 3, pp. 547–555, 2001.
- [13] A. Somech, “The effects of leadership style and team process on performance and innovation in functionally heterogeneous teams”, *Journal of Management*, vol. 32, no. 1, pp. 132–157, 2006.
- [14] H. A. Nissen, M. R. Evald, and A. H. Clarke, “Knowledge sharing in heterogeneous teams through collaboration and cooperation: Exemplified through publicprivate-innovation partnerships”, *Industrial Marketing Management*, vol. 43, no. 3, pp. 473–482, 2014, Special Issue on Innovation in Networks - Per Freytag and Louise Young.
- [15] K. Ingersoll, E. Malesky, and S. M. Saiegh, “Heterogeneity and team performance: Evaluating the effect of cultural diversity in the worlds top soccer league”, *Journal of Sports Analytics*, vol. 3, no. 2, pp. 67–92, 2017.
- [16] L. E. Parker, “Adaptive heterogeneous multi-robot teams”, *Neurocomputing*, vol. 28, no. 1, pp. 75–92, 1999.
- [17] P. Stone and M. Veloso, “Multiagent systems: A survey from a machine learning perspective”, *Autonomous Robots*, vol. 8, no. 3, pp. 345–383, 2000.
- [18] A. Prorok and V. Kumar, “A macroscopic privacy model for heterogeneous robot swarms”, in *Swarm Intelligence*, M. Dorigo, M. Birattari, X. Li, M. López-Ibáñez, K. Ohkura, C. Pinciroli, and T. Stützle, Eds., Cham: Springer International Publishing, 2016, pp. 15–27.
- [19] T. Balch, “The impact of diversity on performance in multi-robot foraging”, in *Proceedings of the Third Annual Conference on Autonomous Agents*, ser. AGENTS 99, Seattle, Washington, USA: Association for Computing Machinery, 1999, 9299.
- [20] L. C. A. Pimenta, V. Kumar, R. C. Mesquita, and G. A. S. Pereira, “Sensing and coverage for a network of heterogeneous robots”, in *IEEE Conference on Decision and Control*, Cancún, México, Dec. 2008, pp. 3947–3952.
- [21] A. Pierson, L. C. Figueiredo, L. C. A. Pimenta, and M. Schwager, “Adapting to performance variations in multi-robot coverage”, in *2015 IEEE International Conference on Robotics and Automation (ICRA)*, Seattle, WA, May 2015, pp. 415–420.

- [22] L. Wang, A. Ames, and M. Egerstedt, “Safety barrier certificates for heterogeneous multi-robot systems”, in *2016 American Control Conference (ACC)*, 2016, pp. 5213–5218.
- [23] G. Notomista, S. Mayya, S. Hutchinson, and M. Egerstedt, “An optimal task allocation strategy for heterogeneous multi-robot systems”, in *2019 18th European Control Conference (ECC)*, Jun. 2019, pp. 2071–2076.
- [24] A. Kolling, P. Walker, N. Chakraborty, K. Sycara, and M. Lewis, “Human interaction with robot swarms: A survey”, *IEEE Transactions on Human-Machine Systems*, vol. 46, no. 1, pp. 9–26, Feb. 2016.
- [25] A. LaViers and M. Egerstedt, Eds., *Controls and Art: Inquiries at the Intersection of the Subjective and the Objective*. Cham: Springer International Publishing, 2014.
- [26] D. Herath, C. Kroos, and Stelarc, Eds., *Robots and Art: Exploring an Unlikely Symbiosis*. Singapore: Springer, 2016.
- [27] A. P. Schoellig, H. Siegel, F. Augugliaro, and R. D’Andrea, “So you think you can dance? rhythmic flight performances with quadrocopters”, in *Controls and Art: Inquiries at the Intersection of the Subjective and the Objective*, A. LaViers and M. Egerstedt, Eds. Cham: Springer International Publishing, 2014, pp. 73–105.
- [28] O. Games, *Experience the future of the olympic games with intel*, <https://www.olympic.org/news/experience-the-future-of-the-olympic-games-with-intel>, Accessed 2020-05-15, 2018.
- [29] J. Cortes, S. Martinez, T. Karatas, and F. Bullo, “Coverage control for mobile sensing networks: Variations on a theme”, in *Proceedings of the 10th Mediterranean Conference on Control and Automation*, Lisbon, Portugal, Jul. 2002.
- [30] J.-M. McNew, E. Klavins, and M. Egerstedt, “Solving coverage problems with embedded graph grammars”, in *Hybrid Systems: Computation and Control: 10th International Workshop*, A. Bemporad, A. Bicchi, and G. Buttazzo, Eds., Pisa, Italy: Springer Berlin Heidelberg, Apr. 2007, pp. 413–427.
- [31] S. Meguerdichian, F. Koushanfar, M. Potkonjak, and M. B. Srivastava, “Coverage problems in wireless ad-hoc sensor networks”, in *Proceedings of IEEE INFOCOM Conference on Computer Communications*, vol. 3, Anchorage, AK, Apr. 2001, pp. 1380–1387.
- [32] H. Jaleel, A. Rahmani, and M. Egerstedt, “Probabilistic lifetime maximization of sensor networks”, *IEEE Transactions on Automatic Control*, vol. 58, no. 2, pp. 534–539, Feb. 2013.

- [33] M. Iri, K. Murota, and T. Ohya, “A fast voronoi-diagram algorithm with applications to geographical optimization problems”, in *System Modelling and Optimization*, P. Thoft-Christensen, Ed., Berlin, Heidelberg: Springer Berlin Heidelberg, 1984, pp. 273–288.
- [34] Y. Ohsawa and A. Suzuki, “Location-allocation problem of multi-person facility”, *Journal of the Operations Research Society of Japan*, vol. 30, no. 3, pp. 368–395, 1987.
- [35] T. Suzuki, Y. Asami, and A. Okabe, “Sequential location allocation of public facilities in one- and two-dimensional space: Comparison of several policies”, *Mathematical Programming*, vol. 52, pp. 125–146, 1991.
- [36] A. Okabe, B. Boots, K. Sugihara, and S. N. Chiu, *Spatial Tessellations: Concepts and Applications of Voronoi Diagrams*. New York, NY, USA: John Wiley & Sons, Inc., 2000.
- [37] G. W. Barlow, “Hexagonal territories”, *Animal Behaviour*, vol. 22, 876 –IN1, 1974.
- [38] M. Hasegawa and M. Tanemura, “On the pattern of space division by territories”, *Annals of the Institute of Statistical Mathematics*, vol. 28, pp. 509–519, 1976.
- [39] R. Votel, D. A. W. Barton, T. Gotou, T. Hatanaka, M. Fujita, and J. Moehlis, “Equilibrium configurations for a territorial model”, *SIAM Journal on Applied Dynamical Systems*, vol. 8, no. 3, pp. 1234–1260, 2009.
- [40] H. Honda, “Description of cellular patterns by dirichlet domains: The two-dimensional case”, *Journal of Theoretical Biology*, vol. 72, no. 3, pp. 523 –543, 1978.
- [41] M. Bock, A. K. Tyagi, J.-U. Kreft, and W. Alt, “Generalized voronoi tessellation as a model of two-dimensional cell tissue dynamics.”, *Bulletin of mathematical biology*, vol. 72, no. 7, pp. 1696–1731, Oct. 2010.
- [42] D. Sánchez-Gutiérrez, M. Tozluoglu, J. D. Barry, A. Pascual, Y. Mao, and L. M. Escudero, “Fundamental physical cellular constraints drive self-organization of tissues”, *The EMBO Journal*, vol. 35, no. 1, pp. 77–88, 2016.
- [43] S. Lloyd, “Least squares quantization in PCM”, *IEEE Transactions on Information Theory*, vol. 28, no. 2, pp. 129–137, Mar. 1982.
- [44] M. Schwager, J. Mclurkin, and D. Rus, “Distributed coverage control with sensory feedback for networked robots”, in *in Proceedings of Robotics: Science and Systems*, 2006.

- [45] Q. Du, V. Faber, and M. Gunzburger, “Centroidal voronoi tessellations: Applications and algorithms”, *SIAM Review*, vol. 41, no. 4, pp. 637–676, Dec. 1999.
- [46] Y. Kantaros, M. Thanou, and A. Tzes, “Distributed coverage control for concave areas by a heterogeneous robotswarm with visibility sensing constraints”, *Automatica*, vol. 53, pp. 195–207, Mar. 2015.
- [47] S. Bhattacharya, R. Ghrist, and V. Kumar, “Multi-robot coverage and exploration on riemannian manifolds with boundaries”, *The International Journal of Robotics Research*, vol. 33, no. 1, pp. 113–137, 2014.
- [48] X. Xu and Y. Diaz-Mercado, “Multi-robot control using coverage over time-varying domains: Extended abstract”, in *2019 International Symposium on Multi-Robot and Multi-Agent Systems (MRS)*, 2019, pp. 179–181.
- [49] X. Xu and Y. Diaz-Mercado, “Multi-agent control using coverage over time-varying domains”, arXiv version available at <https://arxiv.org/pdf/1909.05377.pdf>, 2019.
- [50] A. Pierson and D. Rus, “Distributed target tracking in cluttered environments with guaranteed collision avoidance”, in *2017 International Symposium on Multi-Robot and Multi-Agent Systems (MRS)*, 2017, pp. 83–89.
- [51] M. Wang and M. Schwager, “Distributed collision avoidance of multiple robots with probabilistic buffered voronoi cells”, in *2019 International Symposium on Multi-Robot and Multi-Agent Systems (MRS)*, 2019, pp. 169–175.
- [52] G. Notomista and M. Egerstedt, “Coverage control for wire-traversing robots”, in *2018 IEEE International Conference on Robotics and Automation (ICRA)*, 2018, pp. 5042–5047.
- [53] G. Notomista, M. Santos, S. Hutchinson, and M. Egerstedt, “Sensor coverage control using robots constrained to a curve”, in *2019 International Conference on Robotics and Automation (ICRA)*, 2019, pp. 3252–3258.
- [54] J. Wagenpfeil, A. Trachte, Takeshi Hatanaka, Masayuki Fujita, and O. Sawodny, “Distributed decision making for task switching via a consensus-like algorithm”, in *2009 American Control Conference*, 2009, pp. 5761–5766.
- [55] P. Dames, “Distributed multi-target search and tracking using the phd filter”, *Autonomous Robots*, vol. 44, pp. 673–689, 2020.
- [56] M. Schwager, D. Rus, and J.-J. Slotine, “Decentralized, adaptive coverage control for networked robots”, *The International Journal of Robotics Research*, vol. 28, no. 3, pp. 357–375, 2009.

- [57] C. Song, G. Feng, Y. Fan, and Y. Wang, “Decentralized adaptive awareness coverage control for multi-agent networks”, *Automatica*, vol. 47, no. 12, pp. 2749–2756, 2011.
- [58] “Discoverage: From coverage to distributed multi-robot exploration*”, *IFAC Proceedings Volumes*, vol. 46, no. 27, pp. 328–335, 2013, 4th IFAC Workshop on Distributed Estimation and Control in Networked Systems (2013).
- [59] M. Schwager, M. P. Vitus, D. Rus, and C. J. Tomlin, “Robust adaptive coverage for robotic sensor networks”, in *Robotics Research : The 15th International Symposium ISRR*, H. I. Christensen and O. Khatib, Eds. Cham: Springer International Publishing, 2017, pp. 437–454.
- [60] W. Luo and K. Sycara, “Adaptive sampling and online learning in multi-robot sensor coverage with mixture of gaussian processes”, in *2018 IEEE International Conference on Robotics and Automation (ICRA)*, 2018, pp. 6359–6364.
- [61] A Benevento, M. Santos, G. Notarstefano, K. Paynabar, M. Bloch, and M. Egerstedt, “Multi-robot coordination for estimation and coverage of unknown spatial fields”, in *2020 International Conference on Robotics and Automation (ICRA)*, 2020.
- [62] A. Kwok and S. Martinez, “Unicycle coverage control via hybrid modeling”, *IEEE Transactions on Automatic Control*, vol. 55, no. 2, pp. 528–532, 2010.
- [63] L. Klodt, S. Khodaverdian, and V. Willert, “Motion control for uav-ugv cooperation with visibility constraint”, in *2015 IEEE Conference on Control Applications (CCA)*, 2015, pp. 1379–1385.
- [64] A. Kwok and S. Martinez, “Deployment algorithms for a power-constrained mobile sensor network”, in *2008 IEEE International Conference on Robotics and Automation*, May 2008, pp. 140–145.
- [65] A. Gusrialdi, T. Hatanaka, and M. Fujita, “Coverage control for mobile networks with limited-range anisotropic sensors”, in *2008 47th IEEE Conference on Decision and Control*, Dec. 2008, pp. 4263–4268.
- [66] B. Hexsel, N. Chakraborty, and K. Sycara, “Coverage control for mobile anisotropic sensor networks”, in *2011 IEEE International Conference on Robotics and Automation*, May 2011, pp. 2878–2885.
- [67] R. A. Razak, S. Sukumar, and H. Chung, “Distributed coverage control of mobile sensors: Generalized approach using distance functions”, in *2018 IEEE Conference on Decision and Control (CDC)*, 2018, pp. 3323–3328.

- [68] F. Sharifi, Y. Zhang, and A. G. Aghdam, “A distributed deployment strategy for multi-agent systems subject to health degradation and communication delays”, *Journal of Intelligent & Robotic Systems*, vol. 73, pp. 623–633, 2013.
- [69] . Arslan, “Statistical coverage control of mobile sensor networks”, *IEEE Transactions on Robotics*, vol. 35, no. 4, pp. 889–908, 2019.
- [70] T. Hatanaka, R. Funada, and M. Fujita, “Visual surveillance of human activities via gradient-based coverage control on matrix manifolds”, *IEEE Transactions on Control Systems Technology*, pp. 1–15, 2019.
- [71] M. Schwager, B. J. Julian, M. Angermann, and D. Rus, “Eyes in the sky: Decentralized control for the deployment of robotic camera networks”, *Proceedings of the IEEE*, vol. 99, no. 9, pp. 1541–1561, 2011.
- [72] R. Funada, M. Santos, J. Yamauchi, T. Hatanaka, M. Fujita, and M. Egerstedt, “Visual coverage control for teams of quadcopters via control barrier functions”, in *2019 International Conference on Robotics and Automation (ICRA)*, Montréal, Canada, 2019, pp. 3010–3016.
- [73] R. Funada, M. Santos, T. Gencho, J. Yamauchi, M. Fujita, and M. Egerstedt, “Visual coverage maintenance for quadcopters using nonsmooth barrier functions”, in *2020 International Conference on Robotics and Automation (ICRA)*, 2020.
- [74] T. Balch and L. E. Parker, *Robot Teams: From Diversity to Polymorphism*. A K Peters/CRC Press, 2002.
- [75] X. Zhang, X. Chen, X. Liang, and Y. Fang, “Distributed coverage optimization for deployment of directional sensor networks”, in *2015 54th IEEE Conference on Decision and Control (CDC)*, 2015, pp. 246–251.
- [76] F. Farzadpour, X. Zhang, X. Chen, and T. Zhang, “On performance measurement for a heterogeneous planar field sensor network”, in *IEEE International Conference on Advanced Intelligent Mechatronics*, Munich, Germany, Jul. 2017, pp. 166–171.
- [77] J. Marier, C. Rabbath, and N. Lchevin, “Visibility-limited coverage control using nonsmooth optimization”, in *2012 American Control Conference (ACC)*, 2012, pp. 6029–6034.
- [78] O. Arslan and D. E. Koditschek, “Voronoi-based coverage control of heterogeneous disk-shaped robots”, in *2016 IEEE International Conference on Robotics and Automation (ICRA)*, Stockholm, Sweden, May 2016, pp. 4259–4266.

- [79] M. S. Miah and J. Knoll, “Area coverage optimization using heterogeneous robots: Algorithm and implementation”, *IEEE Transactions on Instrumentation and Measurement*, vol. 67, no. 6, pp. 1380–1388, 2018.
- [80] J. Marier, C. Rabbath, and N. Lchevin, “Optimizing the location of sensors subject to health degradation”, in *Proceedings of the 2011 American Control Conference*, 2011, pp. 3760–3765.
- [81] F Aurenhammer, “Power diagrams: Properties, algorithms and applications”, *SIAM Journal on Computing*, vol. 16, no. 1, pp. 78–96, Feb. 1987.
- [82] L. C. A. Pimenta, M. Schwager, Q. Lindsey, V. Kumar, D. Rus, R. C. Mesquita, and G. A. S. Pereira, “Simultaneous coverage and tracking (scat) of moving targets with robot networks”, in *Algorithmic Foundation of Robotics VIII: Selected Contributions of the Eight International Workshop on the Algorithmic Foundations of Robotics*, G. S. Chirikjian, H. Choset, M. Morales, and T. Murphey, Eds. Berlin, Heidelberg: Springer Berlin Heidelberg, 2010, pp. 85–99.
- [83] S. G. Lee, Y. Diaz-Mercado, and M. Egerstedt, “Multi-robot control using time-varying density functions”, *IEEE Transactions on Robotics*, vol. 31, no. 2, pp. 489–493, Apr. 2015.
- [84] J. M. Luna, R. Fierro, C. T. Abdallah, and J. Wood, “An adaptive coverage control for deployment of nonholonomic mobile sensor networks over time-varying sensory functions”, *Asian Journal of Control*, vol. 15, no. 4, pp. 988–1000, 2013.
- [85] C. H. Caicedo-Nez and N. E. Leonard, “Symmetric coverage of dynamic mapping error for mobile sensor networks”, in *Proceedings of the 2011 American Control Conference*, 2011, pp. 4661–4666.
- [86] G. Notomista and M. Egerstedt, “Constraint-driven coordinated control of multi-robot systems”, in *2019 American Control Conference (ACC)*, 2019, pp. 1990–1996.
- [87] K. Shibuya, S. Matsuda, and A. Takahara, “Toward developing a violin playing robot - bowing by anthropomorphic robot arm and sound analysis”, in *RO-MAN 2007 - The 16th IEEE International Symposium on Robot and Human Interactive Communication*, 2007, pp. 763–768.
- [88] J. Solis, Koichi Taniguchi, Takeshi Ninomiya, Tetsuro Yamamoto, and Atsuo Takanishi, “Development of waseda flutist robot wf-4riv: Implementation of auditory feedback system”, in *2008 IEEE International Conference on Robotics and Automation*, 2008, pp. 3654–3659.

- [89] A. Kapur, M. Darling, D. Diakopoulos, J. W. Murphy, J. Hochenbaum, O. Vallis, and C. Bahn, “The machine orchestra: An ensemble of human laptop performers and robotic musical instruments”, *Computer Music Journal*, vol. 35, no. 4, pp. 49–63, 2011.
- [90] M. Bretan, D. Gopinath, P. Mullins, and G. Weinberg, “A robotic prosthesis for an amputee drummer”, arXiv version available at <https://arxiv.org/pdf/1612.04391.pdf>, 2016.
- [91] C. Crick, M. Munz, and B. Scassellati, “Synchronization in social tasks: Robotic drumming”, in *ROMAN 2006 - The 15th IEEE International Symposium on Robot and Human Interactive Communication*, 2006, pp. 97–102.
- [92] G. Hoffman and G. Weinberg, “Gesture-based human-robot jazz improvisation”, in *2010 IEEE International Conference on Robotics and Automation*, May 2010, pp. 582–587.
- [93] A. Nakazawa, S. Nakaoka, K. Ikeuchi, and K. Yokoi, “Imitating human dance motions through motion structure analysis”, in *IEEE/RSJ International Conference on Intelligent Robots and Systems*, vol. 3, Oct. 2002, pp. 2539–2544.
- [94] K. Shinozaki, A. Iwatani, and R. Nakatsu, “Construction and evaluation of a robot dance system”, in *RO-MAN 2008 - The 17th IEEE International Symposium on Robot and Human Interactive Communication*, Aug. 2008, pp. 366–370.
- [95] A. LaViers, L. Teague, and M. Egerstedt, “Style-based robotic motion in contemporary dance performance”, in *Controls and Art: Inquiries at the Intersection of the Subjective and the Objective*, A. LaViers and M. Egerstedt, Eds. Cham: Springer International Publishing, 2014, pp. 205–229.
- [96] C. B. Santiago, J. L. Oliveira, L. P. Reis, and A. Sousa, “Autonomous robot dancing synchronized to musical rhythmic stimuli”, in *6th Iberian Conference on Information Systems and Technologies (CISTI 2011)*, 2011, pp. 1–6.
- [97] T. Bi, P. Fankhauser, D. Bellicoso, and M. Hutter, “Real-time dance generation to music for a legged robot”, in *2018 IEEE/RSJ International Conference on Intelligent Robots and Systems (IROS)*, Madrid, Oct. 2018, pp. 1038–1044.
- [98] C. Breazeal, A. Brooks, J. Gray, M. Hancher, C. Kidd, J. McBean, D. Stiehl, and J. Strickon, “Interactive robot theatre”, in *Proceedings 2003 IEEE/RSJ International Conference on Intelligent Robots and Systems (IROS 2003) (Cat. No.03CH37453)*, vol. 4, 2003, 3648–3655 vol.3.

- [99] D. Lee, S. Park, M. Hahn, and N. Lee, “Robot actors and authoring tools for live performance system”, in *2014 International Conference on Information Science Applications (ICISA)*, May 2014, pp. 1–3.
- [100] M. Perkowski, T. Sasao, J. H. Kim, M. Lukac, J. Allen, and S. Gebauer, “Hahoe KAIST Robot Theatre: Learning rules of interactive robot behavior as a multiple-valued logic synthesis problem”, in *35th International Symposium on Multiple-Valued Logic (ISMVL’05)*, May 2005, pp. 236–248.
- [101] M. Sunardi and M. Perkowski, “Music to motion: Using music information to create expressive robot motion”, *International Journal of Social Robotics*, vol. 10, no. 1, pp. 43–63, Jan. 2018.
- [102] F. Augugliaro, A. P. Schoellig, and R. D’Andrea, “Dance of the flying machines: Methods for designing and executing an aerial dance choreography”, *IEEE Robotics Automation Magazine*, vol. 20, no. 4, pp. 96–104, 2013.
- [103] T. Lindemeier, S. Pirk, and O. Deussen, “Image stylization with a painting machine using semantic hints”, *Computers & Graphics*, vol. 37, no. 5, pp. 293–301, 2013.
- [104] P. Tresset and F. F. Leymarie, “Portrait drawing by paul the robot”, *Computers & Graphics*, vol. 37, no. 5, pp. 348–363, 2013.
- [105] K. Goldberg, *The telegarden*, <https://goldberg.berkeley.edu/garden/>, Accessed 2020-05-15, 1995-2004.
- [106] M. Dean, R. D’Andrea, and M. Donovan, *Robotic Chair*. Vancouver, B.C.: Contemporary Art Gallery, 2008.
- [107] E. Jochum and K. Goldberg, “Cultivating the uncanny: The telegarden and other oddities”, in *Robots and Art: Exploring an Unlikely Symbiosis*, D. Herath, C. Kroos, and Stelarc, Eds. Singapore: Springer Singapore, 2016, pp. 149–175.
- [108] B. J. Dunstan, D. Silvera-Tawil, J. T.K. V. Koh, and M. Velonaki, “Cultural robotics: Robots as participants and creators of culture”, in *Cultural Robotics*, J. T. Koh, B. J. Dunstan, D. Silvera-Tawil, and M. Velonaki, Eds., Cham: Springer International Publishing, 2016, pp. 3–13.
- [109] E. Vlachos, E. Jochum, and L. Demers, “Heat: The harmony exoskeleton self - assessment test”, in *2018 27th IEEE International Symposium on Robot and Human Interactive Communication (RO-MAN)*, Aug. 2018, pp. 577–582.
- [110] C. Cuan, I. Pakrasi, and A. LaViers, “Time to compile : An interactive art installation”, in *The Sixteenth Biennial Symposium on Arts & Technology*, 2018.

- [111] J. Alonso-Mora, R. Siegwart, and P. Beardsley, “Human-Robot swarm interaction for entertainment: From animation display to gesture based control”, in *Proceedings of the 2014 ACM/IEEE International Conference on Human-robot Interaction*, Bielefeld, Germany: ACM, 2014, pp. 98–98.
- [112] M. T. Santos Fernandez, “Musical abstractions for multi-robot coordination”, Master’s thesis, Atlanta, GA, USA, 2016.
- [113] M. Santos and M. Egerstedt, “From motions to emotions: Can the fundamental emotions be expressed in a robot swarm?”, *International Journal of Social Robotics*, 2020, To appear.
- [114] G. Dietz, J. L. E, P. Washington, L. H. Kim, and S. Follmer, “Human perception of swarm robot motion”, in *CHI Conference Extended Abstracts on Human Factors in Computing Systems*, Denver, Colorado, 2017, pp. 2520–2527.
- [115] F. Levillain, D. St-Onge, E. Zibetti, and G. Beltrame, “More than the sum of its parts: Assessing the coherence and expressivity of a robotic swarm”, in *IEEE International Symposium on Robot and Human Interactive Communication*, 2018, pp. 583–588.
- [116] D. St-Onge, F. Levillain, Z. Elisabetta, and G. Beltrame, “Collective expression: How robotic swarms convey information with group motion”, *Paladyn, Journal of Behavioral Robotics*, vol. 10, pp. 418–435, Dec. 2019.
- [117] A. Albin, G. Weinberg, and M. Egerstedt, “Musical abstractions in distributed multi-robot systems”, in *2012 IEEE/RSJ International Conference on Intelligent Robots and Systems*, Oct. 2012, pp. 451–458.
- [118] L. Moura and V. Ramos, *Swarm Paintings—Nonhuman Art*, J. Maubant and et al, Eds. Lyon/Villeurbanne, France: Architopia: Book, Art, Architecture, and Science, Institut d’Art Contemporain, 2002, pp. 5–24.
- [119] L. Moura, “Machines that make art”, in. May 2016, pp. 255–269.
- [120] S. Chung, *Omnia per omnia*, sougwen.com/project/omniaperomnia, Accessed 2019-09-08, 2018.
- [121] S. Calinon, J. Epiney, and A. Billard, “A humanoid robot drawing human portraits”, in *5th IEEE-RAS International Conference on Humanoid Robots, 2005.*, 2005, pp. 161–166.
- [122] C. Lin, T. T. Mac, and L. Chuang, “Real-time artistic human face portrait by humanoid robot”, in *2009 IEEE Control Applications, (CCA) Intelligent Control, (ISIC)*, 2009, pp. 205–210.

- [123] D. Song, T. Lee, and Y. J. Kim, “Artistic pen drawing on an arbitrary surface using an impedance-controlled robot”, in *2018 IEEE International Conference on Robotics and Automation (ICRA)*, 2018, pp. 4085–4090.
- [124] A. Kotani and S. Tellex, “Teaching robots to draw”, in *2019 International Conference on Robotics and Automation (ICRA)*, 2019, pp. 4797–4803.
- [125] S. Wang, J. Chen, X. Deng, S. Hutchinson, and F. Dellaert, “Robot calligraphy using pseudospectral optimal control in conjunction with a novel dynamic brush model”, arXiv version available at <https://arxiv.org/pdf/2003.01565.pdf>, 2020.
- [126] R. C. Luo, M. Hong, and P. Chung, “Robot artist for colorful picture painting with visual control system”, in *2016 IEEE/RSJ International Conference on Intelligent Robots and Systems (IROS)*, 2016, pp. 2998–3003.
- [127] A. I. Karimov, D. O. Pesterev, V. Y. Ostrovskii, D. N. Butusov, and E. E. Kopets, “Brushstroke rendering algorithm for a painting robot”, in *2017 International Conference “Quality Management, Transport and Information Security, Information Technologies” (IT QM IS)*, 2017, pp. 331–334.
- [128] A. I. Karimov, E. E. Kopets, V. G. Rybin, S. V. Leonov, A. I. Voroshilova, and D. N. Butusov, “Advanced tone rendition technique for a painting robot”, *Robotics and Autonomous Systems*, vol. 115, pp. 17–27, 2019.
- [129] S. Kudoh, K. Ogawara, M. Ruchanurucks, and K. Ikeuchi, “Painting robot with multi-fingered hands and stereo vision”, *Robotics and Autonomous Systems*, vol. 57, no. 3, pp. 279–288, 2009.
- [130] O. Igno-Rosario, C. Hernandez-Aguilar, A. Cruz-Orea, and A. Dominguez-Pacheco, “Interactive system for painting artworks by regions using a robot”, *Robotics and Autonomous Systems*, vol. 121, p. 103 263, 2019.
- [131] T. Lindemeier, J. Metzner, L. Pollak, and O. Deussen, “Hardware-based non-photorealistic rendering using a painting robot”, *Computer Graphics Forum*, vol. 34, no. 2, pp. 311–323, 2015.
- [132] L. Scalera, S. Seriani, A. Gasparetto, and P. Gallina, “Non-photorealistic rendering techniques for artistic robotic painting”, *Robotics*, vol. 8, no. 1, 2019.
- [133] A. Beltramello, L. Scalera, S. Seriani, and P. Gallina, “Artistic robotic painting using the palette knife technique”, *Robotics*, vol. 9, no. 1, 2020.
- [134] A. Schubert, “An optimal control based analysis of human action painting motions”, PhD thesis, Heidelberg, Germany, 2017.

- [135] K. Ren and P. G. Kry, “Single Stroke Aerial Robot Light Painting”, in *ACM/EG Expressive Symposium*, C. S. Kaplan, A. Forbes, and S. DiVerdi, Eds., The Eurographics Association, 2019.
- [136] S. Aupetit, V. Bordeau, N. Monmarche, M. Slimane, and G. Venturini, “Interactive evolution of ant paintings”, in *The 2003 Congress on Evolutionary Computation, 2003. CEC '03.*, vol. 2, Dec. 2003, 1376–1383 Vol.2.
- [137] G. Greenfield, “Evolutionary methods for ant colony paintings”, in *Applications of Evolutionary Computing*, F. Rothlauf, J. Branke, S. Cagnoni, D. W. Corne, R. Drechsler, Y. Jin, P. Machado, E. Marchiori, J. Romero, G. D. Smith, and G. Squillero, Eds., Berlin, Heidelberg: Springer Berlin Heidelberg, 2005, pp. 478–487.
- [138] P. Urbano, “Playing in the pheromone playground: Experiences in swarm painting”, in *Applications of Evolutionary Computing*, F. Rothlauf, J. Branke, S. Cagnoni, D. W. Corne, R. Drechsler, Y. Jin, P. Machado, E. Marchiori, J. Romero, G. D. Smith, and G. Squillero, Eds., Berlin, Heidelberg: Springer Berlin Heidelberg, 2005, pp. 527–532.
- [139] M. D. Cooney, S. Nishio, and H. Ishiguro, “Recognizing affection for a touch-based interaction with a humanoid robot”, in *2012 IEEE/RSJ International Conference on Intelligent Robots and Systems*, 2012, pp. 1420–1427.
- [140] M. A. Arbib and J.-M. Fellous, “Emotions: From brain to robot”, *Trends in Cognitive Sciences*, vol. 8, no. 12, pp. 554–561, 2004.
- [141] C. Breazeal and B. Scassellati, “How to build robots that make friends and influence people”, in *Proceedings 1999 IEEE/RSJ International Conference on Intelligent Robots and Systems. Human and Environment Friendly Robots with High Intelligence and Emotional Quotients (Cat. No.99CH36289)*, vol. 2, 1999, 858–863 vol.2.
- [142] A. Camurri, B. Mazzarino, M. Ricchetti, R. Timmers, and G. Volpe, “Multimodal analysis of expressive gesture in music and dance performances”, in *Gesture-Based Communication in Human-Computer Interaction*, Berlin, Heidelberg: Springer Berlin Heidelberg, 2004, pp. 20–39.
- [143] P. Juslin, “From mimesis to catharsis: Expression, perception, and induction of emotion in music”, in *Musical Communication*. Oxford: Oxford University Press, 2005.
- [144] C. Breazeal, “Toward sociable robots”, *Robotics and Autonomous Systems*, vol. 42, pp. 167–175, 2003.

- [145] J. Or, “Towards the development of emotional dancing humanoid robots”, *International Journal of Social Robotics*, vol. 1, no. 4, p. 367, Oct. 2009.
- [146] M. Perkowski, A. Bhutada, M. Lukac, and M. Sunardi, “On synthesis and verification from event diagrams in a robot theatre application”, in *2013 IEEE 43rd International Symposium on Multiple-Valued Logic*, May 2013, pp. 77–83.
- [147] M. Bretan, G. Hoffman, and G. Weinberg, “Emotionally expressive dynamic physical behaviors in robots”, *International Journal of Human-Computer Studies*, vol. 78, pp. 1–16, 2015.
- [148] G. Hoffman, R. Kubat, and C. Breazeal, “A hybrid control system for puppeteering a live robotic stage actor”, in *RO-MAN 2008 - The 17th IEEE International Symposium on Robot and Human Interactive Communication*, Aug. 2008, pp. 354–359.
- [149] R. Laban and F. Lawrence, *Effort*. London: Macdonald & Evans Ltd, 1947.
- [150] E. I. Barakova and T. Lourens, “Expressing and interpreting emotional movements in social games with robots”, *Personal and Ubiquitous Computing*, vol. 14, no. 5, pp. 457–467, Jul. 2010.
- [151] H. Knight and R. Simmons, “Expressive motion with x, y and theta: Laban effort features for mobile robots”, in *The 23rd IEEE International Symposium on Robot and Human Interactive Communication*, 2014, pp. 267–273.
- [152] T. Lourens, R. van Berkel, and E. Barakova, “Communicating emotions and mental states to robots in a real time parallel framework using laban movement analysis”, *Robotics and Autonomous Systems*, vol. 58, no. 12, pp. 1256–1265, 2010, Intelligent Robotics and Neuroscience.
- [153] M. Masuda, S. Kato, and H. Itoh, “Emotion detection from body motion of human form robot based on laban movement analysis”, in *Principles of Practice in Multi-Agent Systems*, J.-J. Yang, M. Yokoo, T. Ito, Z. Jin, and P. Scerri, Eds., Berlin, Heidelberg: Springer Berlin Heidelberg, 2009, pp. 322–334.
- [154] ———, “A laban-based approach to emotional motion rendering for human-robot interaction”, in *Entertainment Computing - ICEC 2010*, H. S. Yang, R. Malaka, J. Hoshino, and J. H. Han, Eds., Berlin, Heidelberg: Springer Berlin Heidelberg, 2010, pp. 372–380.
- [155] P. Salaris, N. Abe, and J.-P. Laumond, “A worked-out experience in programming humanoid robots via the kinetography laban”, in *Dance Notations and Robot Motion*, J.-P. Laumond and N. Abe, Eds. Cham: Springer International Publishing, 2016, pp. 339–359.

- [156] G. A. Hollinger, Y. Georgiev, A. Manfredi, B. A. Maxwell, Z. A. Pezzementi, and B. Mitchell, “Design of a social mobile robot using emotion-based decision mechanisms”, in *2006 IEEE/RSJ International Conference on Intelligent Robots and Systems*, 2006, pp. 3093–3098.
- [157] S. Turkle, C. Breazeal, B. Scassellati, and O. Dasté, “Encounters with kismet and cog: Children respond to relational artifacts”, in *Humanoids*, 2004.
- [158] M. Heimerdinger and A. LaViers, “Influence of environmental context on recognition rates of stylized walking sequences”, in *Social Robotics*, A. Kheddar, E. Yoshida, S. S. Ge, K. Suzuki, J.-J. Cabibihan, F. Eyssel, and H. He, Eds., Cham: Springer International Publishing, 2017, pp. 272–282.
- [159] M. Zecca, Y. Mizoguchi, K. Endo, F. Iida, Y. Kawabata, N. Endo, K. Itoh, and A. Takanishi, “Whole body emotion expressions for kobian humanoid robot preliminary experiments with different emotional patterns ”, in *RO-MAN 2009 - The 18th IEEE International Symposium on Robot and Human Interactive Communication*, 2009, pp. 381–386.
- [160] P. Ekman, “An argument for basic emotions”, *Cognition and Emotion*, vol. 6, no. 3-4, pp. 169–200, 1992.
- [161] C. E. Izard, *The Psychology of Emotions*. New York, NY, USA: Springer US, 1991.
- [162] P. Johnson-Laird and K. Oatley, “Basic emotions, rationality, and folk theory”, *Cognition and Emotion*, vol. 6, pp. 201–223, 1992.
- [163] A. Mehrabian and J. A. Russell, *An approach to environmental psychology*. Cambridge, MA, US: The MIT Press, 1974.
- [164] A. Mehrabian, *Basic dimensions for a general psychological theory: implications for personality, social, environmental, and developmental studies*. Cambridge: Oelgeschlager, Gunn & Hain, 1980.
- [165] J. Broekens and D. DeGroot, “Scalable and flexible appraisal models for virtual agents”, in *Proc. of the 5th Game-On International Conference*, 2004, pp. 208–215.
- [166] N. Frijda, *The Emotions*, ser. Studies in Emotion and Social Interaction. Cambridge University Press, 1986.
- [167] J. A. Russell, “A circumplex model of affect”, *Journal of Personality and Social Psychology*, vol. 39, no. 6, pp. 1161–1178, 1980.

- [168] A. de Rooij, J. Broekens, and M. H. Lamers, “Abstract expressions of affect”, *International Journal of Synthetic Emotions*, vol. 4, no. 1, pp. 1–31, 2013.
- [169] J.-H. Lee, J.-Y. Park, and T.-J. Nam, “Emotional interaction through physical movement”, in *International Conference on Human-Computer Interaction*, J. A. Jacko, Ed. Berlin, Heidelberg: Springer Berlin Heidelberg, 2007, pp. 401–410.
- [170] F. E. Pollick, H. M. Paterson, A. Bruderlin, and A. J. Sanford, “Perceiving affect from arm movement”, *Cognition*, vol. 82, no. 2, B51 –B61, 2001.
- [171] M. Saerbeck and C. Bartneck, “Perception of affect elicited by robot motion”, in *2010 5th ACM/IEEE International Conference on Human-Robot Interaction (HRI)*, Mar. 2010, pp. 53–60.
- [172] M. Sawada, K. Suda, and M. Ishii, “Expression of emotions in dance: Relation between arm movement characteristics and emotion”, *Perceptual and Motor Skills*, vol. 97, no. 3, pp. 697–708, 2003.
- [173] B. Rimé, B. Boulanger, P. Laubin, M. Richir, and K. Stroobants, “The perception of interpersonal emotions originated by patterns of movement”, *Motivation and Emotion*, vol. 9, no. 3, pp. 241–260, 1985.
- [174] C. L. Roether, L. Omlor, and M. A. Giese, “Features in the recognition of emotions from dynamic bodily expression”, in *Dynamics of Visual Motion Processing: Neuronal, Behavioral, and Computational Approaches*, U. J. Ilg and G. S. Masson, Eds. Boston, MA: Springer US, 2010, pp. 313–340.
- [175] J. Aronoff, “How we recognize angry and happy emotion in people, places, and things”, *Cross-Cultural Research*, vol. 40, no. 1, pp. 83–105, 2006.
- [176] J. Bassili, “Facial motion in the perception of faces and of emotional expression”, *Journal of experimental psychology. Human perception and performance*, vol. 4, no. 3, pp. 373–379, 1978.
- [177] J. Aronoff, A. M. Barclay, and L. A. Stevenson, “The recognition of threatening facial stimuli”, *Journal of Personality and Social Psychology*, vol. 54, no. 4, pp. 647–655, 1988.
- [178] J. Aronoff, B. A. Woike, and L. M. Hyman, “Which are the stimuli in facial displays of anger and happiness? configurational bases of emotion recognition”, *Journal of Personality and Social Psychology*, vol. 62, no. 6, pp. 1050–1066, 1992.
- [179] G. L. Collier, “Affective synesthesia: Extracting emotion space from simple perceptual stimuli”, *Motivation and Emotion*, vol. 20, no. 1, pp. 1–32, 1996.

- [180] J. P. Grotzinger, J. Crisp, A. R. Vasavada, R. C. Anderson, C. J. Baker, R. Barry, D. F. Blake, P. Conrad, K. S. Edgett, B. Ferdowski, R. Gellert, J. B. Gilbert, M. Golombek, J. Gómez-Elvira, D. M. Hassler, L. Jandura, M. Litvak, P. Mahaffy, J. Maki, M. Meyer, M. C. Malin, I. Mitrofanov, J. J. Simmonds, D. Vaniman, R. V. Welch, and R. C. Wiens, “Mars science laboratory mission and science investigation”, *Space Science Reviews*, vol. 170, no. 1, pp. 5–56, Sep. 2012.
- [181] L. E. Parker, “Heterogeneous multi-robot cooperation”, PhD thesis, Cambridge, MA, USA, 1994.
- [182] J. R. Souza, C. C. T. Mendes, V. Guizilini, K. C. T. Vivaldini, A. Colturato, F. Ramos, and D. F. Wolf, “Automatic detection of ceratocystis wilt in eucalyptus crops from aerial images”, in *2015 IEEE International Conference on Robotics and Automation (ICRA)*, Seattle, WA, May 2015, pp. 3443–3448.
- [183] C. K. Ho, A. Robinson, D. R. Miller, and M. J. Davis, “Overview of sensors and needs for environmental monitoring”, *Sensors*, vol. 5, no. 1, pp. 4–37, 2005.
- [184] M. Santos, Y. Diaz-Mercado, and M. Egerstedt, “Coverage control for multirobot teams with heterogeneous sensing capabilities”, *IEEE Robotics and Automation Letters*, vol. 3, no. 2, pp. 919–925, Apr. 2018.
- [185] M. Santos and M. Egerstedt, “Coverage control for multi-robot teams with heterogeneous sensing capabilities using limited communications”, in *IEEE/RSJ International Conference on Intelligent Robots and Systems (IROS)*, 2018, pp. 5313–5319.
- [186] Q. Du and M. Emelianenko, “Acceleration Schemes for Computing Centroidal Voronoi Tessellations”, *Numerical Linear Algebra with Applications*, vol. 13, no. 2-3, pp. 173–192, Feb. 2006.
- [187] F. Aurenhammer, “Voronoi diagrams – a survey of a fundamental geometric data structure”, *ACM Comput. Surv.*, vol. 23, no. 3, pp. 345–405, Sep. 1991.
- [188] D. Pickem, P. Glotfelter, L. Wang, M. Mote, A. Ames, E. Feron, and M. Egerstedt, “The Robotarium: A remotely accessible swarm robotics research testbed”, in *2017 IEEE International Conference on Robotics and Automation (ICRA)*, Singapore, May 2017, pp. 1699–1706.
- [189] D. Pickem, M. Lee, and M. Egerstedt, “The GRITSBot in its natural habitat – a multi-robot testbed”, in *2015 IEEE International Conference on Robotics and Automation (ICRA)*, Seattle, WA, May 2015, pp. 4062–4067.
- [190] N. A. Atanasov, J. Le Ny, and G. J. Pappas, “Distributed algorithms for stochastic source seeking with mobile robot networks”, *Journal of Dynamic Systems, Measurement, and Control*, vol. 137, no. 3, p. 031 004, Mar. 2015.

- [191] S. Wilson, P. Glotfelter, L. Wang, S. Mayya, G. Notomista, M. Mote, and M. Egerstedt, “The robotarium: Globally impactful opportunities, challenges, and lessons learned in remote-access, distributed control of multirobot systems”, *IEEE Control Systems Magazine*, vol. 40, no. 1, pp. 26–44, Feb. 2020.
- [192] M. Santos, S. Mayya, G. Notomista, and M. Egerstedt, “Decentralized minimum-energy coverage control for time-varying density functions”, in *2019 International Symposium on Multi-Robot and Multi-Agent Systems (MRS)*, New Brunswick, NJ, Aug. 2019, pp. 155–161.
- [193] M. Egerstedt, J. N. Pauli, G. Notomista, and S. Hutchinson, “Robot ecology: Constraint-based control design for long duration autonomy”, *Annual Reviews in Control*, 2018.
- [194] G. Notomista, S. Mayya, M. Selvaggio, M. Santos, and C. Secchi, “A set-theoretic approach to multi-task execution and prioritization”, in *2020 International Conference on Robotics and Automation (ICRA)*, 2020.
- [195] E. A. Basso and K. Y. Pettersen, “Task-priority control of redundant robotic systems using control lyapunov and control barrier function based quadratic programs”, arXiv version available at <https://arxiv.org/pdf/2001.07547.pdf>, 2020.
- [196] X. Xu, P. Tabuada, J. W. Grizzle, and A. D. Ames, “Robustness of control barrier functions for safety critical control”, *IFAC-PapersOnLine*, vol. 48, no. 27, pp. 54–61, 2015.
- [197] G. Notomista and M. Egerstedt, “Persistification of robotic tasks”, *IEEE Transactions on Control Systems Technology*, pp. 1–12, 2020.
- [198] Y. Diaz-Mercado, S. G. Lee, and M. Egerstedt, “Human–swarm interactions via coverage of time-varying densities”, in *Trends in Control and Decision-Making for Human–Robot Collaboration Systems*, Y. Wang and F. Zhang, Eds. Cham: Springer International Publishing, 2017, pp. 357–385.
- [199] H. K. Khalil and J. W. Grizzle, *Nonlinear systems*. Prentice hall Upper Saddle River, NJ, 2002, vol. 3.
- [200] R. Olfati-Saber, “Near-identity diffeomorphisms and exponential ϵ -tracking and ϵ -stabilization of first-order nonholonomic $se(2)$ vehicles”, in *Proceedings of the 2002 American Control Conference*, vol. 6, May 2002, pp. 4690–4695.
- [201] M. H. Protter and C. B. J. Morrey, “Differentiation under the integral sign. improper integrals. the gamma function”, in *Intermediate Calculus*, ser. Undergraduate Texts in Mathematics. New York, NY: Springer, 1985.

- [202] L. Scalera, S. Seriani, A. Gasparetto, and P. Gallina, “Watercolour robotic painting: A novel automatic system for artistic rendering”, *Journal of Intelligent & Robotic Systems*, vol. 95, no. 3, pp. 871–886, Sep. 2019.
- [203] R. Berns, *Billmeyer and Saltzman’s Principles of Color Technology*, 3rd ed. New York: Wiley, 2000.
- [204] P. Twu, Y. Mostofi, and M. Egerstedt, “A measure of heterogeneity in multi-agent systems”, in *2014 American Control Conference*, 2014, pp. 3972–3977.
- [205] D. Androutsos, K. N. Plataniotiss, and A. N. Venetsanopoulos, “Distance measures for color image retrieval”, in *Proceedings 1998 International Conference on Image Processing. ICIP98 (Cat. No.98CB36269)*, vol. 2, 1998, 770–774 vol.2.
- [206] D. Kim, S.-W. Son, and H. Jeong, “Large-scale quantitative analysis of painting arts”, *Scientific Reports*, vol. 4, p. 7370, Dec. 2014.
- [207] L. Brown, R. Kerwin, and A. M. Howard, “Applying behavioral strategies for student engagement using a robotic educational agent”, in *2013 IEEE International Conference on Systems, Man, and Cybernetics*, Oct. 2013, pp. 4360–4365.
- [208] T. Belpaeme, P. Baxter, R. Read, R. Wood, H. Cuayáhuitl, B. Kiefer, S. Racioppa, I. Kruijff-Korbayová, G. Athanasopoulos, V. Enescu, R. Looije, M. Neerincx, Y. Demiris, R. Ros-Espinoza, A. Beck, L. Cañamero, A. Hiolle, M. Lewis, I. Baroni, M. Nalin, P. Cosi, G. Paci, F. Tesser, G. Sommariva, and R. Humbert, “Multimodal child-robot interaction: Building social bonds”, *J. Hum.-Robot Interact.*, vol. 1, no. 2, pp. 33–53, Jan. 2013.
- [209] G. Hoffman, “Dumb robots, smart phones: A case study of music listening companionship”, in *2012 IEEE RO-MAN: The 21st IEEE International Symposium on Robot and Human Interactive Communication*, Sep. 2012, pp. 358–363.
- [210] J.-J. Cabibihan, H. Javed, M. Ang, and S. M. Aljunied, “Why robots? a survey on the roles and benefits of social robots in the therapy of children with autism”, *International Journal of Social Robotics*, vol. 5, no. 4, pp. 593–618, Nov. 2013.
- [211] H. Kozima, M. P. Michalowski, and C. Nakagawa, “Keep on”, *International Journal of Social Robotics*, vol. 1, no. 1, pp. 3–18, Jan. 2009.
- [212] M. A. Goodrich and A. C. Schultz, “Human-robot interaction: A survey”, *Found. Trends Hum.-Comput. Interact.*, vol. 1, no. 3, pp. 203–275, Jan. 2007.
- [213] T. B. Sheridan, “Humanrobot interaction: Status and challenges”, *Human Factors*, vol. 58, no. 4, pp. 525–532, 2016.

- [214] P. Ekman, “Facial expression and emotion”, *American Psychologist*, vol. 48, no. 4, pp. 384–392, 1993.
- [215] M. Santos and M. Egerstedt, “From motions to emotions: Exploring the emotional expressiveness of robot swarms”, in *2019 IEEE International Conference on Robotics and Automation (ICRA), ICRA-X: Robotic Art Program. Expressive Motions*, 2019.
- [216] C. E. Izard, “Emotion theory and research: Highlights, unanswered questions, and emerging issues”, *Annual review of psychology*, vol. 60, pp. 1–25, 2009.
- [217] —, *Human Emotions*, ser. Emotions, Personality and Psychotherapy. New York, NY, USA: Springer US, 1977.
- [218] R. Plutchik, “The nature of emotions: Human emotions have deep evolutionary roots, a fact that may explain their complexity and provide tools for clinical practice”, *American Scientist*, vol. 89, no. 4, pp. 344–350, 2001.
- [219] E. W. Justh and P. S. Krishnaprasad, “Steering laws and continuum models for planar formations”, in *42nd IEEE International Conference on Decision and Control*, vol. 4, Dec. 2003, 3609–3614 vol.4.
- [220] J. A. Marshall, M. E. Broucke, and B. A. Francis, “Formations of vehicles in cyclic pursuit”, *IEEE Transactions on Automatic Control*, vol. 49, no. 11, pp. 1963–1974, Nov. 2004.
- [221] J. L. Ramirez, M. Pavone, E. Frazzoli, and D. W. Miller, “Distributed control of spacecraft formation via cyclic pursuit: Theory and experiments”, in *2009 American Control Conference*, Jun. 2009, pp. 4811–4817.
- [222] R. T. Ross, “A statistic for circular series”, *Journal of Educational Psychology*, vol. 29, no. 5, pp. 384–389, 1938.